Doubly-Tagged D_s Decays at 4.03 GeV

Thesis by

Ernest N. Prabhakar

In Partial Fulfillment of the Requirements

for the Degree of

Doctor of Philosophy

California Institute of Technology

Pasadena, California

1995

(Submitted May 23rd, 1995)

Acknowledgements

In the production of this thesis, and the pursuit of my graduate career, I would like to acknowledge my indebtedness to:

- the God who created such a wonderful universe for me to study, and gave me the skills and resources to explore it;
- my parents, John and Esther, who raised me, supported me, and set me free to follow my hearts desire;
- my advisor, David Hitlin, who took me in and gave me the freedom to do things a little differently;
- Mike Kelsey, who despite six years of sharing an office made every day a new adventure;
- the many friendships, which made it all worthwhile.

  Special thanks are due to Mike Kelsey and Jim Panetta for copious last minute proofreading.

Abstract

The D_s is a pseudoscalar meson composed of two second generation quarks, the heavy charm and the light strange. The bulk of our knowledge of the D_s comes from secondary production via B decays. These experiments have high statistics but are poorly suited to absolute branching fraction or production cross-section measurements. The best way to perform those is to use double-tagging of threshold pair production. Unfortunately, there is no strong resonance near D_s threshold, making it difficult to obtain sufficient statistics.

This thesis makes use of the $\mathcal{L}$ =22.8 $\pm$ 0.6 pb^{-1}integrated luminosity collected by the Beijing Spectrometer from the Beijing Electron-Positron Collider at 4.03 GeV. This energy was chosen because the coupled-channel model of Eichten *et al.* predicts an enhancement there of the $D_s^+D_s^-$ cross section to somewhat below 1 nb. We attempt to fully reconstruct hadronic and semileptonic D_s pairs from six-prong events not containing any photons. We combine the χ^2 from kinematic fitting and particle identification to form a single value, the joint confidence level, for each event.

Using this in the analysis yields five hadronic events, with multiple combinations per event. Since the D_s principally decays to resonant moves, we preferentially select those combinations which lead to resonant two-body masses. This gives us a signal containing 7 resonant decays and 3 non-resonant $K^+K^-\pi^+$ decays. We use Monte Carlo efficiencies and knowledge of the ratio $B(D_s^+ \to \overline{K}^{*0}K^+)/B(D_s^+ \to K^+K^-\pi^+)$ to estimate the production rates represented by these tags.

We perform a likelihood analysis using those numbers, together with the absolute branching fractions, to obtain a value of $\sigma(e^+e^- \to D_s^+D_s^-)$ at 4.03 GeV = $0.53^{+0.28\ +0.07}_{-0.20\ -0.09}$nb, one sigma below the coupled channel model. Using only relative branching fractions, we fit to a value for the ratio $B(D_s^+ \to \overline{K}^{*0}K^+)/B(D_s^+ \to \phi\pi^+)$ of $1.78^{+1.23\ +.22}_{-0.80\ -0.24}$. This is within one sigma of the current world average, and differs noticeably from the model of Bauer, Stech, and Wirbel value of 0.56 $\pm$ 0.7.

Contents

Acknowledgements iii

Abstract iv

I Introduction 1

1 The Standard Model 2

1.1 Bosons 2

1.2 Fermions 5

II Experiment 9

2 The Accelerator 10

3 The Detector 13

3.1 Magnetic Field 15

3.2 Beampipe 16

3.3 Luminosity Monitor 16

3.4 Central Drift Chamber 18

3.5 Main Drift Chamber 19

3.6 TOF 20

3.7 Electromagnetic Calorimeter 21

3.8 Muon System 21

3.9 Trigger 22

4 The Data 24

4.1 Data Processing 24

4.2 The Cross-Sections 25
4.3 The Hadronic Strip 26

III Expectations **30**

5 Experimental **31**
5.1 Decay Rates 31
5.2 Reconstruction Rates 32

6 Theoretical **36**
6.1 Weak Decays 36
6.2 The Factorization Model of BSW 38
6.2.1 Semileptonic Decays 38
6.2.2 Hadronic Decays 40
6.2.3 Results 42

IV The Analysis **44**

7 The Analysis **45**
7.1 Datasets 45
7.2 Track Selection 46
7.3 Event Classification 52
7.4 Particle Identification (PID) 52
7.5 Combinatorics 55
7.6 Kinematic Fitting 56
7.7 Summary 58

8 The Double-Tag Sample **59**
8.1 Tag Selection 59
8.1.1 Twobody Resonances 63
8.1.2 Combinatoric Reduction 63

8.1.3 Signal Events 65
8.2 Backgrounds 69
8.2.1 Three-Kaon Background 69
8.2.2 Four-Kaon Background 73
8.2.3 Summary 75
8.3 Efficiencies 75

9 Results **81**
9.1 Summed Mode Analysis 81
9.2 Multiple Mode Analysis 82
9.2.1 Cross-Section 83
9.2.2 $\overline{K}^{*0}K^{+}$ Branching Fraction 83
9.3 Systematics 86
9.4 Conclusions 87

V The Appendix **88**

A One Event Displays **89**

Bibliography **96**

List of Figures

1.1 Fundamental particles in the Standard Model. 3
1.2 Feynman diagram for electromagnetic interactions. 3
1.3 Tree-level QCD diagram plus a loop correction. 5

2.1 The Beijing Electron Positron Collider (BEPC). 11

3.1 Side view of the BES detector. 14
3.2 Axial view of the BES detector. 15
3.3 Luminosity monitor telescopes. 17

4.1 Cross-sections for D meson production relative to dimuon production. 27
4.2 Cross-sections for D_s meson production relative to dimuon production. 28

6.1 Weak decay processes. 37
6.2 BSW hadronic charm decays. 39

7.1 Number of charged and neutral tracks in real data. 47
7.2 Number of charged and neutral tracks in hadronic MC signal. 48
7.3 Number of charged and neutral tracks in semileptonic MC signal. . . 49
7.4 Number of charged and neutral tracks in D^* MC background. 50
7.5 Number of charged and neutral tracks in D_s including π^0 MC background. 51
7.6 Good event momenta for real data and signal MC. 53
7.7 Good event momenta for background. 54

8.1 $P(D_s)$ for signal MC. 60
8.2 $P(D_s)$ for real data. 61
8.3 Leptonic signal and D_s including π^0 background Monte Carlo. 62
8.4 Twobody resonance Monte Carlo plots. 64
8.5 Invariant and beam-energy constrained masses for signal Monte Carlo. 66

8.6 Confidence levels for Monte Carlo signal data. 67
8.7 Mass plot from equal-mass fit of real data. 70
8.8 Background in three- and four-kaon channels 72
8.9 $m_{\pi\pi}$ phase space for nonresonant $D_s \to K\pi\pi$ decays. 72
8.10 Mass plot from equal-mass fit of D^* Monte Carlo. 74

9.1 Poisson likelihood for n = 5. 82
9.2 Multiple mode likelihood function for $N_{\phi\pi\phi\pi}$. 84
9.3 Likelihood function for $\frac{B(D_s^+ \to \overline{K}^{*0} K^+)}{B(D_s^+ \to \phi\pi^+)}$. 85

A.1 One-event display for Run 3750, Event 4208. 90
A.2 One-event display for Run 4838, Event 11178. 91
A.3 One-event display for Run 5113, Event 19395. 92
A.4 One-event display for Run 6422, Event 27143. 93
A.5 One-event display for Run 6462, Event 31342. 94
A.6 One-event display for Run 7108, Event 19638. 95

List of Tables

1.1 The twelve vector bosons. 2
1.2 The three fermion generations. 5
1.3 The CKM weak mixing matrix amplitudes. 6
1.4 The muon and important light mesons. 7
1.5 Charmed mesons. 7
1.6 The low-mass $\bar{c}c$ resonances. 7

2.1 BEPC operating parameters. 11

4.1 BES data taking runs. 24
4.2 Coupled-channel model predictions at 4.03 GeV. 26
4.3 Hadronic strip cuts. 29

5.1 PDG values for principal D_s decay modes. 32
5.2 Three-prong decays of the D_s. 33
5.3 Background decays of the D_s $D^{\pm}$, and D^0. 33
5.4 Expected number of events in signal modes for $N_{\phi\pi\phi\pi} = 22$ 34

6.1 BSW Parameters 42
6.2 BSW predictions for D_s decay modes. 42

7.1 Monte Carlo datasets generated. 46
7.2 Hadronic and semileptonic particle identification triplets. 55
7.3 Particle identification hextets. 56
7.4 Constraints applied via kinematic fits. 57
7.5 Hardwired cuts. 58

8.1 Values used for two-body resonances. 63
8.2 Mode breakdown of final combinations. 65

8.3 Masses of signal events. 68
8.4 Confidence levels of signal events. 68
8.5 Summary of interactive cuts applied. 68
8.6 Background combinations of real data with $P(m^+ = m^-) > 0.001$ cut. 71
8.7 Non-resonant $K\pi\pi$ background events. 71
8.8 Background events with four kaons. 73
8.9 Measured signal and background events. 75
8.10 Counts from hadronic Monte Carlo. 76
8.11 Counts from semileptonic Monte Carlo. 76
8.12 Efficiencies from semileptonic Monte Carlo. 77
8.13 $\overline{K}^{*0}K^+$ versus $K^+K^-\pi^+$ efficiencies. 78
8.14 Effective number of signal and background events. 80

9.1 Sources of uncertainty in fitted and derived quantities. 86

Part I

Introduction

Chapter 1 The Standard Model

The Standard Model postulates that the universe is made of twelve different vector bosons and twelve spin-$\frac{1}{2}$ fermions and their antiparticles, as shown in Figure 1.1. Formed out of the union of electroweak theory and quantum chromodynamics (QCD), the Standard Model has proven remarkably successful at explaining a wide variety of data. The Minimal Standard Model (MSM) also predicts a neutral scalar Higgs boson, associated with electroweak theory and the generation of mass. While there is strong theoretical motivation for at least one Higgs boson, there is as yet no evidence for its existence.

The vector bosons in the Standard Model act as carriers of forces, as shown in Table 1.1. They are associated with the generators for particular symmetry group: $SU(2) \otimes U(1)$ for electroweak, and $SU(3)$ for QCD. They couple to particles which form multiplets under those symmetries. The Standard Model does not fix the relation between the two, nor predict the parameters within them (such as masses and coupling constants). Various Grand Unified Theories (GUTs) attempt to do so, but also predict behavior such as proton decay which has not yet been observed.

1.1 Bosons

Electromagnetism, the most familiar force, is carried by photons and couples to electric charge with a strength of $\alpha = \frac{e^2}{4\pi\hbar c} \approx \frac{1}{137}$ at large distances. A photon can either

Force	Carrier	Number	Charge	Mass[1]
Color	gluon (g)	8	0	≈ 0
Electromagnetism	Photon (γ)	1	0	0
Neutral Weak	Z^0	1	0	91.187 GeV
Charged Weak	$W^{\pm}$	2	± 1	80.22 GeV

Table 1.1: The twelve vector bosons.

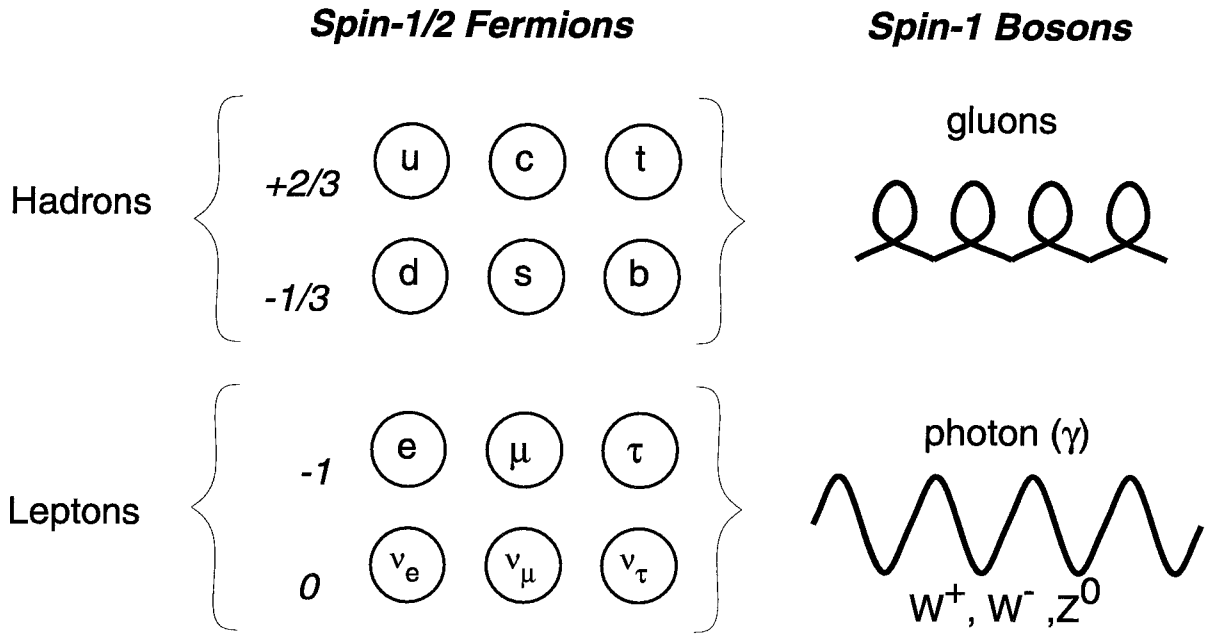

Figure 1.1: Fundamental particles in the Standard Model.

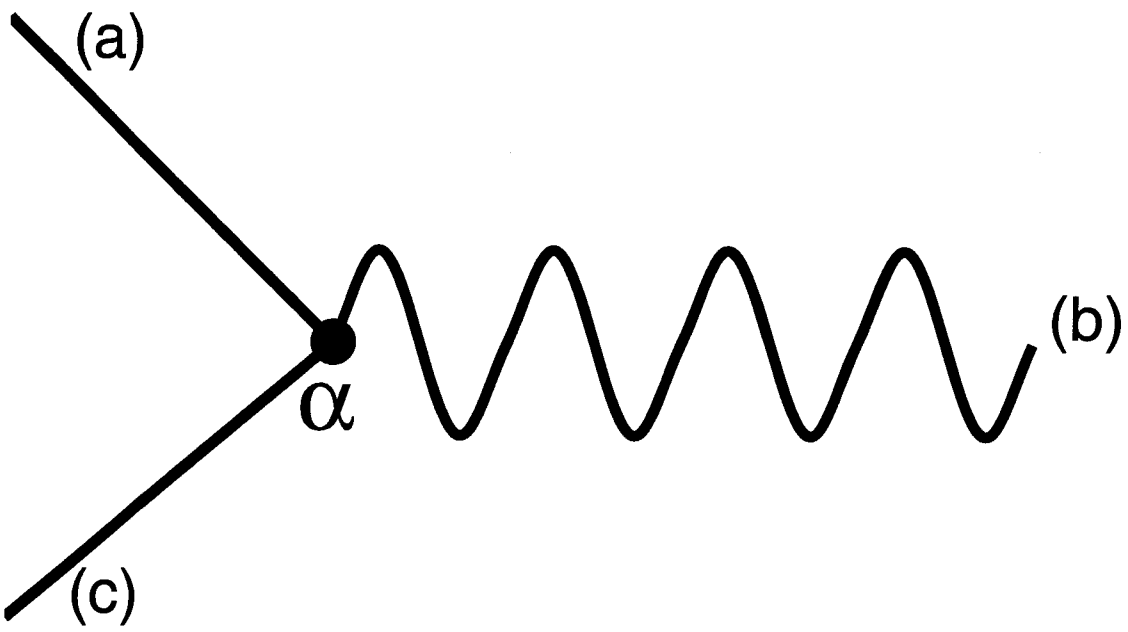

Figure 1.2: Feynman diagram for electromagnetic interactions. Emission is read downward, where (a) emits (b) and turns into (c). Annihilation is read to the right, where (a) annihilates (c), producing (b). Pair-production is read to the left, where (b) spontaneously produces both (a) and (c). All these interactions have a strength of α.

be emitted or absorbed by a charged particle, or it can be involved in the creation (pair-production) or destruction (annihilation) of charged particle-antiparticle pairs. These are all governed by the same Feynman diagram vertex, shown in Figure 1.2, read in different ways. In fact, even if a photon doesn't have enough energy to create two real particles, it will continually create virtual pairs, which could themselves emit virtual photons. However, the amplitude for each of these recursive processes is suppressed by a factor of α. This allows one to use perturbation theory to calculate their rate to any desired accuracy.

The Z^0 couples both to charged particles, and neutral particles like neutrinos. The $W^{\pm}$, on the other hand, couples to weak doublets, whose charge difference is one. The latter only couples to particles with negative helicity (spin times direction, $\vec{\sigma} \cdot \hat{p}$). Thus, left-handed particles and right-handed antiparticles form weak doublets, whereas their mirror images form weak singlets. Particles with mass will generally be in a superposition of helicity states. The Higgs symmetry breaking which gives mass to the fermions also leaves the weak bosons with a large mass. This results in a short-range force whose coupling constant $G_{Fermi} = 1.12 \times 10^{-5}\text{GeV}^{-2}$ is a million times smaller than α at nuclear scales. Both of these increase at higher energies, and become comparable at the weak scale.

By contrast, QCD has a large coupling constant ($\approx \frac{4}{3}$) which decreases with energy (presumably matching up with the others at the GUT scale, far above any imaginable experimental energy). QCD, also known as the strong force, couples to a triplet of charges, known as "color." Bound states (hadrons) involve either three colors (baryons) or a color-anticolor pair (mesons). The strong force actually increases with distance, making it impossible to isolate a colored object. Gluons, as the $SU(3)$ generators, also possess color, making it theoretically possible for them to form a bound state by themselves

The real problem with the strong force is that the coupling constant is greater than one at low energies. Thus, the perturbation series diverges, as diagrams increase in amplitude the more recursively produced gluons there are. Tree-level diagrams, such as that on the left of Figure 1.3, ignore this problem, which is associated with gluon

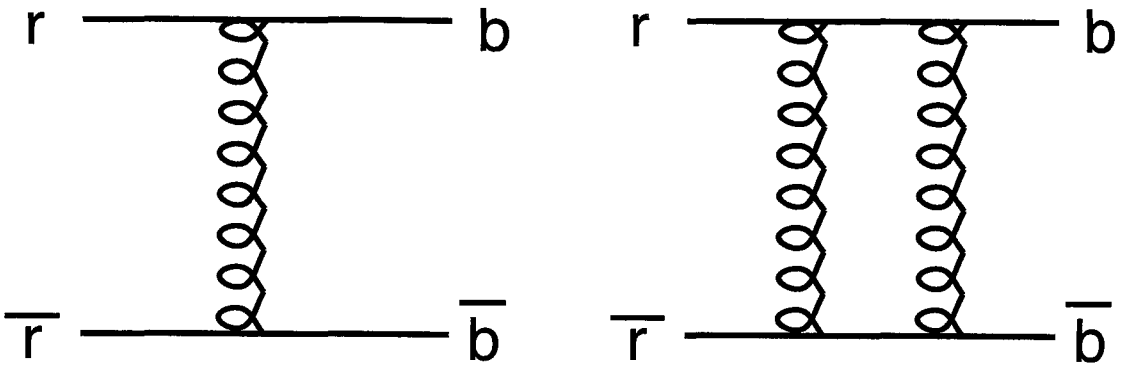

Figure 1.3: Tree-level QCD diagram plus a loop correction.

Quantum Numbers		Generation Number		
Lepton/Baryon	Weak Isospin	1	2	3
$L = 0$, $B = 1/3$	$I = +1/2$	$u \approx 5$MeV	$c \approx 1.3$GeV	$t \approx 180$GeV
	$I = -1/2$	$d \approx 10$MeV	$s \approx 200$MeV	$b \approx 4.3$GeV
$L = 1$, $B = 0$	$I = +1/2$	$\nu_e < 7$eV	$\nu_\mu < 0.27$MeV	$\nu_\tau < 31$MeV
	$I = -1/2$	$e = 0.511$MeV	$\mu = 105.7$MeV	$\tau = 1777$MeV

Table 1.2: The three fermion generations.

loops like that shown on the right. Tree-level diagrams are often useful for qualitative descriptions of processes, even if they are not quantitatively correct. However, there is in general no way to directly calculate QCD bound states, though there are various tricks and models that can help in particular circumstances. Non-perturbative methods, such as lattice gauge theory [2] which simulates space-time as a 4D lattice, hold out some hope of eventually calculating some of these quantities, but have not quite done so due to theoretical and computational limitations.

1.2 Fermions

There are three generations of fermions, each with a pair of quarks and a pair of leptons. These are listed in Table 1.2, along with their masses from Ref [1]. Each negatively charged lepton, along with its massless, neutral neutrino[1] form a weak

[1]The MSM predicts massless neutrinos. The possibility of neutrino mass is a hotly debated theoretical and experimental topic.

	d	s	b
u	0.97530 ± 0.00060	0.22100 ± 0.00300	0.00350 ± 0.00150
c	-0.22100 ± 0.00300	0.97450 ± 0.00070	0.04000 ± 0.00800
t	-0.01100 ± 0.00800	-0.04400 ± 0.01400	0.99915 ± 0.00035

Table 1.3: The CKM weak mixing matrix amplitudes.

doublet. For quarks, however, these are not formed by two quarks from the same generation with a well-defined mass. Instead, the eigenstates of the weak force are linear combinations of the mass eigenstates.[2] The mixing between the two is ascribed by convention to the down quarks, and handled by a unitary transformation known as the Cabbibo-Kobayashi-Maskawa (CKM) matrix.

The CKM matrix, whose elements are usually denoted V_{ij}, is a unitary 3x3 matrix, and hence can be parametrized by three real numbers plus a complex phase. The amplitudes from Ref [1] are shown in Table 1.3. The complex phase, if non-zero, would violate parity and may be responsible for the matter-antimatter asymmetry of the universe. Due to its small size, and the uncertainty in the other matrix elements, it has not yet been measured directly. Note that the diagonal terms are large, so quarks predominantly couple within their own generation.

If we work at energies where the top and bottom quarks are inaccessible, the CKM matrix reduces to a 2×2 matrix parametrized by a single angle. This is known as the Cabbibo angle, and has a value of $\sin\theta_C = 0.22$, giving a mixing of about 5%. In other words, a charm quark is almost twenty times more likely to decay to a strange quark than to a down quark. The former is referred to as a Cabbibo-allowed decay, while the latter is called Cabbibo-suppressed. This is a very important result, as it is decays of the charm quark that we will be concerned with in the next chapter.

The most interesting thing about quarks is that they carry color charge, and hence form bound states under QCD. In this thesis we are concerned with $q\bar{q}$ bound states known as mesons. A summary of mesons to which we will refer is given in the Tables 1.4, 1.5, and 1.6, using information from Ref [1]. For long-lived particles,

[2]If neutrinos have mass, then they would be liable to mixing as well. Otherwise, there is no other basis in which to decompose the weak eigenstate neutrinos.

Name	Mass (MeV)	Full Width / Lifetime ($c\tau$)	Quark Content	Principal Decays
$\mu^{\pm}$	105.66	659 m	none	$e^{+}\nu_e + \bar{\nu}_\mu$
$\pi^{\pm}$	139.6	7.8m	$u\bar{d}, \bar{u}d$	$\mu^{+}\nu_\mu$
π^0	135	25.1 nm	$u\bar{u} - \bar{d}d$	2γ
$K^{\pm}$	494	3.7 m	$u\bar{s}, \bar{u}s$	$\mu^{+}\nu_\mu, \pi^{+}\pi^0$
K^0_S	498	2.7 cm	$d\bar{s} + \bar{d}s$	$\pi\pi$
K^0_L	498	15.5 m	$d\bar{s} - \bar{d}s$	$\pi\pi\pi$
$K^*(892)^0$	896	50 MeV	$d\bar{s} + \bar{d}s$	$K\pi$
$f_0(980)$	980	40 to 400 MeV	$u\bar{u} + d\bar{d} + s\bar{s}$	$\pi\pi, KK$
$\phi(1020)$	1019.4	4.4 MeV	$s\bar{s}$	K K

Table 1.4: The muon and important light mesons.

	Pseudoscalar		Vector	
Quarks	Name	Mass (MeV)	Name	Mass (MeV)
$c\bar{d}$	$D^{\pm}$	1869.4 ± 0.4	$D^*(2010)^{\pm}$	2010.0 ± 0.5
$c\bar{u}$	D^0	1864.6 ± 0.5	$D^*(2007)^0$	2006.7 ± 0.5
$c\bar{s}$	$D_s^{\pm}$	1968.5 ± 0.7	$D_s^{*\pm}$	2110.0 ± 1.9

Table 1.5: Charmed mesons.

Common Name	Official Name	Mass (MeV)	Width (MeV)	Principal Decays
J/ψ	$J/\psi(1S)$	3097	0.090	Light mesons
ψ'	$\psi(2S)$	3686	0.277	J/ψ + mesons
ψ''	$\psi(3770)$	3770	24	$D, \bar{D}$
none	$\psi(4040)$	4040	52	D^0, $D^*(2007)^0$

Table 1.6: The low-mass $\bar{c}c$ resonances.

the lifetime is given in terms of the relativistic path length, $c\tau$, whereas that for the short-lived resonances is given in terms of decay width.

Part II

Experiment

Chapter 2 The Accelerator

The Beijing Electron Positron Collider (BEPC)[3], shown in Figure 2.1, was commissioned on April 24th, 1984 and began e^+e^- collisions on October 16th, 1988, two months ahead of schedule. It is located at the Institute of High Energy Physics in Beijing, which contained an existing linear accelerator that was adapted to inject electrons and positrons into a storage ring. There, they collide with each other under precisely controlled conditions. The design was based on the SPEAR ring at Stanford, upgraded for greater luminosity.

The energy range of the accelerator is from 3 to 5 GeV, where charmed mesons and tau leptons can be pair-produced near threshold. Not only would this mean that there are no extraneous particles in the event, it ensures that the particles in a pair each have the same energy as the beam. SPEAR and other machines of the late seventies that operated in this region have either been decommissioned or upgraded to higher energies, so BEPC is one of the few existing machines capable of precision measurements in this region. This energy is also suitable for glueball and hybrid studies, as well as general measurements of the cross-section for various processes in this regime.

Initial studies focused on the J/ψ, ψ', and τ particles[4]. D_s data taking began in the spring of 1992 and continued until the spring of 1994, apart from machine studies and calibration measurements at the J/ψ and ψ'. Operating parameters during the D_s run are shown in Table 2.1.

The 202 m linear accelerator alternately injects bunches of electrons and positrons into the storage ring. Each injection cycle fills one bunch of each in the ring, which degrade over the course of the several-hours-long run. Since the electrons and positrons have opposite charges, they can circle in opposing directions using the same beampipe and electronics. Powerful magnets bend the particles around the curves; this acceleration causes them to radiate away energy, which is restored by two radio-frequency

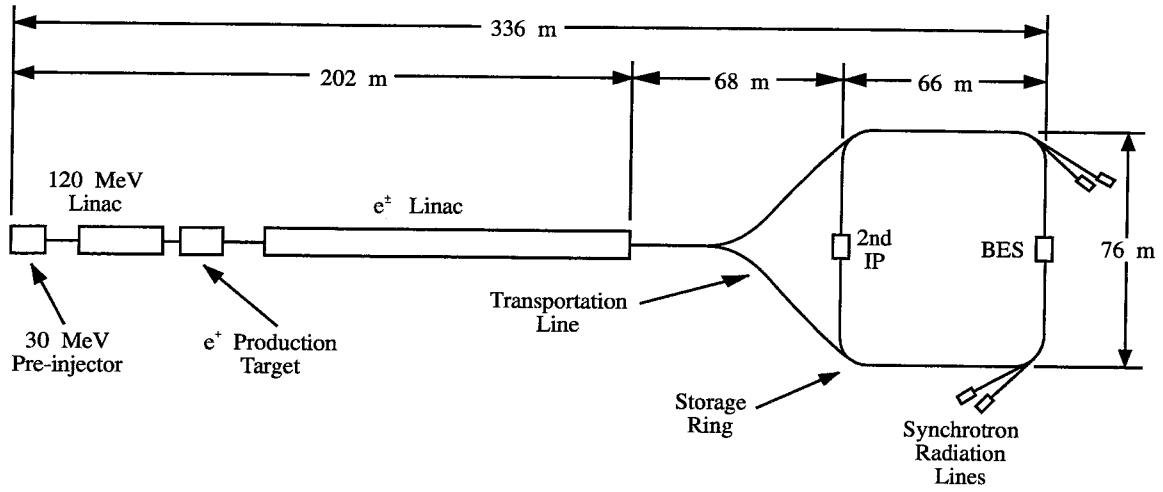

Figure 2.1: The Beijing Electron Positron Collider (BEPC).

Parameter	Symbol	Value	Units
Center of mass energy	E	3 – 5	GeV
Storage ring circumference	L	240.400	m
Bunch spacing	t_b	801.888	nsec
Number of bunches	N	1	
Natural bunch length	σ_l	5.20	cm
Number of particles per bunch at injection	N_b	6.8×10^{10}	
Revolution frequency	f_0	1247.057	kHz
Horizontal beta function at IP	β_x^*	103.00	cm
Vertical beta function at IP	β_y^*	8.5	cm
Horizontal spot size at IP	σ_x^*	592	μm
Vertical spot size at IP	σ_x^*	38.7	μm
Beam-beam linear tune shift	$\Delta\nu_x$	0.035	
Beam-beam linear tune shift	$\Delta\nu_y$	0.035	
Beam-pipe inner radius at IP	r^*	7.5	cm

Table 2.1: BEPC operating parameters.

(RF) cavities in the straightaways.

This loss is partly intentional, as the lost energy takes the form of synchrotron radiation (SR). As X-rays of precise frequency and high-intensity, SR is very useful for materials science studies. While this useful side-effect helps justify the construction of an accelerator, the difficulty in doing both colliding-beam physics and SR research simultaneously means the two groups often compete for running time.

Over most of the ring, the magnetic fields are designed to keep the counterrotating electrons and positrons from intersecting with each other. The exception is the Interaction Point (IP), located opposite the injection site. There, the two beams are focused down to a spot 40 microns high and 600 microns wide, intersecting along a distance of 10 centimeters. Particles produced by collisions here are seen by the detector, which almost completely surrounds the IP.

Chapter 3 The Detector

The detector at the IP is named the Beijing Spectrometer (BES). Started shortly after BEPC was begun, it was installed there in April 1989. BES[5] is a fairly standard, cylindrical, magnetic e^+e^- detector, modeled after the Mark III detector at SPEAR. It is about six meters long and seven meters high, as shown in Figures 3.1 and 3.2. Its *raison d'etre* is to measure the momentum and identity of the stable particles produced by collisions in BEPC, and thereby infer those of the unstable particles. Most detector subsystems are only designed to detect charged particles, but the electromagnetic calorimeter can also respond to photons.

The identity of particles is primarily determined from their velocity. The tracking system, in conjunction with the magnetic field, measures momentum. By observing the velocity-dependent interactions with other systems, we can then determine the mass of a particle, giving us its identity. The prime exception to this is the muon system, which uses the greater strength of hadronic interactions to differentiate pions from the similarly massive but weakly interacting muons.

The detector proper consists of a central and main drift chamber (CDC and MDC); a time-of-flight system (TOF); an electromagnetic calorimeter using shower counters (SC), and the muon system. Supplementing these are the magnetic field, the hardware trigger, the luminosity monitor, and the beampipe. Their operating parameters will vary with time, and must be determined by calibration. The subsystems are discussed below in the order they would be experienced by a particle produced at the IP. Their size is given in terms of inner diameter (ID), outer diameter (OD), and length. Both Cartesian and cylindrical coordinates are used, with z along the beampipe and y pointing upward.

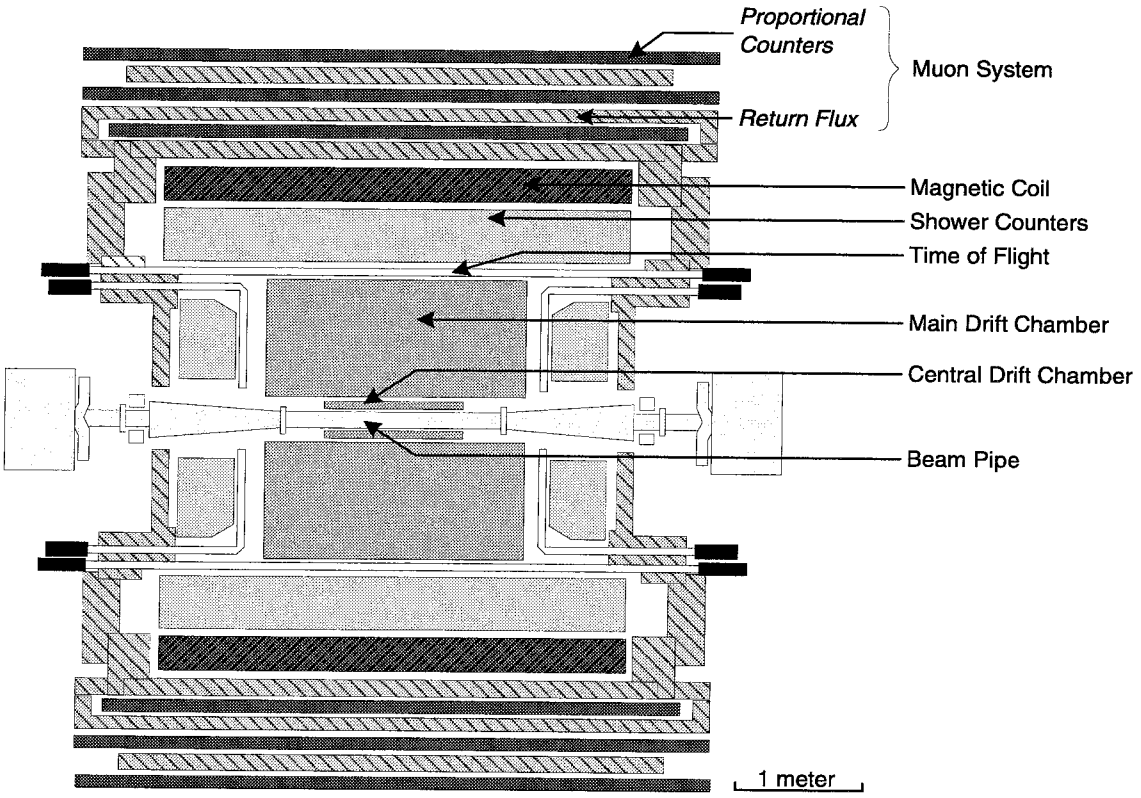

Figure 3.1: Side view of the BES detector.

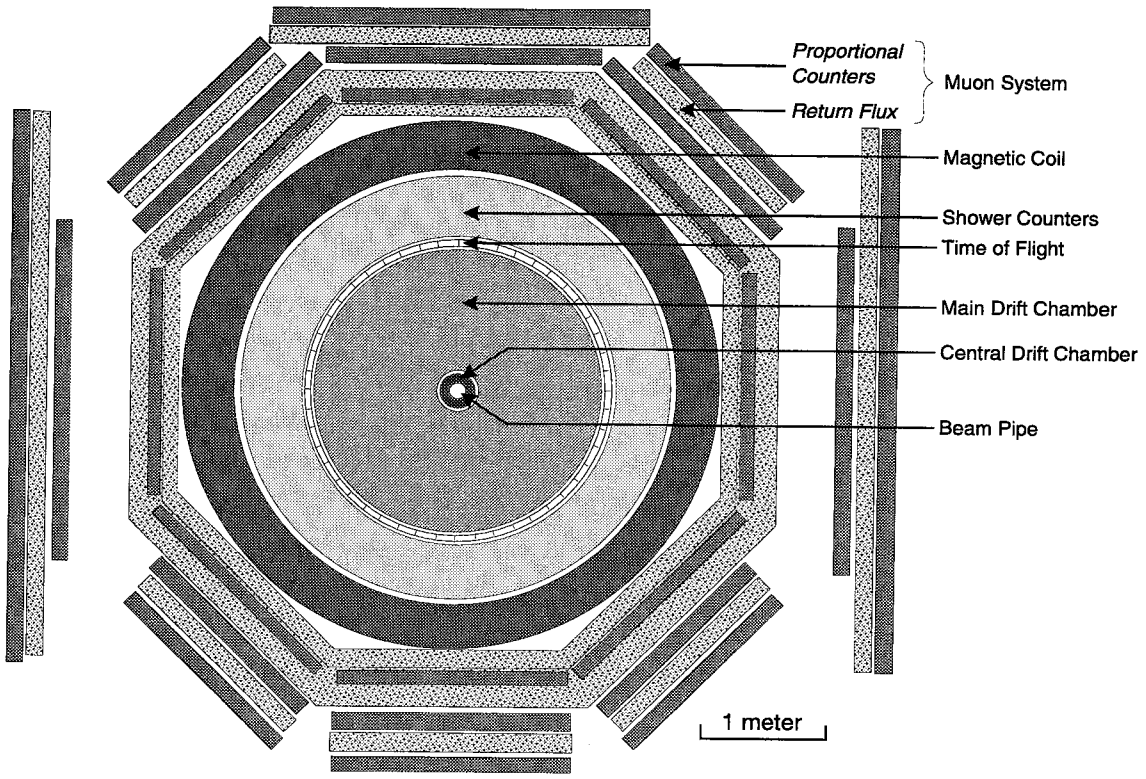

Figure 3.2: Axial view of the BES detector.

3.1 Magnetic Field

The first thing a particle newly created at the IP experiences is the presence of a magnetic field. The detector is swathed in an axial magnetic field of 0.4 tesla generated by an aluminum coil encapsulating nearly the entire detector, with an ID of 3.48 m, an OD of 4.14 m, and a length of 3.60 m. Within the tracking region, the field is uniform to within less then 3%.

The incoming electrons are not strongly affected by the field, since they are moving parallel to it. However, particles from collisions generally have a momentum component transverse to the field, which results in a helical trajectory around the axis. The faster the particle, the greater the radius of curvature. A stronger magnetic field allows greater resolution of high-momenta particles, which otherwise would look like straight lines. However, that causes particles with low transverse momentum to curl up so tight they never reach the detector. At BES, charged particles need $p_T > 40$ MeV/c to get far enough into the detector to be reconstructed.

3.2 Beampipe

Particles which avoid curling up face their first barrier: the aluminum beampipe. While integral to the detector, this pipe is part of the system which maintains a vacuum of 5×10^{-10} torr throughout the storage ring. It is a cylinder with an ID of 15.0 cm and OD of 15.4 cm, the thickness corresponding to 0.0225 radiation lengths. This can mean quite a substantial loss of energy for a slow-moving particle, since energy loss increases dramatically as a particle slows down. What is worse, the amount of energy lost depends on what kind of particle it is, so cannot be known until after identification has taken place. Energy loss is a function of velocity, and hence depends on both momenta and particle type. Kaons with less than about 140 MeV/c of momentum have a good chance of being stopped entirely by the beampipe.

3.3 Luminosity Monitor

Particles which escape the beampipe may enter the detector, and experience a (brief) lifetime of fame and significance. However, not all particles are so lucky. Some move at such a shallow angle to the beampipe that they exit it beyond the detector. However, even these serve a useful purpose, in that they can be used to give us a precise measurement of the luminosity. This is accomplished by a luminosity monitor, consisting of four scintillator telescopes located on either side of the IP, as shown in Figure 3.3.

The particles involved are Bhabha-scattered electrons. Bhabhas are produced by electrons which either scatter or collide to produce another electron pair. Since by indistinguishability we can not tell the two processes apart, both channels contribute to the cross-section. The differential cross-section for this process [6] is:

$$\frac{d\sigma}{d\Omega} = \frac{\alpha^2}{8E^2} \frac{(2 - \sin^2\theta)(4 - \sin^2\theta)^2}{\sin^4\theta}, \tag{3.1}$$

using $0 < \theta < \pi$ for the angle from the beampipe. Thus, by knowing the number of Bhabha electrons at a given angle, we can determine the luminosity at the IP. The

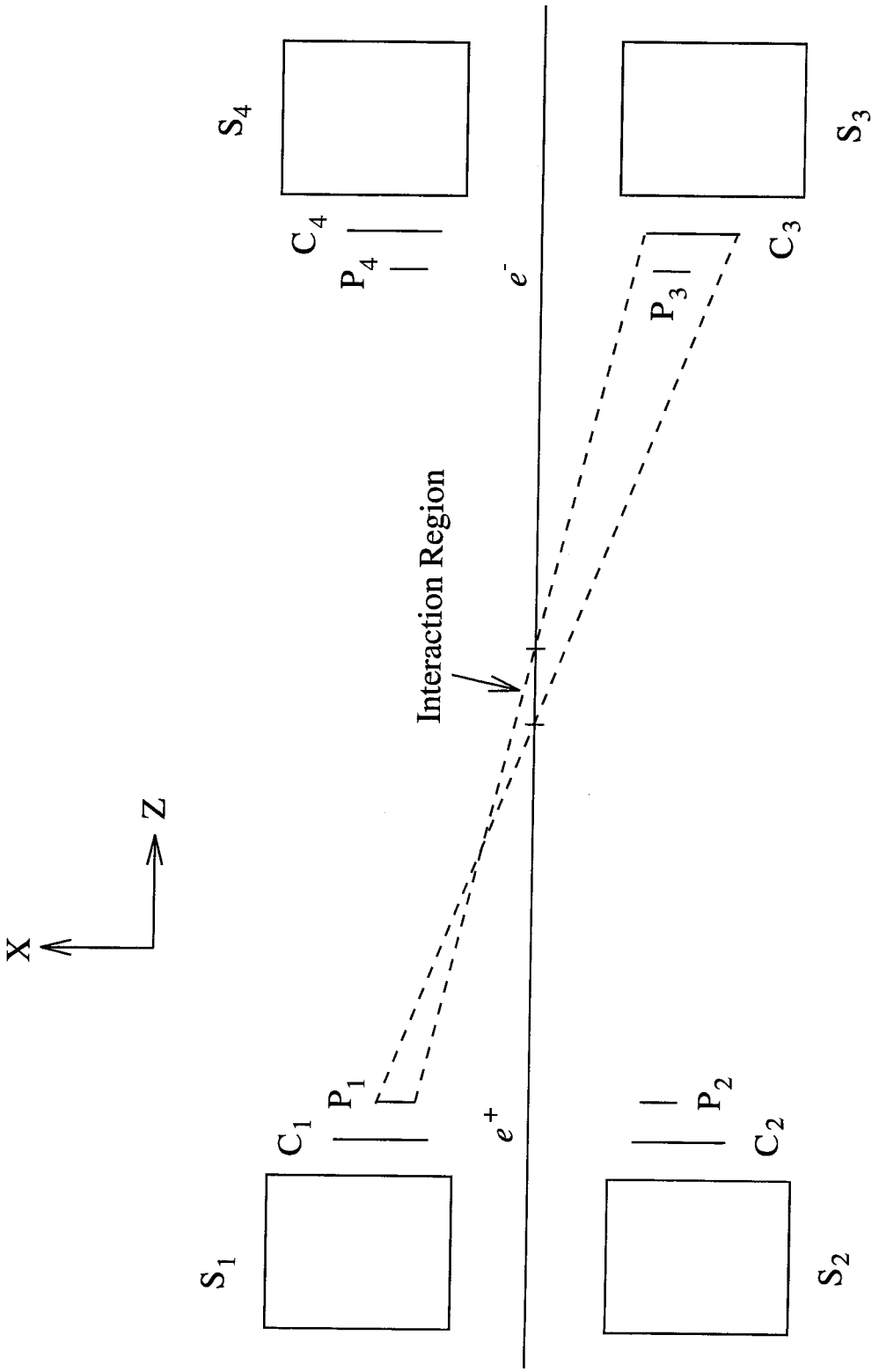

Figure 3.3: Luminosity monitor telescopes.

luminosity monitor measures small-angle Bhabhas, which are dominated by scattering with $\sigma \propto 1/\sin^4\theta$; wide-angle Bhabhas enter the detector, and are used for luminosity measurements and calibration by the offline reconstruction.

The luminosity monitor makes use of the fact that Bhabha electrons are produced symmetrically. The telescopes are arranged in two pairs, on either side of the beampipe. The system is triggered whenever two diametrically opposed telescopes both register a hit within 50 nsec of the beam crossing. This may also include some false coincidences, however. A second trigger counts coincidences between a monitor and its opposite number from the *previous* crossing, estimating the rate for false coincidences. A third trigger, which reads one out of every million crossings regardless, is used to measure random background, in case there is any intrinsic bias in the counters themselves.

Hits and coincidences are defined using the two pieces of scintillator (P and C) and the shower counter (S) associated with each telescope, shown in Figure 3.3. The scintillators provide a simple yes/no signal, indicating whether or not they were hit. The shower counter uses a photomultiplier tube[1] to measure the energy with a resolution of about 13% in this energy range. For the system to record a hit, the deposited energy must be within 3.5σ of the beam energy.

The telescopes are arranged symmetrically around the IP. However, since interactions actually take place in a finite region around the nominal IP, electrons can approach the two telescopes from slightly different angles. This is why there are two separate pieces of scintillator: as shown, the size of the C counter is carefully matched to subtend the possible angle of Bhabha events which ended up in the opposing P counter.

3.4 Central Drift Chamber

If the particle has sufficient transverse momentum, it will enter the detector and encounter the Central Drift Chamber, which is wrapped snugly around the beampipe.

[1] Actually located outside the magnetic field, and fed via light pipes.

The CDC is a gas-filled cylinder with a length of 110 cm, an inner diameter of 18.4 cm, and an outer diameter of 30.2 cm, covering a solid angle of 98% of 4π. It consists of four layers of 48 sense wires running axially, plus field wires which define a sense cell around it.

The idea of a sense cell is used throughout the detector whenever there is a region of gas, where the wires are at a high voltage. When a charged particle passes through the gas, it interacts electromagnetically to strip electrons from the gas molecules. Due to the electric field, the electrons in the region of the sense cell move towards a particular wire. This creates a large electric pulse, which travels down to both ends of the wire.

In the CDC, the gas is 89% Ar, 10% CO_2, 1% CH_4 and the voltage is nominally 2400 V. By noting which wire signalled, we could identify the transverse location with a σ_{xy} of 150 microns. By noting the height of the pulse at either end, we could estimate z with a σ_z of one centimeter. The CDC was not calibrated, so it was not useful for reconstruction, but it did serve an important role in the trigger.

3.5 Main Drift Chamber

In contrast to the CDC, the Main Drift Chamber was critical to the entire experiment. That is because the MDC is used to measure momentum, by carefully noting the curvature of particles in the magnetic field, via the formula $p_T(\mathrm{GeV}/c) = 0.3B(\mathrm{Tesla})R(\mathrm{meters})$. It also forms the heart of the detector by its size and complexity, with a length of 220.0 cm, an ID of 31.0 cm, and an OD of 230.0 cm, filled with the same gas as the CDC, but containing 19,380 wires and an electric field initially set to 850 V/cm.

Of these, 2808 are sense wires. Four sense wires stacked radially make up a sense cell, with the number of cells per layer ranging from 48 on the inside to 108 on the outside. There are ten layers, alternating between axial (along the detector) and stereo (skewed), allowing for more precise z measurements. The position measurements translate into a momentum resolution of $\sigma_p/p = 2.1\%\sqrt{1+p^2}$, with p in units

of GeV/c, since our curvature error increases for stiffer tracks.

In addition to position, the MDC also keeps track of the amount of energy deposited in the gas around each wire (dE/dx), which is a function of the velocity of the particle. dE/dx pulses have a full-width half-maximum resolution of 8.5%. This is generally compared against the predicted energy loss for different particle types traveling with that momenta, and quoted in terms of fractional σ. The amplification of the pulse height is strongly correlated to the voltage of the MDC. During the 1993 run, an excessively low voltage resulted in the loss of dE/dx information for many events, which renders those useless for our particular analysis.

Relative to the IP, the MDC takes up less solid angle with each layer. The track reconstruction software requires information from at least three layers before it will even attempt to fit a helix. At the second layer, the coverage is 96% of 4π, but this goes down to about 85% by the tenth and final layer.

3.6 TOF

Particles which make it through all ten layers of the MDC now enter the dedicated particle identification (PID) systems. Particles which slip out the sides early are caught by the analogous endcap systems, but those are not calibrated, and are thus only useful as checks rather than for identifying particles.

The first system encounted measures the time it takes for a particle to travel there from the IP, and then derives a velocity from this time-of-flight (TOF) and the path length (measured along the expected helix). The barrel TOF system consist of 48 trapezoidal pieces of scintillator, arranged in a cylinder covering 76% of 4π. Each is 284 cm long, 5 cm thick, and about 15 cm wide, with a photo-multiplier tube at each end to amplify the photons produced by incoming charged particles. It measures the time with a resolution that is nominally 300 psec, but in practice sits between 400 and 450 psec.

On each endcap, 24 2.5 cm thick rectangular counters, read out only on one end, form a ring with an ID of 75 cm and and an OD of 211 cm, slightly less than that

of the MDC. These endcap shower counters each cover a solid angle of 10% of 4π. In practice they were used not to measure TOF but merely to signal the presence of extraneous tracks.

3.7 Electromagnetic Calorimeter

Outside the TOF is the electromagnetic calorimeter, composed of shower counters (SCs) to measure energy deposited by electromagnetic interactions. It has a barrel (ID = 247.0 cm, OD = 338.2 cm, length = 385.0 cm) covering 80% of 4π and two endcaps (ID=74.6, OD=192.0, thickness = 41.0 cm) covering 7% each. However, for this experiment the endcap SC was not calibrated, so it was also used only for extraneous track detection.

Each shower counter consists of 24 layers, with 560 cells/layer in the barrel and from 174 to 190 cells/layer in the endcap. Each is composed of a lead plate followed by a gas counter, for a total of 12 radiation lengths. The gas in the counter is one part argon and two parts CO_2 bubbled through n-pentane at $0°C$. This operates at a higher voltage than the MDC, in self-quenching streamer mode, which makes the gas act as its own amplifier, trading some precision for simpler electronics. The resulting energy resolution is $\sigma_E/E = 25\%/\sqrt{E(\mathrm{GeV})}$, since we are counting the number of particles produced in an electromagnetic shower. The position resolution is $\sigma_\phi = 4.5$ mrad, $\sigma_z = 2$ cm in the barrel, and $\sigma_x = 0.7$ cm, $\sigma_y = 13\%L$ in the endcaps, where L is the tube length.

3.8 Muon System

Beyond the shower counter lie the magnetic coil and return flux. The material present in these two systems is used to absorb particles which interact strongly. Instruments embedded in the return flux mark the presence of those which nevertheless make it out this far. This is primarily of value in identifying muons, which is why it is called the muon system.

The only subsystem sitting outside the magnetic field, the muon tracking system is an octagonal structure consisting of three double layers of proportional counter tubes interleaved with the iron absorber of the flux return. The absorber and the magnet together capture most pions, allowing the counters to act as "yes" detectors for muons. The downside is that all muons with less than about 600 MeV of momentum are also stopped, limiting its usefulness. Total solid angle coverage is also only 68% of 4π. Still, within its limitations, the system is very useful, since pions and muons have very nearly the same mass and are difficult to distinguish any other way.

Each tube acts like a single sense cell, where charge division provides an estimate of the z position. The position resolution is $\sigma_z = 5$ cm, and $\sigma_{r\phi} = 3$ cm. During reconstruction, the software attempts to match up hits in the muon counter with tracks in the MDC, as it does with the TOF and SC systems.

3.9 Trigger

Determining whether all this information gets saved out to a tape is the job of the trigger. The beam crossing rate is 1.25 MHz, and cosmic rays contribute a few kHz, but there are only 0.2 to 5 good events per second. It takes 10 msec for the electronics to read out the detector, and another 20 msec for the VAX/785 to store the result, so even reading 3 events/second would give us a deadtime of 10%. The goal of the triggering system is to read out only those few events which have a high probability of representing interesting physics (as opposed to beam gas or cosmic rays). It uses fast hardware and simple logic on data feeds to estimate the response of various systems.

The interval between beam crossings is about 800 nsec, so the goal is to respond within that time frame. BES uses a multi-level trigger, with each level taking up one interval and responding to the previous level. The trigger rate after the first level is a few kilohertz, but drops to a few hertz after the second level. The first level checks time and location from the TOF system, and position in the CDC or SC, depending on whether it is charged or neutral. This is particularly important for eliminating cosmic rays. The second level uses the MDC to identify the number of tracks, and

the SC to examine energy deposition. The third-level does a detailed selection, to classify events as Bhabha, dimuon, charged, neutral, or cosmic.

For the D_s running, the charged, neutral and $D_s(2)$ triggers were used. The last is the one that was designed to capture physics of interest to us. The specific requirements were at least two hits in the barrel TOF, at least two tracks in the MDC, at least one hit in layer 3 or 4 of the CDC, and total shower counter energy above a given threshold[7].

Chapter 4 The Data

The BES Collaboration, consisting of various American and Chinese institutions, was formed in June of 1991, and published its first paper—a measurement of the tau mass—in November 1992. A history of BES running is shown in Table 4.1, along with nominal integrated luminosity. 1995 is a transitional year, with only a little ψ' running, as the D_s running has finished, and a major detector upgrade is planned for later this year.

4.1 Data Processing

The digitized detector readouts are transformed into physically interesting quantities via a process known as reconstruction. The main task in reconstruction is identifying the tracks from charged particles in the MDC, and deriving momenta from them. If possible, the tracks are fit to a full three-dimensional helix; otherwise, the momentum is derived from a circle fit in the x-y plane. These tracks are then associated with appropriately located hits in the TOF, SC, and muon systems. If a high-momentum track does *not* have a corresponding muon system hit, that informa-

Period	Purpose	Integrated Luminosity
9/89 - 1/90	Debugging and Calibration	3×10^5 J/ψ
1/90 - 6/90	First J/ψ Run	3×10^6 J/ψ
11/90 - 1/91	Second J/ψ Run	3×10^6 J/ψ
3/91 - 5/91	Third J/ψ Run	3×10^6 J/ψ
11/91 - 1/92	τ Mass Run	5.0 pb^{-1}
1/92 - 6/92	First D_s Run	3.3 pb^{-1}
12/92 - 5/3	Second D_s Run	7.1 (4.6) pb^{-1}
12/93 - 1/94	First ψ $(2S)$ Run	2.3 pb^{-1}
1/94 - 5/94	Third D_s Run	14.9 pb^{-1}
1/95 - 4/95	Second ψ $(2S)$ Run	4 pb^{-1}

Table 4.1: BES data taking runs.

tion is also recorded. Neutral tracks are identified by hits in the shower counter.

The conversion from voltages and wire numbers to energies and positions is handled by means of various calibration constants. These constants are adjusted for each run using Bhabha-scattered electrons and dimuons, which have a precise energy and a large, well-known differential cross section. Radiative Bhabhas, from $e^+e^- \rightarrow e^+e^-\gamma$, give electrons with a continuous range of energy to use for calibration. The expected response of PID systems to other particles is extrapolated from the electron or muon mass.

Large-angle Bhabhas are also used to confirm the luminosity associated with each run[8]. We examine the number of Bhabha events with $|\cos\theta| < x$, for $x = 0.60, 0.65, 0.70,$ and 0.748. The QED cross-section is calculated to be 247.2 nb, so knowing the angular distribution and the efficiencies allows us to determine the efficiency. Total systematic uncertainty is on the order of 2.5%, which is larger than the variance between results from the four different angular regions. We use the largest region since it has the best statistics.

Total integrated luminosity from all three years comes out to 25.35 ± 0.63 pb^{-1}. However, voltage problems in the MDC resulted in a large part of the 1993 data having improper dE/dx information. Since this would severely impact our ability to identify particles, events without usable dE/dx data were removed from the dataset. This results in 4.6 instead of 7.1 pb^{-1} for that run, giving an effective sample of 22.8 ± 0.6 pb^{-1}.

4.2 The Cross-Sections

The cross-sections for charmed meson production near threshold are still only poorly measured. The best theoretical predictions for their values come from the coupled-channel model of Eichten, *et al.* used by the Mark III collaboration[9]. The basic premise is that whenever a new channel opens, it gains cross-section at the expense of other channels. It is hoped that this would compensate for the relative difficulty, due the heavier mass of the strange quark, in producing a D_s meson instead of a D^0

Production	R	Cross-section	Events for 22.8 ± 0.6 pb^{-1}
$D_s^+ D_s^-$	$\approx$0.15	$\approx$0.8 nb	18×10^3
$D\overline{D}$	$\approx$0.02	$\approx$0.1 nb	2×10^3
$D^{*0}\overline{D}^0 + D^0\overline{D^*}^0$	$\approx$0.60	$\approx$3.2 nb	73×10^3
$D^{*\pm}D^{\pm}$	$\approx$0.65	$\approx$3.5 nb	79×10^3
$D^{*0}\overline{D^*}^0$	$\approx$0.75	$\approx$4 nb	90×10^3
$D^{*+} - D^{*-}$	$\approx$0.75	$\approx$4 nb	90×10^3

Table 4.2: Coupled-channel model predictions at 4.03 GeV.

or $D^{\pm}$.

The Mark III coupled-channel model predictions for charmed meson cross-sections are shown in Figures 4.1 and 4.2, taken from Ref [9]. R is the ratio of hadronic to dimuonic production rates, $\sigma_{HAD}/\sigma_{\mu\mu}$, at a given energy. From the formula $\sigma = \frac{86.8 Q_f^2 \text{nb}}{s(\text{GeV}^2)}$[1], we obtain $\sigma_{\mu\mu} = 5.34$ nb at 4.03 GeV. From these plots, we can estimate the cross-sections for charm decays at 4.03 GeV. Those, and the expected events for 22.8 ± 0.6 pb^{-1}($N = \sigma\mathcal{L}$), are summarized in Table 4.2.

BES decided to run at 4.03 GeV, where the coupled-channel model predicts an enhancement in the D_s production rate, to somewhat less than 1 nb. At this energy, each D_s has an energy of 2.015 GeV, which corresponds to a momentum of 430 MeV. This is different from Mark III, which ran at 4.14 GeV, above the threshold for $D_s^* D_s$ production. That has a larger cross-section, but reconstruction is harder due to uncertainty in the energy of the D_s produced from D_s^* decay.

4.3 The Hadronic Strip

The D_s dataset comprises data taken at an energy of 4.03 GeV during 1992, 1993, and 1994. It was analyzed at the High Performance Computer Center (HPCC) of the Texas National Research Laboratory Commission (TNRLC). The full dataset was broken up into various pieces for different physics and diagnostic analyses. To identify events which potentially contained hadronic charm events (as opposed to Bhabhas, dimuons, or cosmic rays), we used the following definitions:

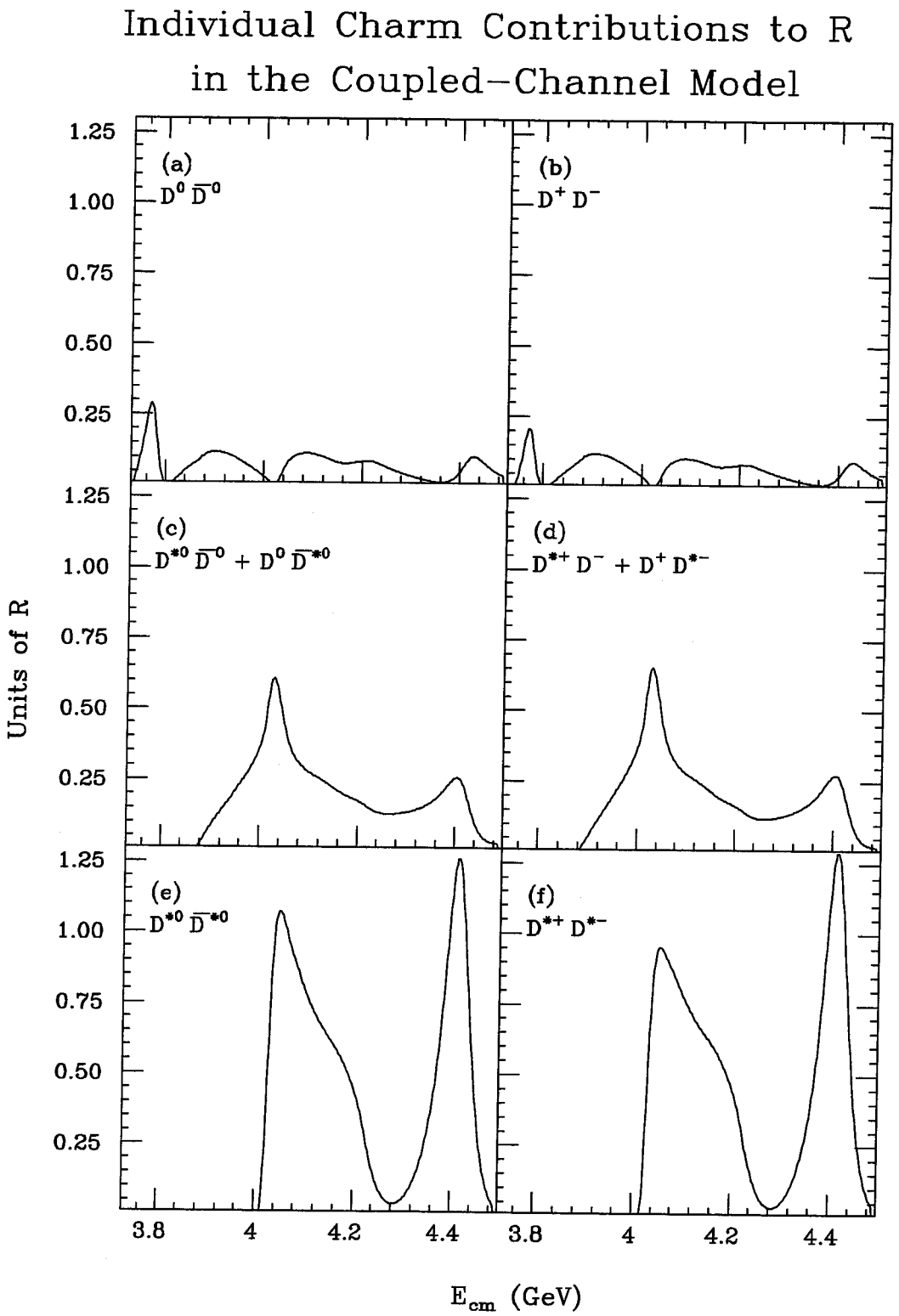

Figure 4.1: Cross-sections for D meson production relative to dimuon production.

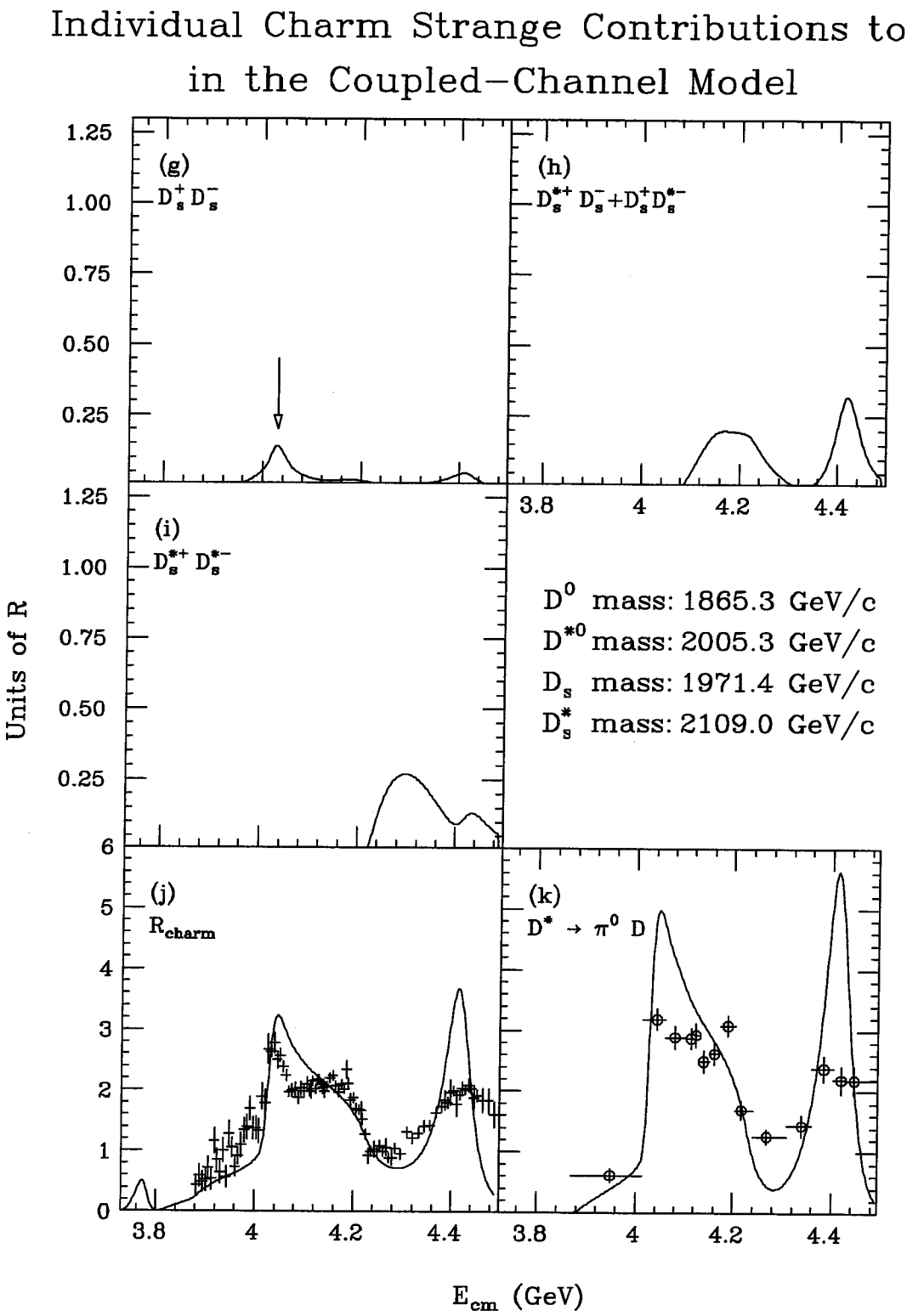

Figure 4.2: Cross-sections for D_s meson production relative to dimuon production.

Type of Cut	Cut
Momentum	$P_{scalar} > 1.5$ GeV
Vertex	$V_{xy} < 0.02$ m, $\|V_z\| < 0.2$ m
Charged Track	$N_{charged} < 12$ or $P_{scalar} < 10$ GeV
Usable Track	$N_{usable} \geq 3$ or $N_{gamma} \geq 2$

Table 4.3: Hadronic strip cuts.

- *charged track:* Contains main drift chamber information, and a momentum of $P < 4.0$ GeV.
- *good track:* A charged track with a successful helix fit.
- *usable track:* A charged track with either a helix or a circle fit.
- *isolated neutral:* A neutral track (cluster of shower counter hits) with $E > 50$ MeV with $\cos\theta < 0.97$ away from the nearest charged track.
- *Vertex (V):* Weighted average of the DCA (Distance of Closest Approach) of good tracks.
- *Scalar Momentum Sum (P_{scalar}):* The scalar sum of the magnitudes of the momenta for all charged and isolated neutral tracks.

Based on these definitions, the cuts in Table 4.3 were made. These were carefully studied to ensure that they did not reject any actual charm events. The resulting dataset, called the hadronic strip, was made available to the collaboration for different analyses. One such analysis is described in the final part of this thesis.

Part III

Expectations

Chapter 5 Experimental

This chapter covers the current experimental situation, and provides predictions for the number and type of events we might expect to see. The following chapter compares this with theoretical models for the D_s.

5.1 Decay Rates

Our best information on the D_s comes from the CLEO experiment at Cornell[10]. CLEO's accelerator, CESR, runs at the $\Upsilon(4S)$ to produce B mesons. These then decay to produce various charmed mesons, which can be studied in large quantities. However, this only allows direct measurements of relative branching fractions.

Historically, branching fractions are measured relative to $B(D_s^+ \to \phi\pi^+)$, as that is the easiest mode to measure accurately by identifying the decay $\phi(1020) \to K^+K^-$. To obtain an absolute measurement of that mode requires making model-dependent assumptions about the production cross-section, the semileptonic branching fractions, or the ratio $D_s \to \phi\pi\ /D \to K^*\pi$. The backgrounds make measuring missing energy difficult, complicating neutrino identification.

By way of contrast, threshold pair-production provides a clean way to measure absolute branching fractions with great precision. Unfortunately, the $c\bar{c}$ production rate above D_s threshold is much smaller than that from B decay at the $\Upsilon(4S)$. This leads to very poor statistics. Mark III[11, 12] found no events despite searching several resonant decay modes, but established a 90% confidence level for $B(D_s^+ \to \phi\pi^+) < 4.1\%$ using 6.30 ± 0.46 pb^{-1}of data at 4.14 GeV. Previous work using the BES data[13] and searching for resonant two-body decays led to two double-tags, which was combined with a single-tag sample for a result of $B(D_s^+ \to \phi\pi^+) = 4^{+10}_{-2}$, and an estimate of $\sigma(e^+e^- \to D_s^+D_s^-) \approx 200$ pb.

However, by dint of their sheer number of events, sophisticated detector, and

Mode	Ratio to $\phi\pi$	Fraction (%)
$\phi\pi^+$	1.0	3.5 ± 0.4
$\phi l^+\nu_l$	0.54 ± 0.05	1.88 ± 0.29
$\eta l^+\nu_l + \eta'(958) l^+\nu_l$	3.9 ± 1.6 (to $\phi l^+\nu_l$)	7.4 ± 3.2
$K^+\overline{K}^0$	1.01 ± 0.16	3.5 ± 0.7
$K^+K^-\pi^+(total)$	1.37	4.8 ± 0.7
$K^+\overline{K}^*(892)^0$	0.95 ± 0.10	3.3 ± 0.5
$K^+K^-\pi^+(NR)$	0.25 ± 0.09	0.87 ± 0.32
$K^*(892)^+\overline{K}^0$	1.2 ± 0.3	4.2 ± 1.0
$\pi^+\pi^-\pi^+$	0.39 ± 0.08	1.35 ± 0.31
$\phi\rho^+$	1.8 ± 0.6	6.4 ± 1.7
$K^*(892)^+\overline{K}^*(892)^0$	1.6 ± 0.6	5.6 ± 2.1
$\eta\pi^+$	0.5 ± 0.1	1.9 ± 0.4
$\eta'\pi^+$	1.4 ± 0.4	4.7 ± 1.4
$\eta\rho^+$	2.8 ± 0.5	10.0 ± 2.2
$\eta'\rho^+$	3.4 ± 1.0	12.0 ± 3.0

Table 5.1: PDG values for principal D_s decay modes.

careful analysis, CLEO has used indirect D_s production to make precise measurements of numerous relative branching fractions, both hadronic and semileptonic modes. They have even stretched the theory to estimate the absolute $\phi\pi$ branching ratio at $B(D_s^+ \to \phi\pi^+) = 3.1 \pm 0.6^{+0.9}_{-0.6} \pm 0.6\%$. [14]. Their work forms much of the basis for the Particle Data Group's summary[1], which yields $B(D_s^+ \to \phi\pi^+) = 3.5 \pm 0.4\%$. Table 5.1 lists various two- and three-body modes of interest. We follow the convention of indicating decays of the D_s^+, with the understanding that the decays of the D_s^- are their charge conjugates.

5.2 Reconstruction Rates

To estimate what we expect to see at BES, we will use the PDG branching fractions and the coupled-channel model cross-sections. We will focus on Cabbibo-allowed decays that result in charged tracks, since those are the easiest to measure precisely. We will also restrict ourselves to decays with no more than three tracks. We will also consider semileptonic modes with three charged tracks plus one neutrino. These are

Decay Mode	Initial Fraction (%)	Final State	Percentage in State	Final Fraction (%)
Hadronic 3-prong D_s decays				
$\phi\pi^+$	3.5	$(K^+K^-)\pi^+$	49	1.7
$\overline{K}^{*0}K^+$	3.5	$K^+(K^-\pi^+)$	67	2.3
$K^+K^-\pi^+$	0.87	$K^+K^-\pi^+$	100	0.87
$K^+K_S^0$	3.3	$K^+(\pi^-\pi^+)$	33	1.1
Semileptonic D_s decays				
$\phi l^+\nu$	1.88	$(K^+K^-)l^+$	49	0.94

Table 5.2: Three-prong decays of the D_s.

Decay Mode	Initial Fraction (%)	Final State	Percentage in State	Final Fraction (%)
D_s decays including π^0				
$K^{*+}\overline{K}^{*0}$	5.6	$(K^+\pi^0)(K^-\pi^+)$	$(33)(67) = 22$	1.24
$\phi\rho^+$	6.5	$(K^+K^-)(\pi^+\pi^0)$	49	3.2
$D^\pm$ decays				
D^0	—	$K^-\pi^+$	4	—
D^+	—	$K^+K^-\pi^+$	1	—

Table 5.3: Background decays of the D_s $D^\pm$, and D^0.

shown in Table 5.2, with important background modes shown in Table 5.3.

The general formula for the number of events we expect in any given final state $\{i, j\}$ is

$$N_{ij} = \sigma(e^+e^- \to D_s^+D_s^-)\mathcal{L}B_iB_j = N_{D_s^+D_s^-}B_iB_j \tag{5.1}$$

where $\sigma(e^+e^- \to D_s^+D_s^-)$ is the cross-section for D_s pair production, $\mathcal{L}$ is the total integrated luminosity and B_i is the absolute D_s branching fraction to mode i. From Table 4.2 we have an estimate for the number of D_s pairs produced, $N_{D_s^+D_s^-} = 18,000$ events. We recast this in terms of the branching fractions relative to $\phi\pi$,

$$b_i = B_i/B(D_s^+ \to \phi\pi^+) \tag{5.2}$$

giving:

$$N_{ij} = N_{D_s^+D_s^-}B(D_s^+ \to \phi\pi^+)B(D_s^+ \to \phi\pi^+)b_ib_j = N_{\phi\pi\phi\pi}b_ib_j, \tag{5.3}$$

	$\phi\pi^-$	K^-K^{*0}	$K^-K^+\pi^-$	$K^-K_S^0$	$\phi e^-\bar{\nu}+\phi\mu^-\bar{\nu}$
$\phi\pi^+$	22.0 (5.3)	20.9 (6.8)	5.5 (2.7)	22.3 (3.8)	23.8 (5.7)
$\overline{K}^{*0}K^+$	20.9 (6.8)	19.9 (8.8)	5.2 (3.5)	21.2 (4.8)	22.6 (7.4)
$K^+K^-\pi^+$	5.5 (2.7)	5.2 (3.5)	1.4 (1.4)	5.6 (1.9)	6.0 (2.9)
$K^+K_S^0$	22.3 (3.8)	21.2 (4.8)	5.6 (1.9)	22.6 (2.6)	24.1 (4.1)
$\phi e^+\nu+\phi\mu^+\nu$	23.8 (5.7)	22.6 (7.4)	6.0 (2.9)	24.1 (4.1)	25.7 (6.2)

Table 5.4: Expected number of events in signal modes for $N_{\phi\pi\phi\pi}=22$. The expected number that would end up in three-prong versus three-prong final states is shown in parentheses.

where the number of $\phi\pi$ pairs produced is

$$N_{\phi\pi\phi\pi} = N_{D_s^+D_s^-}B(D_s^+\to\phi\pi^+)B(D_s^+\to\phi\pi^+) \quad (5.4)$$

$$= \sigma(e^+e^-\to D_s^+D_s^-)\mathcal{L}B(D_s^+\to\phi\pi^+)^2. \quad (5.5)$$

We will make use of these formulas in Chapter 9 to measure the cross-section.

From the coupled-channel model and $B(D_s^+\to\phi\pi^+)=3.5\%$, we estimate $N_{\phi\pi\phi\pi}=22$ events. Using this and the relative branching fractions gives us the predictions shown in Table 5.4. We follow the practice of combining results from the $\phi e^+\nu$ and $\phi\mu^+\nu$ channels. Note that the lower diagonal is the charge conjugate of, and equal to, the upper diagonal, but is still counted separately.

As a first order approximation, we can assume the probability to reconstruct and properly identify a given track is about 85%.[1]. For a six-prong event, the overall efficiency must therefore be below 40%. Thus, we are unlikely to detect very many events, especially after we introduce additional cuts to remove background. However, we should be able to reconstruct a few events, allowing us to improve on the Mark III results.

Another problem is that slow kaons will decay in flight, usually producing muons. The D_s is produced with only 430 MeV, corresponding to a Lorentz boost of $\beta\gamma=.22$. The K^* and ϕ are both produced with $\beta\gamma\approx 0.7$, and the daughter kaons have $\beta\gamma=0.6$ and 0.25, respectively. The kaon from the K^* will not slow down very

[1]This is an empirical observation, though roughly correlated to the solid angle covered by the PID systems.

much unless it is moving directly backward from its parent. For the ϕ, however, one kaon will always be moving relatively backward. An average boost of 0.7 gives a decay length of only 260 cm. Since the particle travels in a helix, it could easily decay inside the drift chamber, severely confusing the reconstruction and particle ID systems.

While this calculation needs to be verified using Monte Carlo simulations, it does imply that the $\phi\pi$ mode will be suppressed relative to $\overline{K}^{*0}K^{+}$, by as much as a factor of two. This will not only decrease efficiency, but also complicate relative branching fraction calculations.

Chapter 6 Theoretical

For comparison with those experimental measurements, we will use the factorization model developed by Bauer, Stech, and Wirbel (BSW), as it is one of the simplest, and makes specific predictions for D_s decays. In this the author is greatly indebted to Chris Matthews[15] for the lucid description and detailed predictions in his thesis.

6.1 Weak Decays

Let us start by examining the tree-level diagrams associated with D_s decay[16], as shown in Figure 6.1. It is important to remember that quarks possess an extra color degree of freedom, and therefore a $W^{\pm}$ will naively decay to them three times as often. However, the color of quarks produced by $W^{\pm}$ decay—or from the vacuum—is not correlated with that of the original quarks, but with each other, resulting in color-suppression of the hadronization process. Also, since many of the diagrams can end up with the same final state particles, we have to worry about interference due to their relative phases and amplitudes.

The first mode is annihilation, followed by the equivalent t-channel process known as $W^{\pm}$ exchange. Since the strange and charm quarks are primarily members of the same weak doublet, the annihilation mode is Cabbibo allowed. The exchange diagram, on the other hand, must be suppressed on at least one side, and hence is less significant.

The annihilation diagram is extremely interesting in the case of leptonic decays of the $W^{\pm}$. Since that is the only process that can produce purely leptonic one-prong decays, it is a very straightforward way to measure the decay constant. It is less interesting for the sort of two-body, three-prong decays we are interested in, as the amount of available energy will tend to pop multiple non-resonant hadrons out of the vacuum. It is also impossible for this mode to produce semileptonic decays at

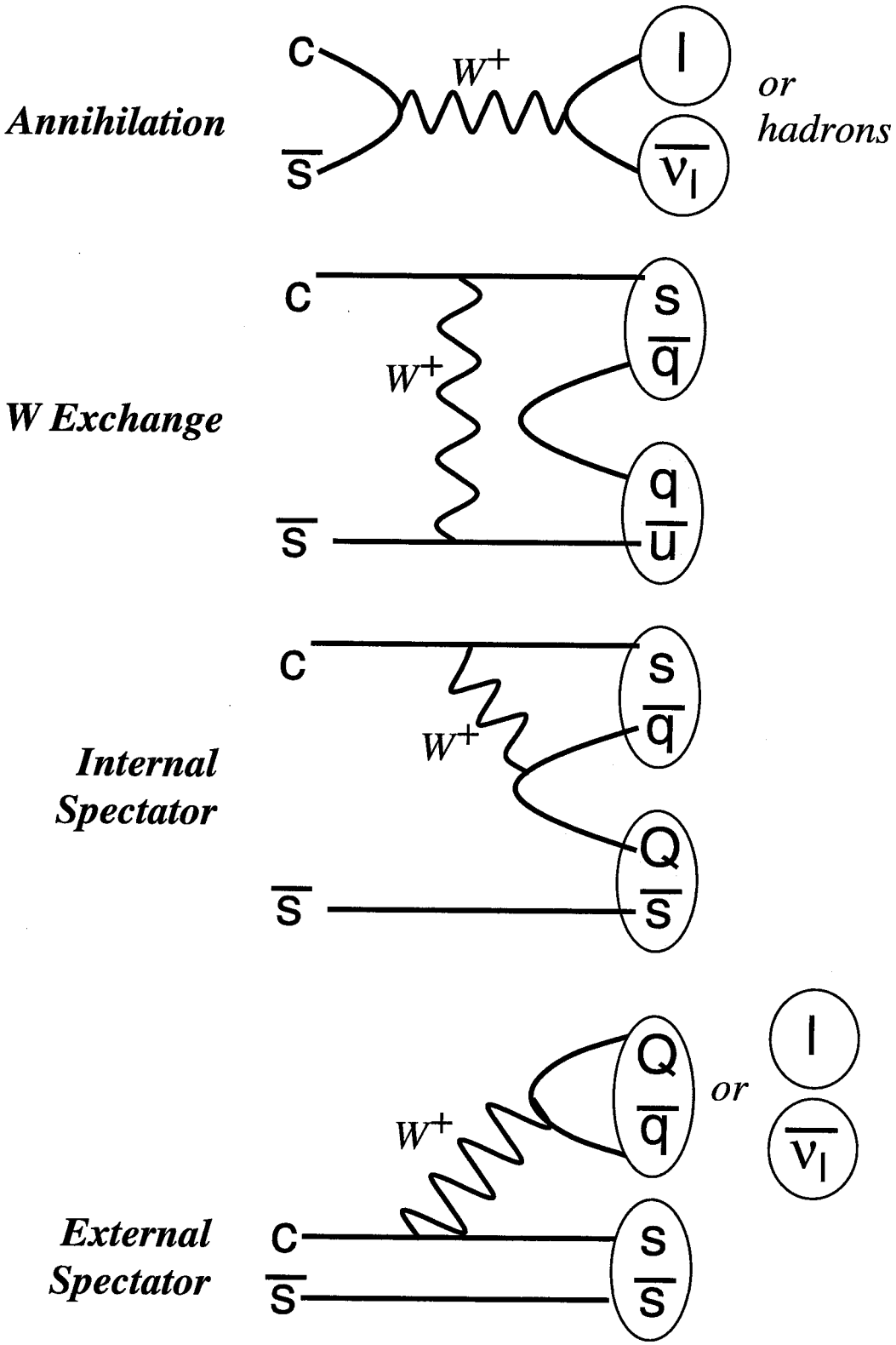

Figure 6.1: Weak decay processes.

tree-level.

Our strongest interest is reserved for the Cabbibo-allowed spectator decays, where the heavier charm decays to a strange while the initial strange quark passively watches. If the $W^{\pm}$ decays to leptons, or to quarks which form their own hadron(s), it is considered external. An internal decay is one where the quarks from the $W^{\pm}$ hadronize with the two s quarks, despite the color suppression.

The important thing to remember is that these are just the simplest tree-level diagrams. Additional diagrams not only contain more weak vertices, but also divergent gluon loops. Thus, we can not directly calculate the width for any of these processes. However, by observing some of the symmetries present in tree-level and single loop diagrams, we can parametrize our ignorance, and attempt to build a reasonable model.

6.2 The Factorization Model of BSW

One such model is that of BSW[17, 18, 19, 20], which focuses on spectator decays. Annihilation and exchange processes are either ignored or added in by hand later. They start by assuming that the dominant decay is the Cabbibo-allowed charm to strange transition. This process can be drawn purely in relation to the $W^{\pm}$, as shown in Figure 6.2. The $W^{\pm}$ can either decay to leptons, as shown on top, or to hadrons. The latter process also includes diagrams for hard gluon exchange, as illustrated below.

6.2.1 Semileptonic Decays

We will start with semileptonic decays, as they are easier to calculate. The Hamiltonian is $H = \frac{G_F}{\sqrt{2}} L^{\mu} J_{\mu}$, where the left-handed lepton current is $L^{\mu} = \bar{u}(\nu) W^{\mu} v(l^{+})$ and the left-handed hadronic current is $J_{\mu} = \bar{s}' W_{\mu} c$. The $W_{\mu} = \gamma_{\mu}(1 - \gamma_5)$ projects out the left-handed component, and can be elided by defining $(\bar{s}c)_L \equiv \sum_i^{N_c} \bar{s} W_{\mu} c$, where $N_c = 3$ is the number of colors. We can replace the weak eigenstate $\bar{s}'$ with the Cabbibo-favored component of the mass eigenstate $V_{cs}\bar{s}$. To calculate the amplitude

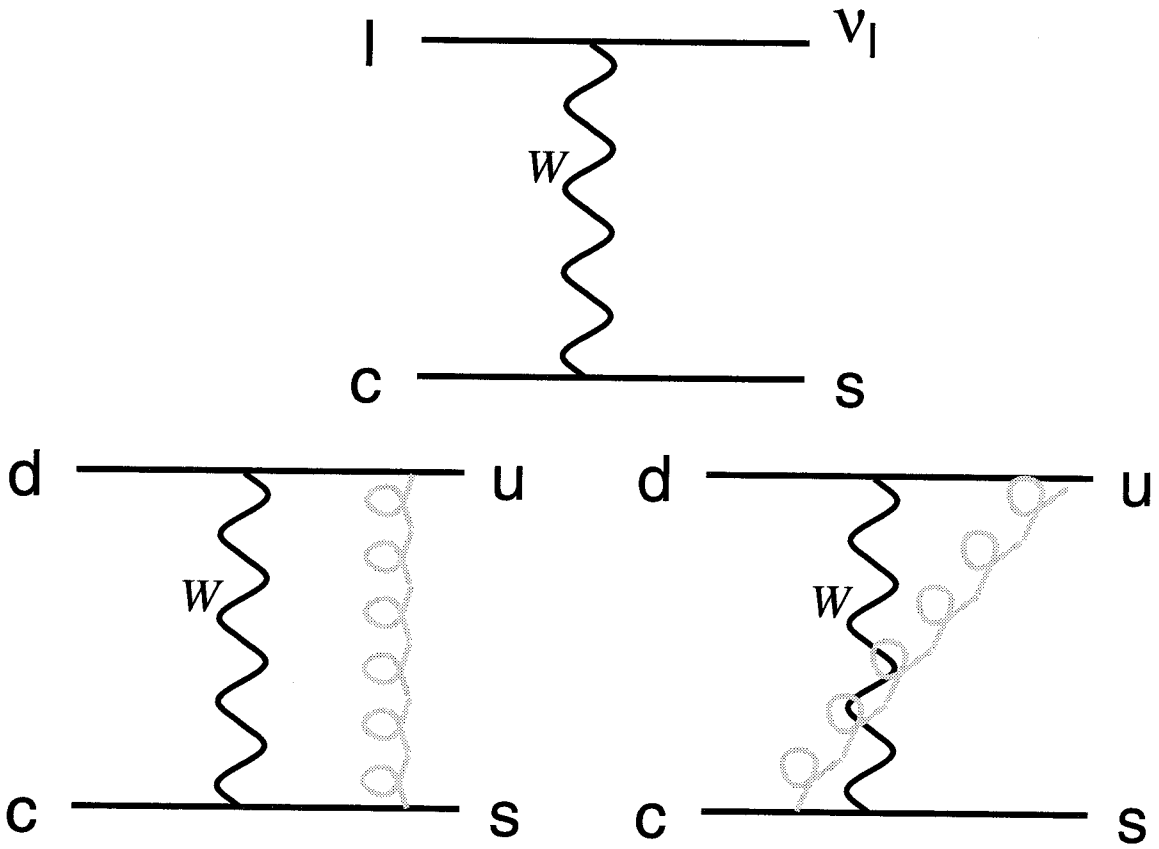

Figure 6.2: BSW hadronic charm decays.

for a process like $D \rightarrow Xl\nu$, we therefore need to evaluate the matrix element:

$$A(D \rightarrow Xl\nu) = \langle Xl\nu | \frac{G_F}{\sqrt{2}} L^\mu J_\mu | D \rangle \tag{6.1}$$

We can simplify this in two ways. First, since the leptonic and hadronic currents do not interfere with each other, we can use factorization to split them up, giving:

$$A(D \rightarrow Xl\nu) = \frac{G_F}{\sqrt{2}} \langle l\nu | L^\mu | 0 \rangle \langle X | J_\mu | D \rangle \tag{6.2}$$

That is, the D turns into an X, and the leptons are created from the vacuum.

At this point, rather than continuing to work with quark currents, BSW switches over to hadrons. The hadronic part of the current now becomes $\langle X | (\bar{s}c)_H | D \rangle$. This can be expressed in terms of the spin-parity and four-momenta of X, D, and the current q (plus the polarization of X, if any).

The only term that does not come directly from symmetry arguments is the hadronic form factor $F(q^2)$, which is different for each spin-parity state. This term is assumed to have the form:

$$F(q^2) = \frac{h}{1 - q^2/m^2} \tag{6.3}$$

dominated by a pole at the nearest resonance of mass m with the proper spin-parity and flavor content, with a decay constant of h. The decay constant, the form factor at $q = 0$, is calculated using bound states of relativistic harmonic oscillators, in an infinite momentum frame where the momenta of the light quarks is small relative to the heavy quark. This also requires assumptions about the appropriate resonances, some of which are not known and have to be inferred. Given that, however, the calculations are straightforward, if tedious.

6.2.2 Hadronic Decays

BSW now apply the same techniques to hadronic decays. The basic Hamiltonian is

$$H_W^0 = \frac{G_F}{\sqrt{2}} (\bar{s}' W_\mu c) \times (\bar{u} W^\mu d') \tag{6.4}$$

Replacing the W_μ and both quark fields, as before, gives:

$$H_W^0 = \frac{G_F}{\sqrt{2}} V_{cs} V_{ud} (\bar{s}c)_L (\bar{u}d)_L \tag{6.5}$$

When we add in tree-level hard gluon exchanges, like the one shown above plus their mirror images, we get an additional Hamiltonian which looks like:

$$H_W^1 = A \frac{G_F}{\sqrt{2}} V_{cs} V_{ud} [(\bar{s}c)_L (\bar{u}d)_L - 3(\bar{s}d)_L (\bar{u}c)_L] \tag{6.6}$$

where $A = \frac{\alpha_s}{8\pi} \ln \frac{M_W^2}{\mu^2}$ is the effective strong coupling constant at this energy.

Adding them together, and dropping the ubiquitous L subscript gives:

$$H_W = \frac{G_F}{\sqrt{2}} V_{cs} V_{ud} [c_1 (\bar{s}c)(\bar{u}d) + c_2 (\bar{s}d)(\bar{u}c)] \tag{6.7}$$

which is in fact the general form. Higher order corrections merely change the values of the c_i, which can be calculated using renormalization group techniques. Switching over to hadronic currents gives us:

$$H_{eff} = \frac{G_F}{\sqrt{2}} V_{cs} V_{ud} [a_1 (\bar{s}c)_H (\bar{u}d)_H + a_2 (\bar{s}d)_H (\bar{u}c)_H] \tag{6.8}$$

Naively, we might expect to fix $a_1 = c_1 + \frac{1}{N_c} c_2$, and vice versa, corresponding to the color-suppression of the internal spectator diagram. However, the a_i (or, equivalently, N_c) are treated as free parameters by BSW. The amplitude for the transition from an initial charmed quark D to the two-body system XY is now proportional to:

$$\langle XY | H_{eff} | D \rangle \propto a_1 \langle XY | (\bar{s}c)_H (\bar{u}d)_H | D \rangle + a_2 \langle XY | (\bar{s}d)_H (\bar{u}c)_H | D \rangle \tag{6.9}$$

Now, semileptonic decays are inherently factorizable. BSW makes the further assertion that all hadronic decays can also be factorized, ignoring weak annihilation, and deferring final-state interactions. So, the two body decays become:

$$a_1 \langle Y | (\bar{u}d)_H | 0 \rangle \langle X | (\bar{s}c)_H | D \rangle + a_2 \langle X | (\bar{s}d)_H | 0 \rangle \langle Y | (\bar{u}c)_H | D \rangle \tag{6.10}$$

Parameter	Value
a_1	$+1.13 \pm 0.03$
a_2	-0.47 ± 0.03
ρ_{a_1,a_2}	-51%

Table 6.1: BSW Parameters

Name	Predicted (%)	Measured (%)
$\phi\pi$	2.7 ± 0.1	3.5 ± 0.4
$\overline{K}^{*0}K^+$	1.5 ± 0.2	3.3 ± 0.5
$K^{*+}\overline{K}^0$	1.5 ± 0.2	4.2 ± 1.0
$K^+\overline{K}^0$	1.25 ± 0.02	3.5 ± 0.7
$\eta\pi^+$	2.8 ± 0.15	1.9 ± 0.4
$\eta'\pi^+$	1.64 ± 0.09	4.7 ± 1.4
$\eta\rho^+$	5.3 ± 0.3	10.0 ± 2.2
$\eta'\rho^+$	1.49 ± 0.08	12.0 ± 3.0
$\phi l^+\nu$	3.47	1.88 ± 0.29
$\eta l^+\nu$	2.05	7.4 ± 3.2
$\eta' l^+\nu$	0.58	(for both)

Table 6.2: BSW predictions for D_s decay modes, compared with measured branching fractions from Ref [1].

That is, the first term turns D into X and pops Y out of the vacuum, while the second does the opposite. These can be decomposed in the same way as the currents from semileptonic decay.

6.2.3 Results

This allows us to obtain predictions for the widths of any two-body charm decay in terms of a_1 and a_2. The effect of final-state interactions can be derived from the correlations between these two. The values for these numbers used in Ref. [15] are shown in Table 6.1, giving the predictions in Table 6.2. Generally, the parameters are fixed by measuring the decay widths for the different charge states of $D \to K\pi$. These values were calculated using older values for those branching fractions, but the net change is less than one sigma, although the error bars would be smaller. Of course, the semileptonic results are independent of the a_i, and hence the same as before.

BSW predictions are fairly close for a large number of modes, especially considering how few free parameters are used. However, it can be seen that it it falls short in several key channels. In particular, it is significantly off in the key KK and $\phi l\nu$ channels. The last is particularly damning, as it is precisely that sort of semileptonic Cabbibo-allowed decay where factorization is expected to function well.

Because of this, there is a continuing search for better models. The factorization hypotheses is generally well accepted, so the quest focuses on improved form factors. Isgur *et al.*[21], criticize BSW for using infinite-momentum frame wave-functions, which they claim are poorly understood. They also dislike extrapolating from a region where the form factor is small, $q = 0$, to where it is large, $q = m$. They prefer to start in the zero recoil ($q = m$) limit, and use a non-relativistic quark potential. Their analysis suffers from having to add relativistic effects in *ad hoc*; more recent attempts have been made using relativistic formalisms like the bag model[22]. None of those models have yet produced predictions for exclusive hadronic decays as detailed as those from BSW, so we will continue to use that for this thesis.

Part IV

The Analysis

Chapter 7 The Analysis

The goal of our analysis is to prepare a sample of doubly-tagged D_s mesons with high efficiency and low background. Our primary background is from pair-produced charmed meson which do not contain strange quarks. Therefore, our focus will be on events with a high strangeness. For hadronic decays, this means events with at least three kaons. For semileptonic decays, which presumably come via external spectator processes, we require two kaons on the same side as the missing neutrino.

We will attempt to fully reconstruct events containing six charged tracks, since the D_s primarily goes to three-body final states. Using charged tracks gives us good momentum resolution, which allows us to make effective use of kinematic fitting. By using the beam energy constraint, we hope to discriminate against decays where one or more low-momenta photons are swallowed by the beampipe, such as from a D^* or $D_s \to X\pi^0$. These are particularly difficult to distinguish from events with a missing neutrino.

We check the consistency of the event against all potential hypotheses, both signal and background. Particle identification is handled by calculating a χ^2 for how well all six tracks match a given hypothesis. This χ^2 is then added to the χ^2 from the kinematic fit, allowing us to incorporate all the information into a single variable.

This chapter discusses the algorithms and cuts used to implement this scheme and produce an n-tuple. The next chapter applies simple cuts to produce a double-tag sample, then analyzes the efficiencies and backgrounds. The final chapter covers the physically interesting parameters derived from that sample.

7.1 Datasets

The analysis was performed on the cumulative D_s dataset from all three years. A preselection cut was imposed to only examine those events which had good dE/dx

Channel	Number
D_s Hadronic vs. Hadronic	1000 each
D_s Hadronic vs. Semileptonic	1000 each
D_s Hadronic vs. D_s including π^0	1000 each
D^* Cocktail vs. $D^0 \to K^-\pi^+$	10,000
D^* Cocktail vs. $D^+ \to K^+K^-\pi^+$	10,000

Table 7.1: Monte Carlo datasets generated.

information. Several Monte Carlo (MC) simulations were analyzed in the same fashion, to calibrate our analysis. We simulated all the modes listed in Table 5.2. The various D_s modes were decayed against the different hadronic modes. The D modes were decayed against D^* cocktail, which contains the different decay modes in the appropriate fraction. The number produced for each type is shown in Table 7.1.

7.2 Track Selection

Candidate double-tag events should contain six usable charged tracks (three positive and three negative), and no isolated neutral tracks. We use the same definitions of "usable" and "isolated" used in Section 4.3 for the hadronic strip. While real events must of course conserve charge, we do not impose it as a constraint at this time. Rather, we only require that there be six charged tracks. We use events with non-zero net charge to estimate background from high multiplicity events with lost tracks. By knowing how many appear with the wrong net charge, we can deduce how many masquerade as real events. For such events, we arbitrarily swap the sign of enough tracks to balance the charge, then treat it as a normal event.

Figure 7.1 shows the number of charged and neutral tracks per event, plus separate plots for events with and without charge balance. Figures 7.2 and 7.3 show the hadronic and semileptonic signal Monte Carlos, whereas the backgrounds from D^* and D_s including π^0 are shown in Figures 7.4 and 7.5. The comparable numbers of balanced and unbalanced events indicate a large amount of trickle down due to lost tracks at this stage.

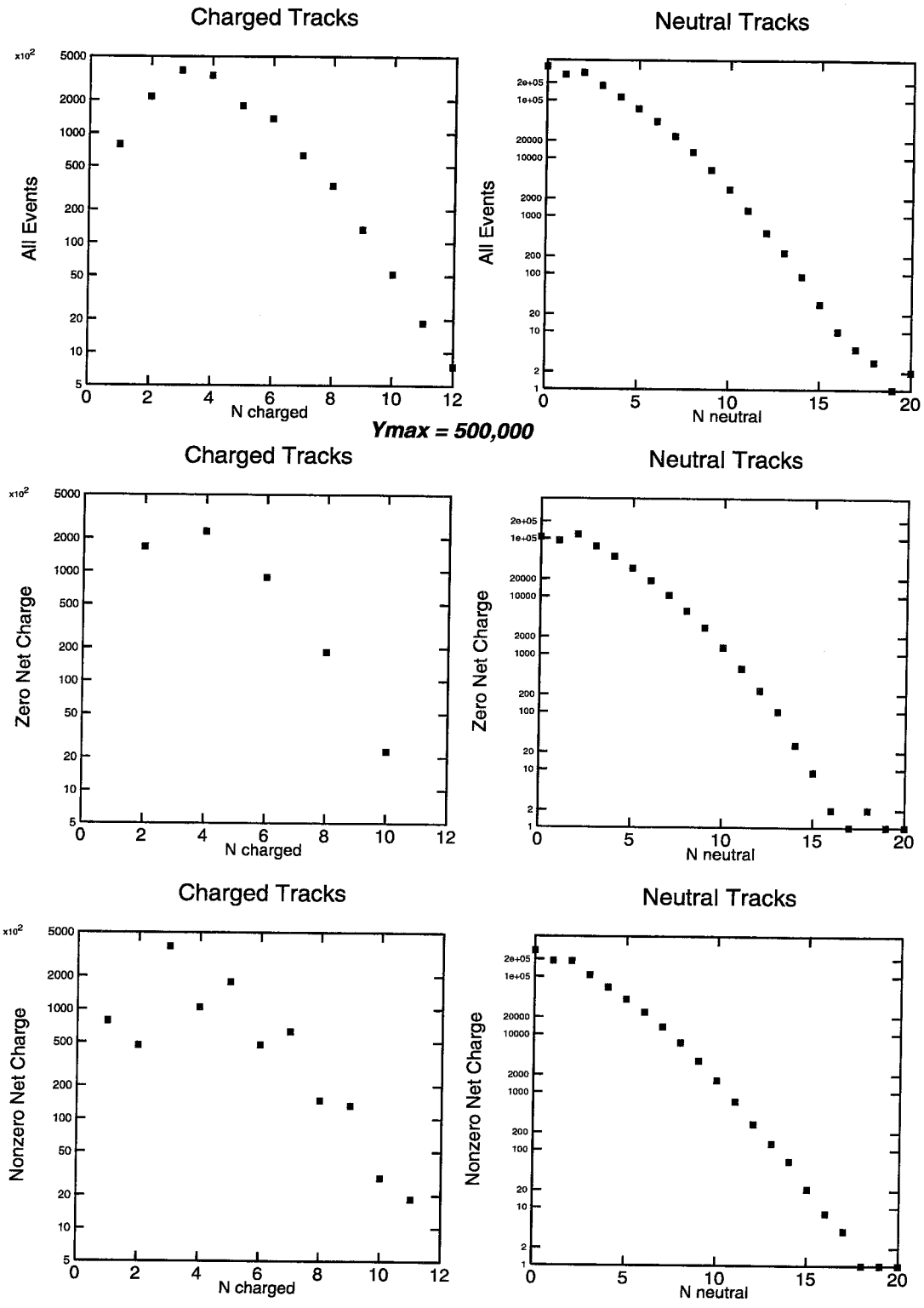

Figure 7.1: Number of charged and neutral tracks in real data. The first row contains all events, the second and third those with and without charge balance, respectively.

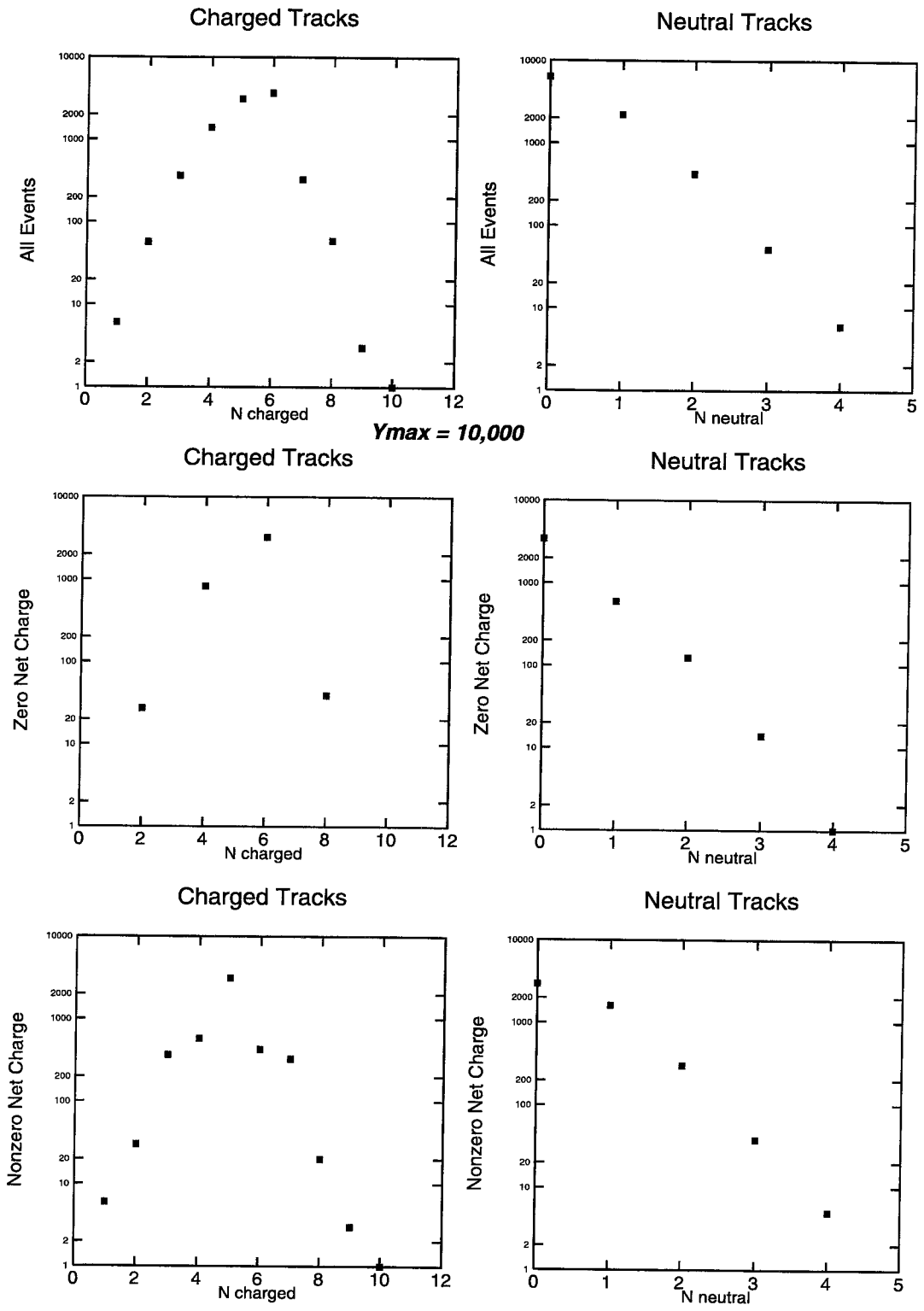

Figure 7.2: Number of charged and neutral tracks in hadronic MC signal. The first row contains all events, the second and third those with and without charge balance, respectively.

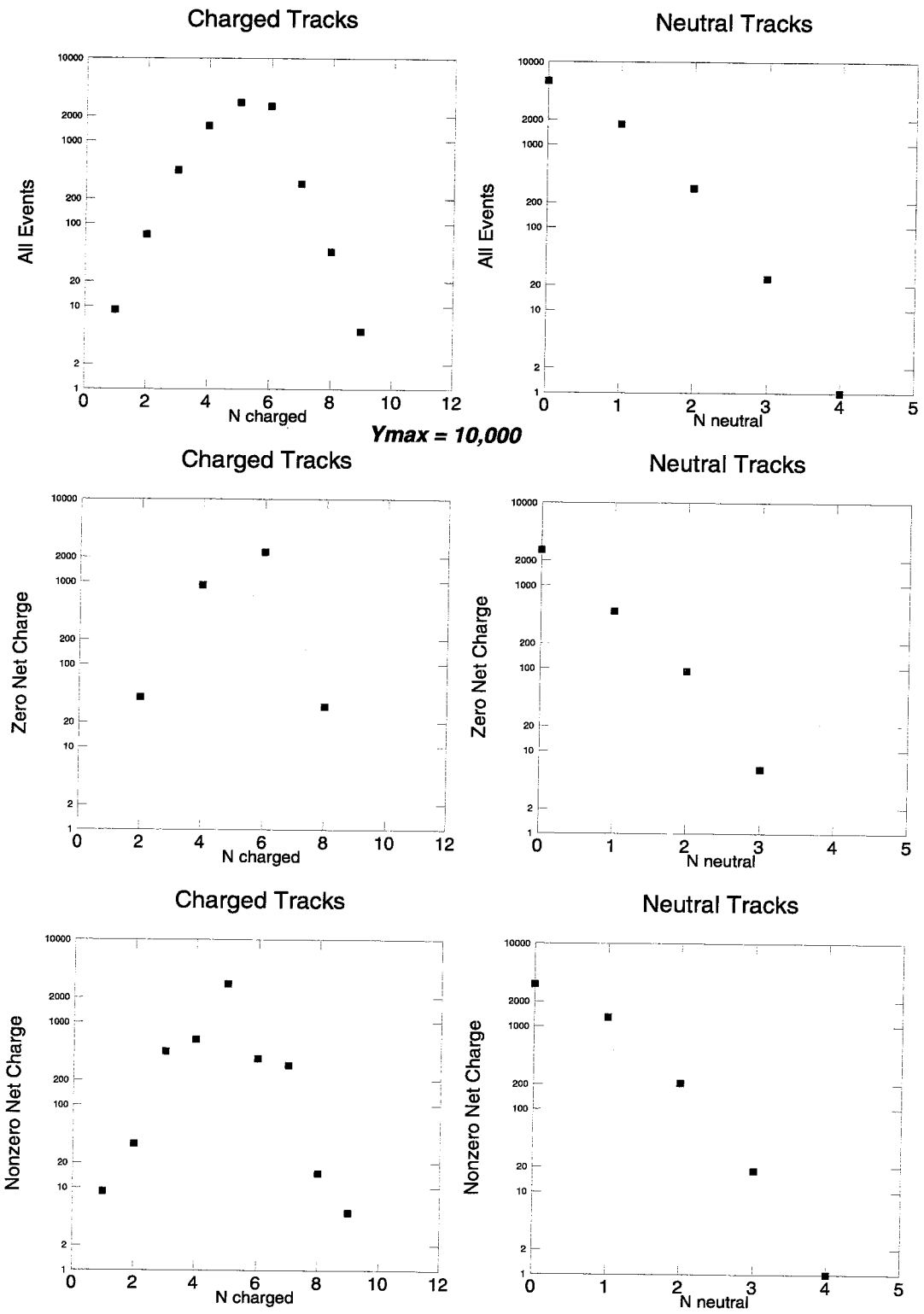

Figure 7.3: Number of charged and neutral tracks in semileptonic MC signal. The first row contains all events, the second and third those with and without charge balance, respectively.

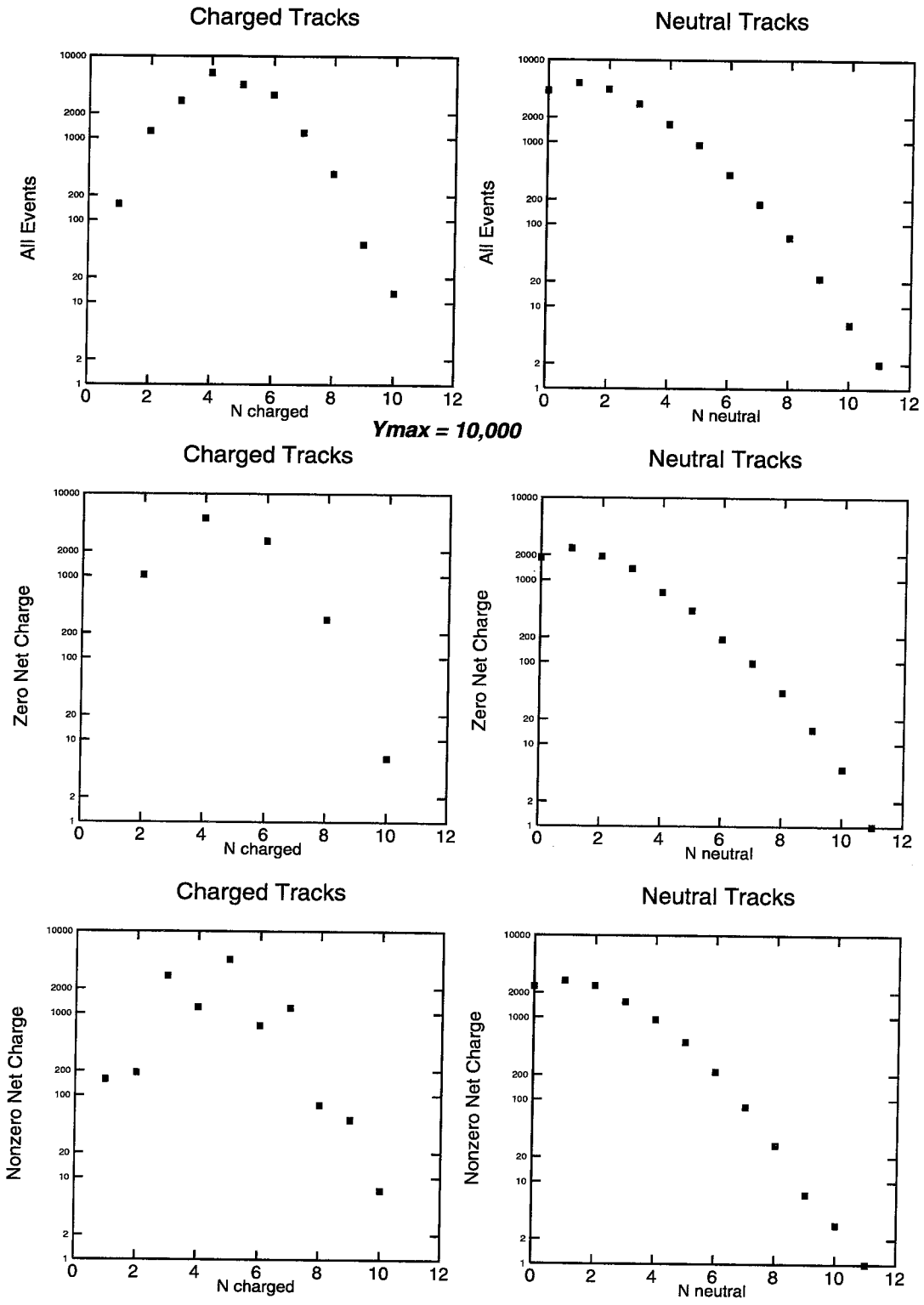

Figure 7.4: Number of charged and neutral tracks in D^* MC background. The first row contains all events, the second and third those with and without charge balance, respectively.

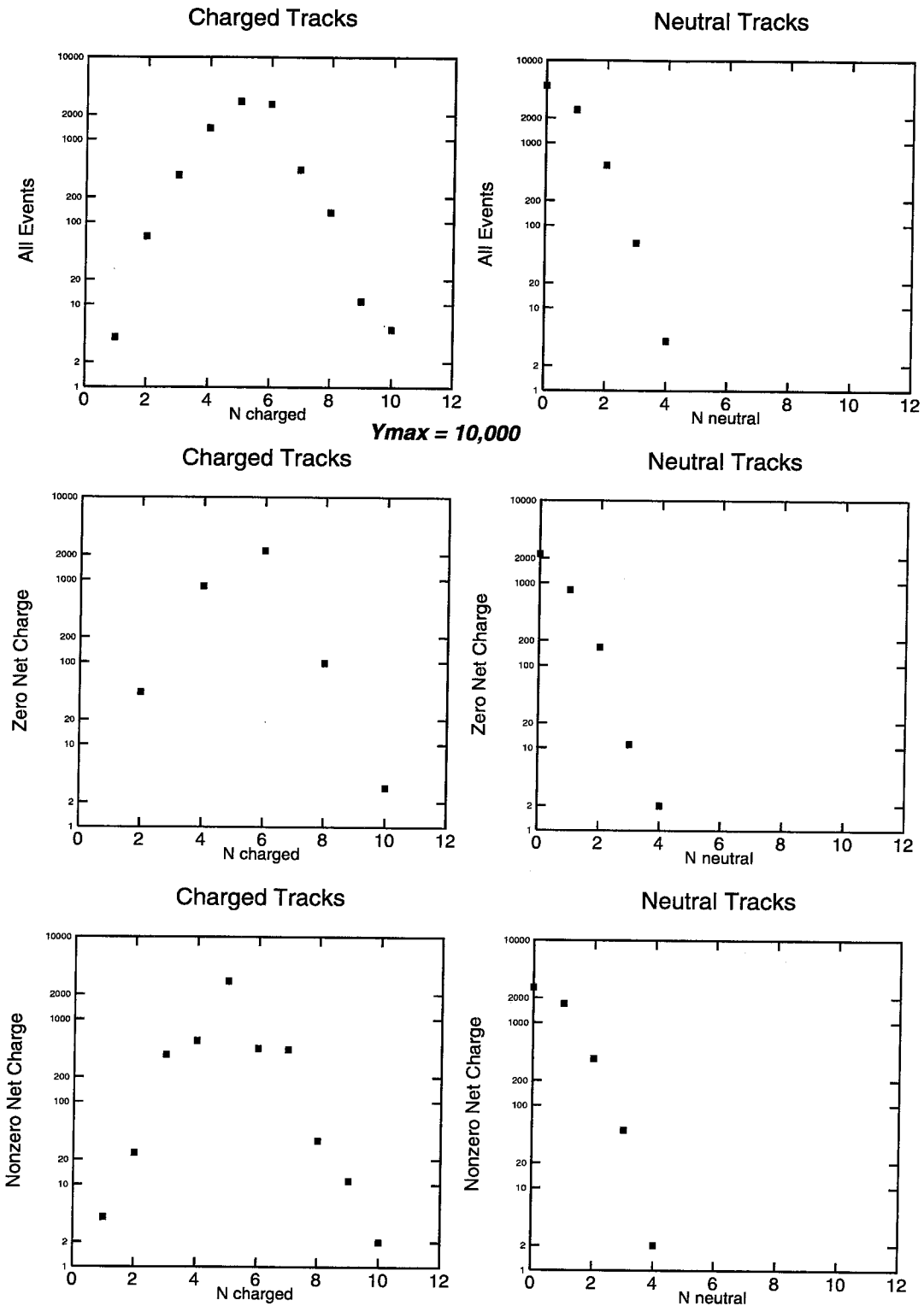

Figure 7.5: Number of charged and neutral tracks in D_s including π^0 MC background. The first row contains all events, the second and third those with and without charge balance, respectively.

7.3 Event Classification

To avoid contamination due to lost particles, it is important to account for all the energy and momentum in the event. We start by looking at the missing momentum, equal and opposite to the sum of the momenta for all six tracks, $\vec{p} = \sum_i^6 \vec{p_i}$. We then use this information to classify the event as hadronic or semileptonic. Since this takes place before particle identification, we must do this using momenta uncorrected for beam-pipe energy loss.

For semileptonic events, this momentum is associated with the missing neutrino. To distinguish it from particles trapped in the beampipe, we require $p_T = \sqrt{p_x^2 + p_y^2} >$ 200 MeV. For hadronic events, this should be zero, so we require $|\vec{p}| < 150$ MeV and the three-constraint kinematic fit $\vec{p} = 0.0$ to have a $\chi^2 < 200$. Plots of $|\vec{p}|$ and p_T for real data and signal MC are shown in Figure 7.6, and for background MC in Figure 7.7.

7.4 Particle Identification (PID)

For each track, we calculate particle identification information using the standard BES package, TrackID[23]. We use it to calculate a χ^2 for each of the hypotheses $e, \mu, \pi,$ and K. Measurements from all the various subsystems listed in Chapter 3 are compared with the theoretical expectations for a given hypothesis at the proper momentum. For each subsystem, the χ^2 is only considered valid if the $\chi^2 < 9.0$ for at least one hypotheses (since there are no other stable particles in this kind of event, and it is possible for a subsystem to return invalid data). If it is valid, the appropriate χ^2 is added to each hypothesis, and the number of degrees of freedom is incremented.

Each subsystem also returns the corresponding likelihood generated from the same function used for the χ^2. The only exception is the muon system, which returns a likelihood based on the hit pattern in the three layers. The likelihoods from all the subsystems are multiplied together to give an overall likelihood for that hypotheses. These likelihoods are then scaled by the sum of likelihoods of all hypotheses for that

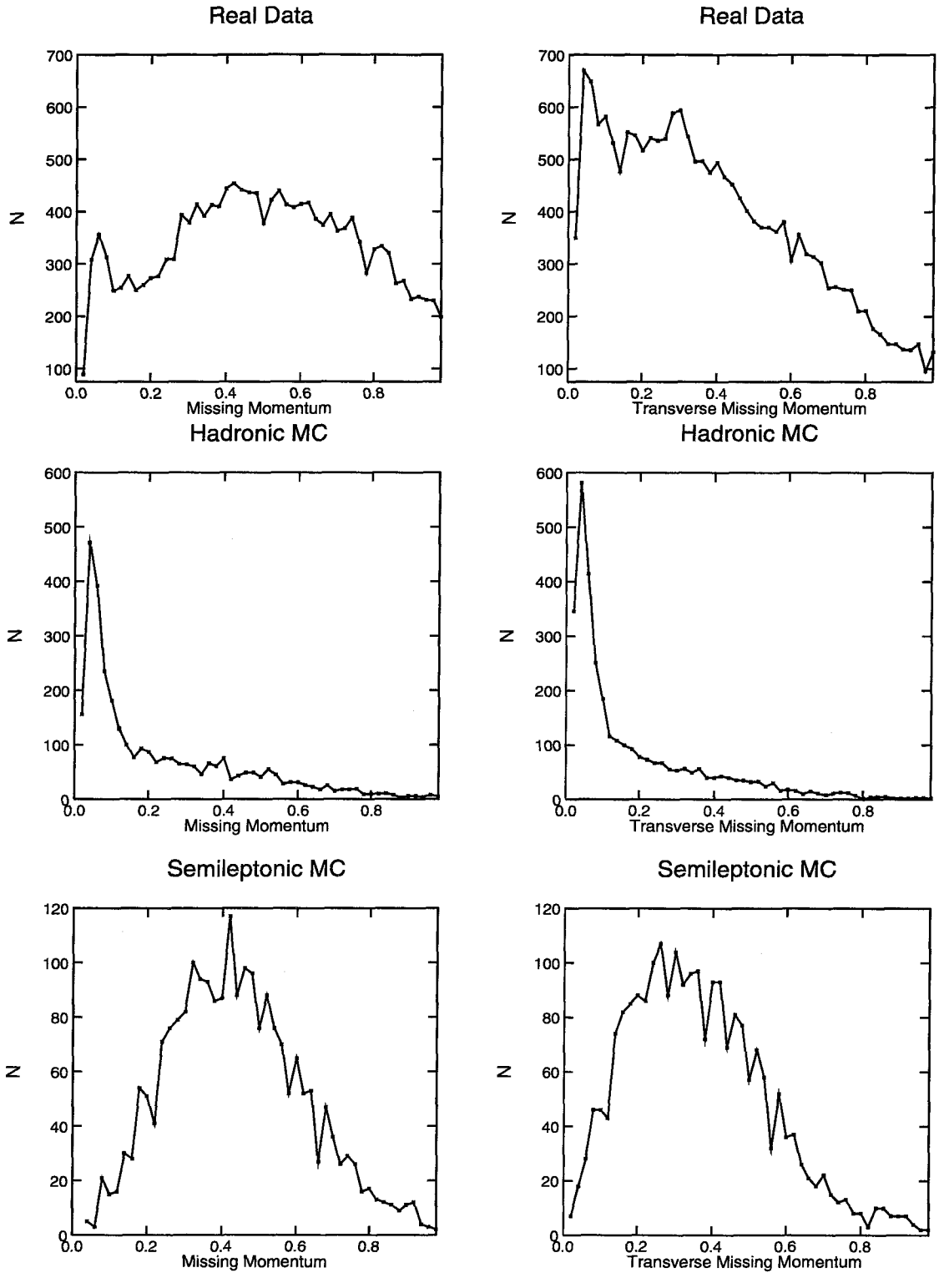

Figure 7.6: Good event momenta for real data and signal MC.

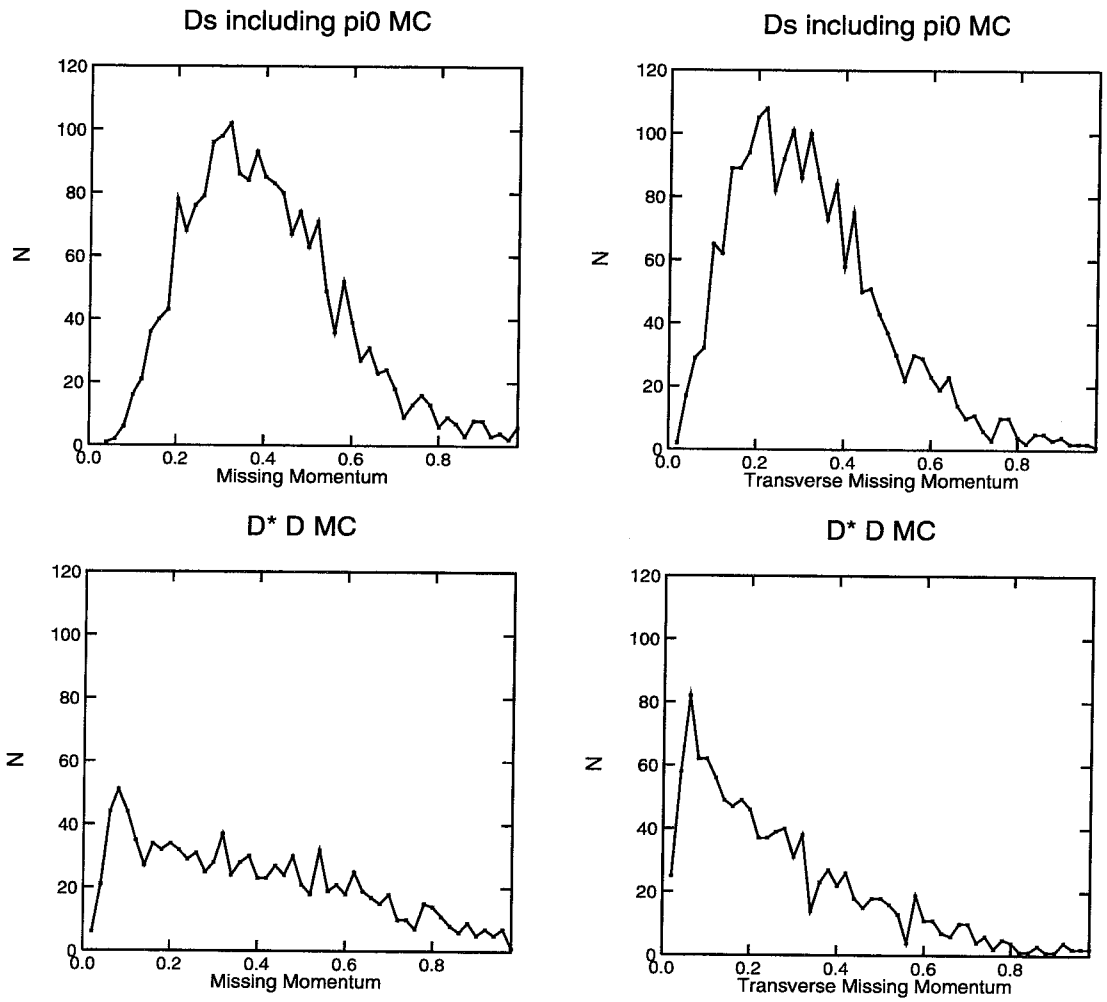

Figure 7.7: Good event momenta for background.

Right-sign	Wrong-sign
Hadronic	
$K^+K^-\pi^+$	$K^+\pi^-K^+$
$K^+\pi^-\pi^+$	$\pi^+K^-\pi^+$
$\pi^+\pi^-\pi^+$	$K^+K^-K^+$
Semileptonic	
$K^+K^-l^+$	$K^+l^-K^+$
$K^+\pi^-l^+$	$K^+l^-\pi^+$
$\pi^+\pi^-l^+$	$\pi^+l^-\pi^+$

Table 7.2: Hadronic and semileptonic particle identification triplets.

track, yielding a normalized weight.

Each D_s is composed of three tracks, two with the same charge and one with the opposite charge. Since we are dominated by spectator decays, the lepton from charm decay will generally have the same sign as the D_s. Any "wrong-sign" leptons are most likely due to background, and hence can be used to estimate the frequency of random coincidences. Similarly, Cabbibo-allowed hadronic spectator decays would always contain a right-sign strange quark; Cabbibo-suppressed modes, having the wrong-sign, would most likely be due to background processes. Table 7.2 shows the various right-sign and wrong-sign hadronic and semileptonic modes.

The χ^2 and likelihood for each individual per-track hypothesis are both combined over all the tracks to produce overall PID values for the triplet.

7.5 Combinatorics

The (nominally) three positive and three negative tracks can be grouped into two triplets, $+-+$ and $-+-$, corresponding to D_s candidates. There are nine such groupings, or hextets, per event. For each one, we evaluate all the different wrong-sign and right-sign hypothesis pairs with the appropriate number of kaons. We then calculate the PID χ^2 for the entire hextet, and calculate the confidence level with the relevant degrees of freedom. If it comes out to less than 1.0×10^{-4}, the combination is discarded.

Note that there are several triplets where a kaon and a pion both have the same

Type	N_K	Right-Sign	Wrong-Sign
Hadronic	4	$K^+K^-\pi^+ \times K^-K^+\pi^-$	$K^+\pi^-K^+ \times K^-\pi^+K^-$
	3	$K^+K^-\pi^+ \times K^-\pi^+\pi^-$	$K^+\pi^-K^+ \times K^-\pi^+\pi^-$
Semileptonic	4	$K^+K^-\pi^+ \times K^-K^+l^-$	$K^+\pi^-K^+ \times K^-l^+K^-$
	3	$K^+\pi^-\pi^+ \times K^-K^+l^-$	$K^+\pi^-\pi^+ \times K^-l^+K^-$

Table 7.3: Particle identification hextets.

charge. Trying all the combinations would significantly increase our combinatoric background. Instead, we construct the relative weight $X_{\pi/K} = L_\pi/L_K$ from the two likelihoods. The track with the larger value is called a pion, and the other is treated as a kaon. Other than this, however, all possible combinations are attempted and evaluated independently. The relevant right-sign and wrong-sign combinations for $D_s^+D_s^-$ systems with the appropriate number of kaons are shown in Table 7.3.

For each triplet, we also calculate the invariant mass ($m^2 = (\sum_{i=1}^3 E_i)^2 - (\sum_{i=1}^3 \vec{p}_i)^2$) and beam-constrained mass ($m^2 = E_{beam}^2 - (\sum_{i=1}^3 \vec{p}_i)^2$).

7.6 Kinematic Fitting

We now apply various kinematic constraints using the TELESIS kinematic fitting package[24]. This returns a χ^2 representing the minimum "pull" needed to make the momenta of the various tracks satisfy the given constraints. The χ^2 from the kinematic fit can be used to form a fit confidence level (FCL). Like any other χ^2 it can be added to the χ^2 from particle identification, forming a joint confidence level (JCL). This gives us a probability measuring how well we have accounted for all the particles in the event.

Having assigned particle ID to each track, we now have a set of four-momenta which should add up to the incoming beam energies, 4.03 GeV, plus a net momentum of zero. This gives a four constraint (4C) fit for hadronic events, corresponding to the four-momenta. For semileptonic events, the missing neutrino is modeled by an extra track with three free parameters, whose mass is fixed to be zero. This reduces the number of constraints by three, giving a 1C fit.

This four-momentum-conservation (FMC) fit simply uses the momentum and par-

Name	Symbol	Constraint	Number of Constraints	
			Hadronic	Semileptonic
Four-Momentum Conservation	FMC	$\sum_{i=1}^{6} E_i = 2E_{beam}$ $\sum_{i=1}^{6} \vec{p}_i = \vec{0}$	4	1
Equal Mass	EM	$m_+ = m_-$	5	2
D_sMass	D_s	$m_+ = m_- = m_{D_s}$	6	3
K^0 mass (swum)	K^0	$m_{\pi\pi} = m_{K^0}$	+1	+1

Table 7.4: Constraints applied via kinematic fits.

ticle ID information to ensure that we have captured all the decay products of the event. We also attempt an equal-mass (EM) fit to establish that the decay came from two paired triplets. The additional constraint is that the mass associated with one triplet must equal that of the other triplet. Put another way, half the energy and momenta of the event should go into each triplet. This helps select pair-produced systems, without creating significant bias in favor of the D_s.

To identify our signal, we also fit with one more constraint: that the mass of both triplets be equal to the D_s mass, defined by the PDG value of 1968.5 MeV. We also calculate the various two-body masses from the fitted tracks, to aid us in searching for resonant decays. We do not impose any sort of constraint or cut on the two-body masses, allowing us to also search for non-resonant decays. However, for triplets which may contain a $K^0_S K$ decay, we also attempt an additional calculation. This is done in parallel with the other triplets, serving as a supplementary check.

The lifetime of the K^0_S is long enough for it to travel a considerable distance from the IP before decaying, perhaps even exiting the beampipe. This would change the beam-pipe energy correction required for the resulting pions. Additionally, they would originate from a different location, which would affect the track fit. We use the KLAMS swimming routine, which is part of TELESIS[24], to find a common origin for the two pions, then swim the postulated K^0_S back to the IP. We then add a constraint to the K^0 mass for those refitted tracks. Note that we do not consider events with four pions, so we never have two K^0_S candidates in the same combination.

The various fits attempted for hadronic and semileptonic events are shown in Table 7.4. Note that all three fits with different constraints, are applied. The fitting

Cut Name	Cut Value
Tracks	$N_{usable} = 6$ and $N_{neutral} = 0$
Hadronic	$\|\sum \vec{p}\| < 150$ MeV and $\chi^2_{\vec{p}=0} < 200$
Semileptonic	$p_T > 200$ MeV
Triplets	$KK\pi, K\pi\pi, KKl\nu$
Hextets	$n_K >= 3$
Particle ID	$CL_{PID} > 1.0 \times 10^{-4}$
Kinematic Fit	$\chi^2_{FMC}, \chi^2_{EM} < 50$

Table 7.5: Hardwired cuts.

routines converge only for $\chi^2 < 50$. All combinations for which the momentum-conservation and equal-mass fits converge are saved; the rest are discarded.

7.7 Summary

Table 7.5 summarizes all the hard-wired cuts which are applied.

Chapter 8 The Double-Tag Sample

The sample resulting from the analysis in Chapter 7 is separated into hadronic and semileptonic datasets. These datasets are further divided into events with balanced and unbalanced net charge. We apply cuts to these to derive a clean sample of doubly-tagged D_s decays. This chapter describes those cuts, the resulting double-tags, and the efficiences and backgrounds associated with them.

8.1 Tag Selection

We start by defining $P(D_s)$, the total probability for being a D_s, as the joint confidence level (JCL) from particle identification and the kinematic fit to the D_s mass. In principle all we need to do is to choose the point at which to cut on $P(D_s)$. We look at its distribution for all events where the fit converged. Figure 8.1 shows the Monte Carlo signal data, while Figure 8.2 shows real data. We choose $P(D_s) = 0.001$ as our cutoff. Note that these plots still include multiple combinations per event, which may account for some of the non-Gaussianness. The resulting MC mass distributions have a width of 1.8 MeV for hadronic events, and 3.5 MeV for semileptonic.

There is one more cut we need to impose. As shown by the Monte Carlos in Figure 8.3, a large number of events with $D_s \rightarrow X + \pi^0$ are still consistent with semileptonic decays. To discriminate against these, we calculate $X_{h/l}$, the relative likelihood for the nominal lepton to be a hadron (π or K) or lepton (μ or e). We require $X_{h/l} < 0.05$, or a factor of twenty greater likelihood. This has the salutary effect of suppressing the π^0 modes by a relative factor of five, as opposed to the original two. The downside of this is that it also reduces our signal by a factor of two. These effects will be calculated below.

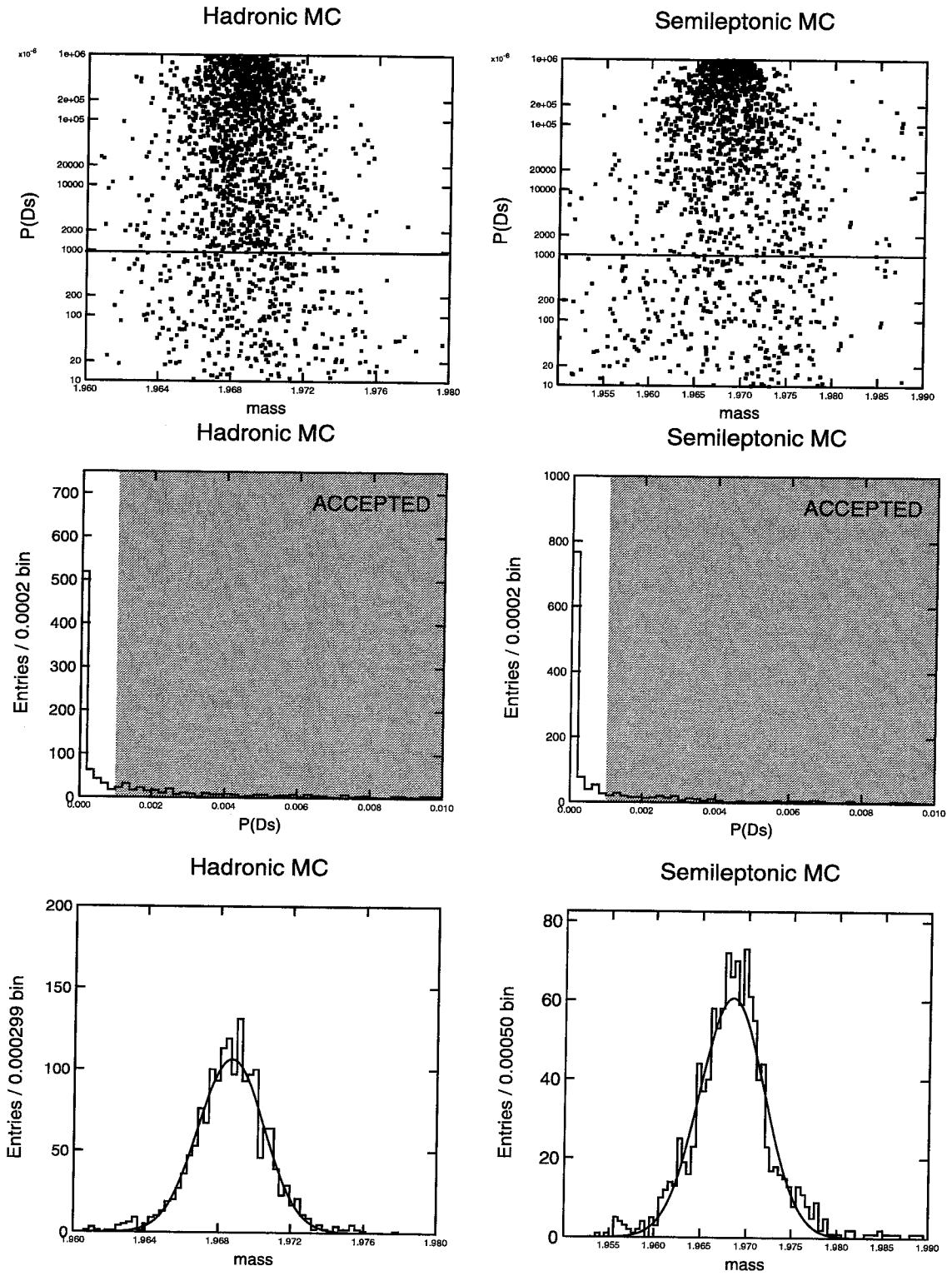

Figure 8.1: $P(D_s)$ for signal MC. The first row is $P(D_s)$ constraint versus the mass (in GeV) from the equal-mass constraint fit. The second row is $P(D_s)$ in the region near zero. The final plot is the mass distribution after the $P(D_s)$ cut of 0.1% was applied

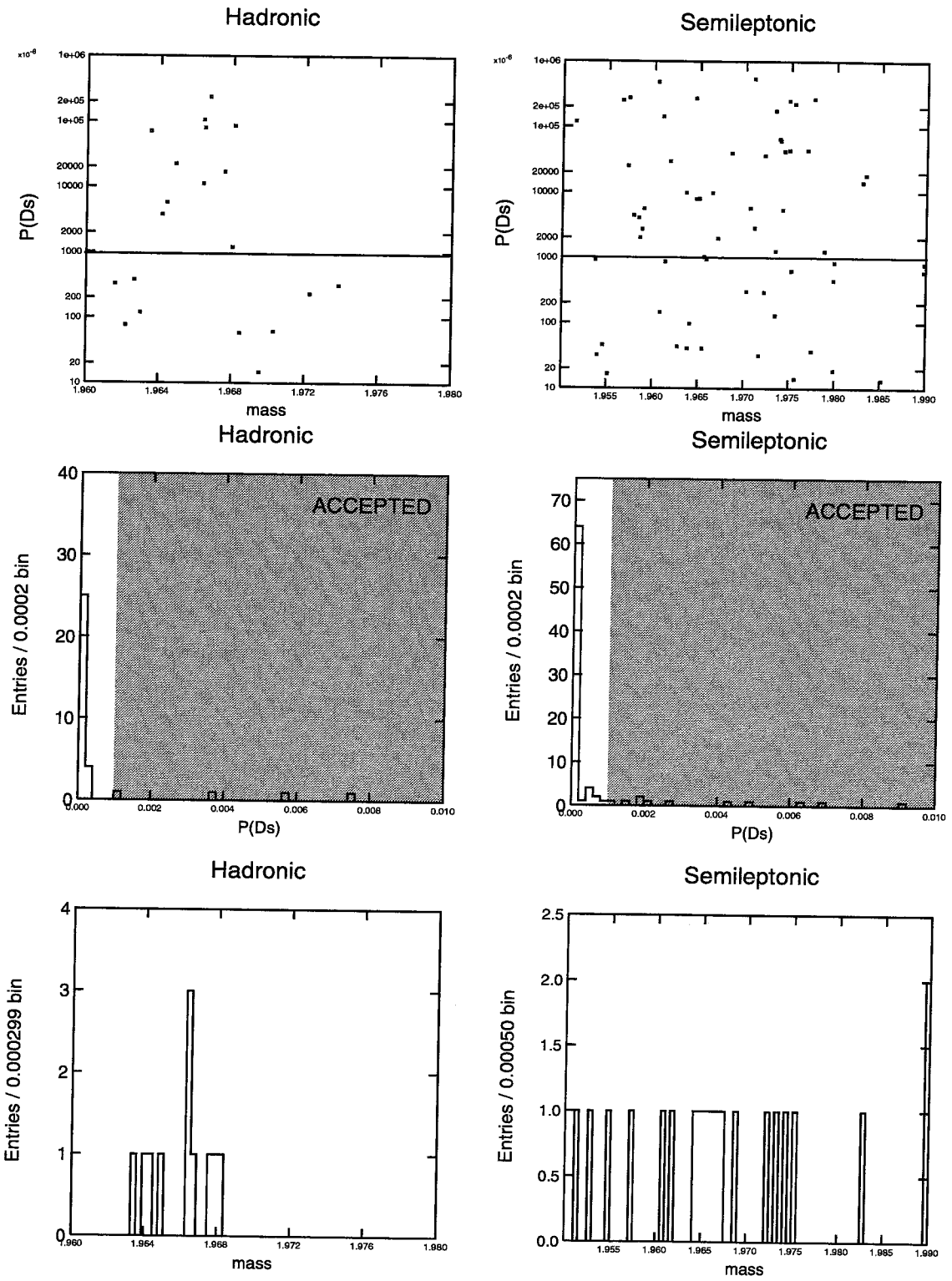

Figure 8.2: $P(D_s)$ for real data. The first row is $P(D_s)$ constraint versus the mass (in GeV) from the equal-mass constraint fit. The second row is $P(D_s)$ in the region near zero. The final plot is the mass distribution after the $P(D_s)$ cut of 0.1% was applied

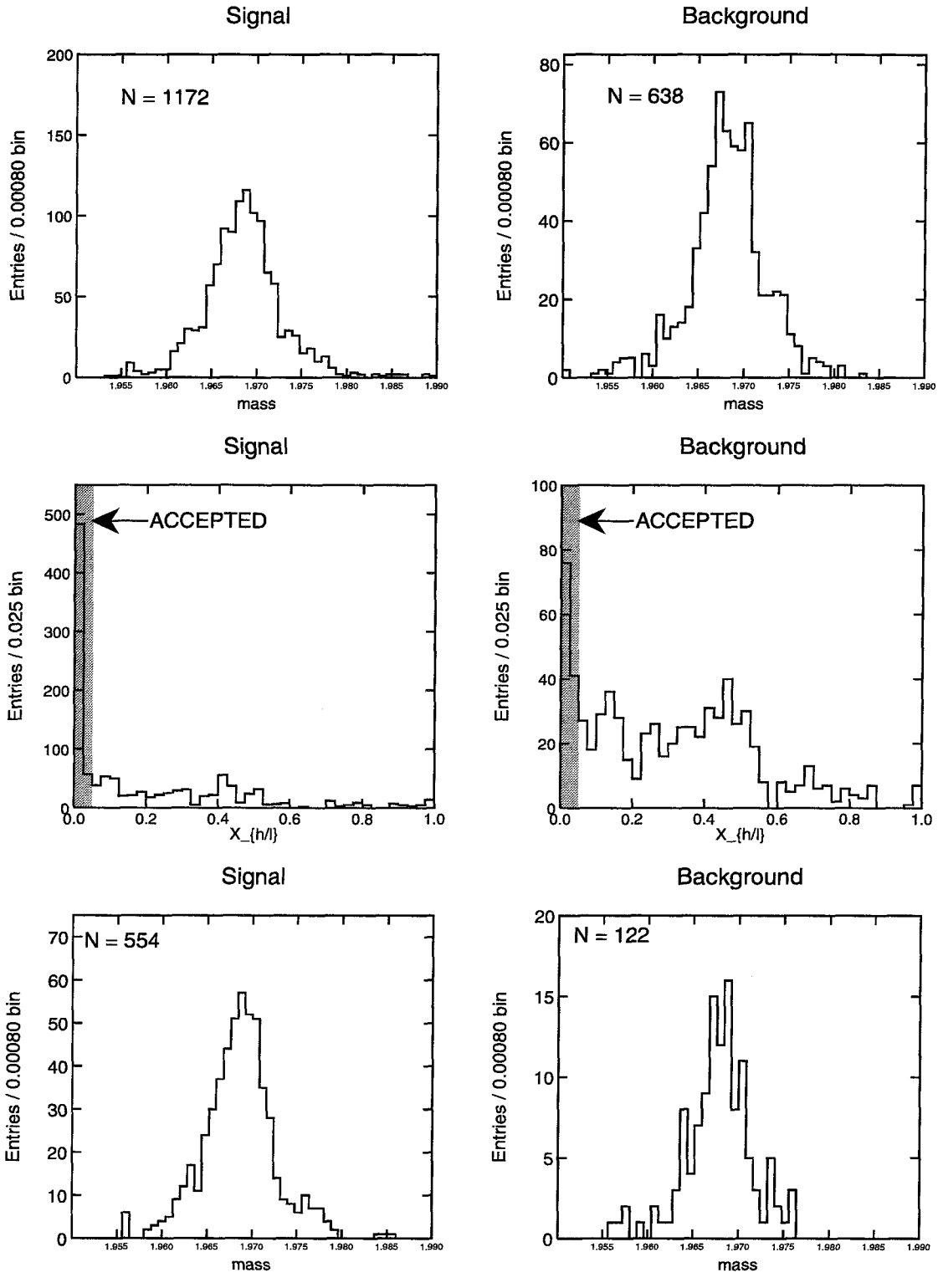

Figure 8.3: Leptonic signal and D_s including π^0 background Monte Carlo.

Name	Mass	Width	Cut
K^0_S	497.672 MeV	8 MeV	±40MeV
K^{0*}	896.1 MeV	23 MeV	±50MeV
ϕ	1019.41 MeV	4 MeV	±20MeV

Table 8.1: Values used for two-body resonances.

8.1.1 Twobody Resonances

Now that we have our signal events, we need to identify from which mode they came. To start with, we need to define our two-body resonances. Figure 8.4 shows the distribution of two-body masses for the $K^0_S, \overline{K}^{*0}$, and ϕ. The data is drawn from signal MC events which pass the preceding cuts. We try all possible combinations of two-body masses which have the correct number of kaons, so there is a fair amount of combinatoric background.

Table 8.1 shows the nominal mass, the fitted width, and the chosen range for identifying the three resonances. In addition to the mass cut, any combination which survives swimming and being constrained to the K^0 mass is also tagged as a K^0_S. The most troublesome mode is the $\overline{K}^{*0}$, since it has a large combinatoric and non-resonant background.

We use this information to calculate a two-body weight W. For each pair, we calculate $W = \frac{1}{\sqrt{2\pi}\sigma} \exp(\frac{-(m-m_0)^2}{2\sigma^2})$. For the two charge-neutral pairs in each triplet, we pick the one with the highest weight. The weight for the entire combination is the sum of the weights for the two triplets. While the use of a Gaussian weight for the K^* is non-physical, it does have the benefit of reducing the influence from the tails, where we would be swamped by non-resonant background.

8.1.2 Combinatoric Reduction

Table 8.2 lists the events and combinations which survive these cuts, with their two-body weight. A K^0_{Swum} indicates that it was tagged by including the K^0_S mass constraint after swimming; the two-body mass shown is the swum mass. No events with non-zero net charge, or identified as semileptonic decays, survived our earlier cuts.

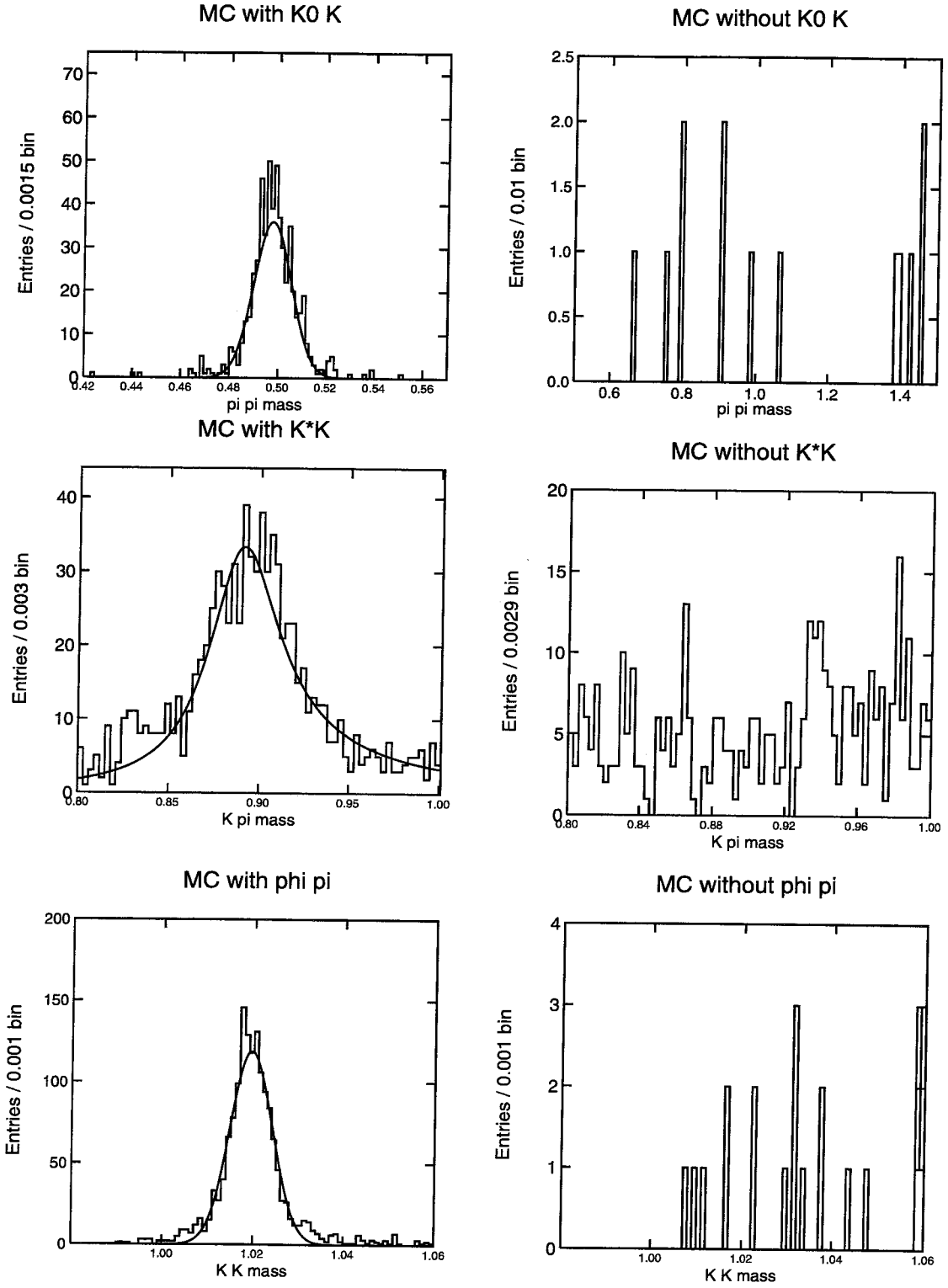

Figure 8.4: Twobody resonance Monte Carlo plots. The left column is from D_s Monte Carlo which contain the resonance of interest, whereas the right is from those which do not.

Run	Event	Mass	$P(D_s)$	Tag	m_{2body}	Recoil	m_{2body}	Weight	N_K
3750	4208	1.9800	0.0076	$(K^-\pi^+)\pi^+$	1.033	$K^-(K^+\pi^-)$	0.702	3.1e-07	-3
3750	4208	1.9664	0.1051	$K^+(K^-\pi^+)$	0.956	$(K^+\pi^-)\pi^-$	0.707	0.58	-3
3750	4208	1.9635	0.0703	$K^+(K^-\pi^+)$	0.953	$K^0_S K^-$	0.472	1.11	3
3750	4208	1.9664	0.0112	$K^+(K^-\pi^+)$	0.956	$K^0_{Swum} K^-$	0.477	2.6	3
4838	11178	1.9681	0.0861	$\overline{K}^{*0} K^+$	0.852	$\phi\pi^-$	1.011	15.39	4
5113	19395	1.9676	0.0169	$\overline{K}^{*0} K^+$	0.877	$K^-(\pi^+\pi^-)$	0.292	12.26	-3
5113	19395	1.9680	0.0012	$K^+(K^-\pi^+)$	1.342	$K^-(\pi^+\pi^-)$	0.292	0	3
6422	27143	1.9665	0.0792	$\overline{K}^{*0} K^+$	0.874	$K^{*0} K^-$	0.918	21.96	4
6462	31342	1.9642	0.0038	$K^0_S K^+$	0.501	$K^-(K^+\pi^-)$	1.420	44.76	3
6462	31342	1.9644	0.0058	$K^0_{Swum} K^+$	0.546	$K^-(K^+\pi^-)$	1.420	7e-07	3
6462	31342	1.9649	0.0225	$K^+(\pi^-\pi^+)$	0.901	$K^-(K^+\pi^-)$	1.457	0	3
7108	19638	1.9668	0.2367	$\overline{K}^{*0} K^+$	0.904	$K^-(K^+\pi^-)$	0.828	16.61	4

Table 8.2: Mode breakdown of final combinations. m_{2body} is the mass for the resonance, or the parenthesized pair in the triplet with the highest two-body weight. N_K is the number of kaons in the event, and is set negative if there is at least one wrong-sign triplet present.

Some of semileptonics survived the $P(D_s)$ cut, but failed the hadron/lepton cut.

8.1.3 Signal Events

In order to identify which channel a particular event came from, we first need to pick a particular combination to represent it. To improve our efficiency, we want to pick the combination that most resembles a D_s decay. We use the information in Table 5.2 to rank combinations as to which is most likely to have come from a D_s. First, we always prefer right-sign (Cabbibo-allowed) combinations over wrong-sign ones. Second, we select triplets with two kaons instead of one, in those rare cases where both hypotheses are consistent. We implement both of these by selecting those combinations with the maximum value of N_K for that event. Since there are in general still multiple combinations remaining, we choose the one with the highest two-body weight. This should be effective in conserving signal, even if the resonance widths from the Monte Carlo are not strictly accurate. The decays are then labeled as either resonant or non-resonant, according to Table 8.1.

The invariant and beam-constrained masses for these combinations are tabulated

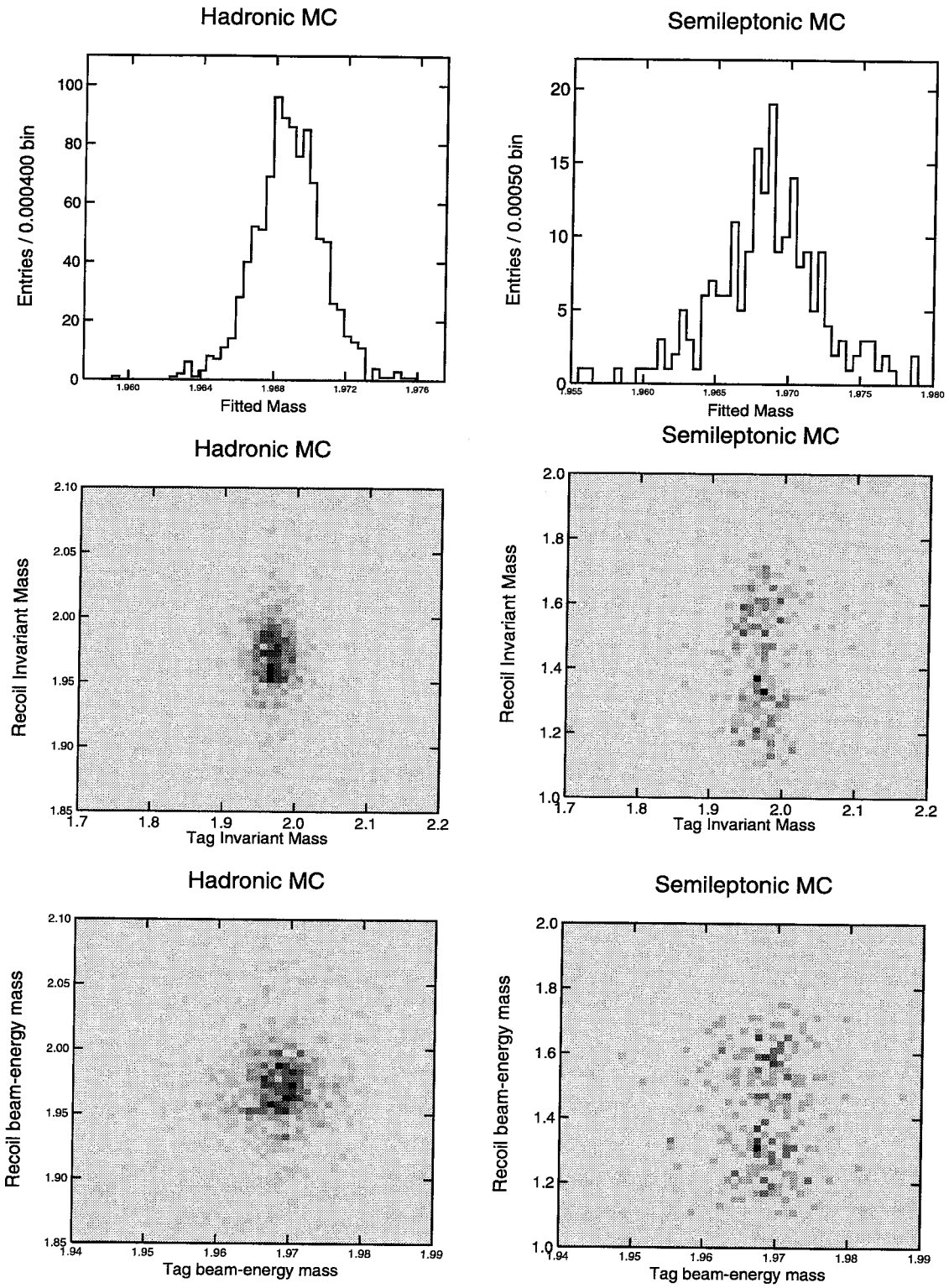

Figure 8.5: Invariant and beam-energy constrained masses for signal Monte Carlo.

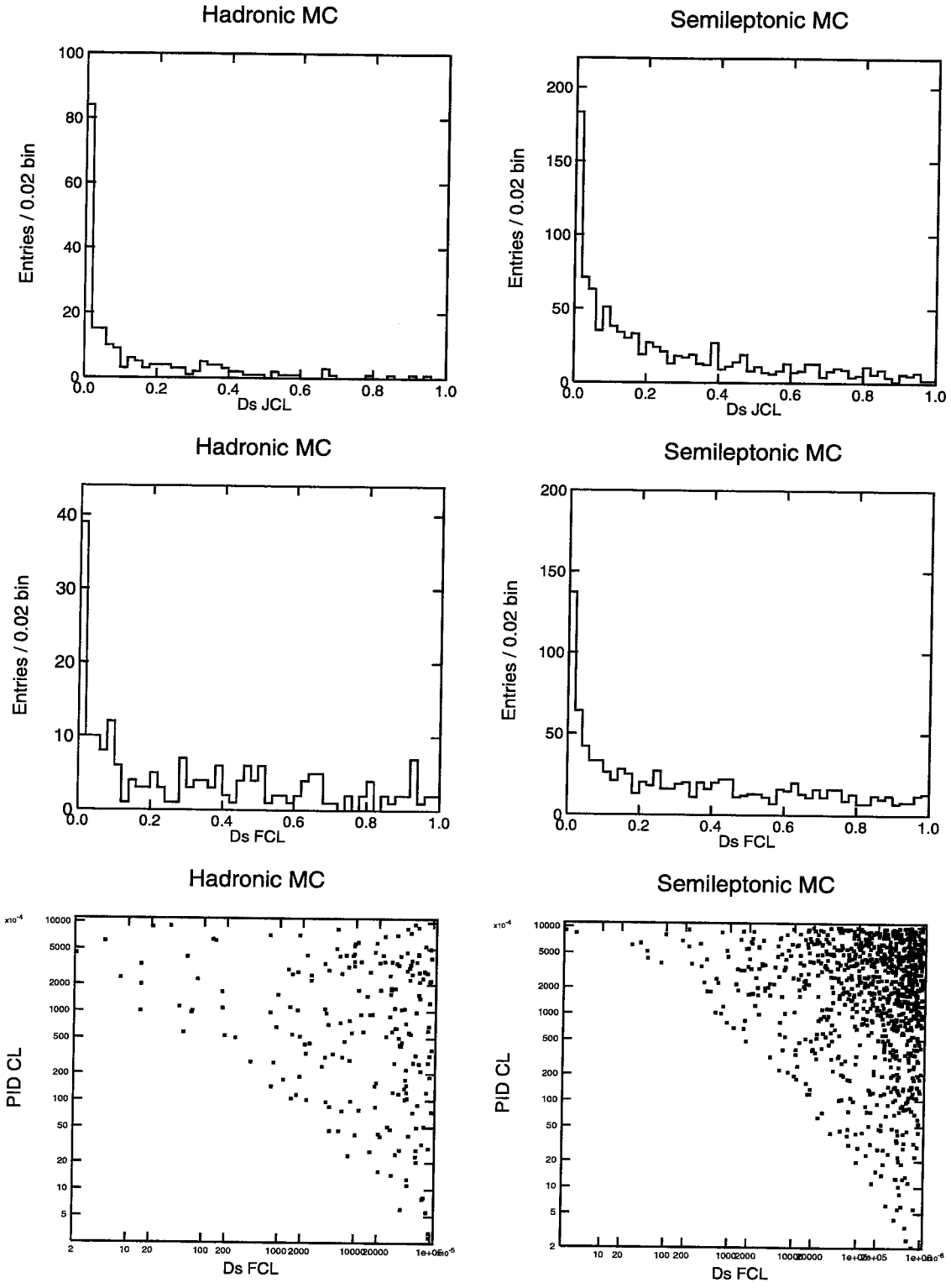

Figure 8.6: Confidence levels for Monte Carlo signal data. FCL is the confidence level just from the D_s mass fit, whereas JCL also includes the χ^2 from particle identification.

Run	Event	Mass	Mode	Tag Mass		Recoil Mass	
				Invariant	BC	Invariant	BC
3750	4208	1.9664	$K^+K^-\pi^+ \times K^0_{Swum}K^-$	2.1232	1.9723	1.9378	1.9822
4838	11178	1.9681	$\overline{K}^{*0}K^+ \times \phi\pi^-$	2.0131	1.9551	1.9518	1.9696
5113	19395	1.9680	$K^+K^-\pi^+ \times K^-\pi^+\pi^-$	2.0754	1.9670	1.9565	1.9631
6422	27143	1.9665	$\overline{K}^{*0}K^+ \times K^{*0}K^-$	1.9889	1.9648	1.9516	1.9624
6462	31342	1.9642	$K^0_SK^+ \times K^-K^+\pi^-$	2.1083	1.9452	1.9500	1.9655
7108	19638	1.9668	$\overline{K}^{*0}K^+ \times K^-K^+\pi^-$	1.9780	1.9663	1.9577	1.9667

Table 8.3: Masses of signal events. We have one mass from the equal-mass fit, and one from each triplet for the invariant and beam-constraint masses.

Run	Event	PID CL	Beam Constraint		Equal Mass		D_s Mass	
			Fit CL	Joint CL	Fit CL	Joint CL	Fit CL	Joint CL
3750	4208	0.2838	0.0008	0.0056	0.0016	0.008	0.0031	0.0112
4838	11178	0.9368	0.0004	0.0509	0.0008	0.0651	0.0018	0.0861
5113	19395	0.1173	0.0384	0.0317	0.0002	0.0008	0.0005	0.0012
6422	27143	0.0728	0.9465	0.1765	0.432	0.0969	0.3195	0.0792
6462	31342	0.4644	0.0013	0.0216	0.0007	0.0125	0.0002	0.0038
7108	19638	0.2689	0.4446	0.3059	0.4346	0.3039	0.2884	0.2367

Table 8.4: Confidence levels of signal events.

in Table 8.3, with the confidence levels shown in Table 8.4. Plots of these quantities for Monte Carlo signal events are shown in Figures 8.5 and 8.6. Note that event 5113/19395, with a non-resonant $K^-\pi^+\pi^-$, has $m_{\pi\pi} = 2m_\pi$. This is consistent with pions really being misidentified electrons, pair-produced by a photon. Like all other non-resonant $\pi\pi$ events, it is considered background, and will be ignored for the remainder of this analysis.

Name	Cut
Consistency with D_s	$JCL_{D_s} > 0.001$
Hadron/Lepton	$X_{h/l} < 0.05$
Cabbibo-Allowed	$\max_{event}(N_K)$
Maximum Two-body Weight	$\max_{event}(W_+ + W_-)$
No Non-Resonant $K\pi\pi$	$m_{\pi\pi} = m_{K^0}$

Table 8.5: Summary of interactive cuts applied. $\max_{event}(X)$ indicates that X for a combination must equal the highest value of X possessed by any combination in that event. $W_\pm$ is the larger of the two two-body weights in the positive (negative) D_s candidate.

The interactive cuts used in this chapter are summarized in Table 8.5.

8.2 Backgrounds

Since we cut on confidence level rather than mass, we do not have the usual sidebands we could use for background study. What we can do, however, is drop the D_s mass requirement from our kinematic fit, and just impose the equal-mass constraint. This gives us a traditional mass plot, where we can look for events near the D_s mass. We define our signal region for these purposes as ± 5 MeV around the nominal D_s mass, roughly 3σ on the MC plot in Figure 8.1. For our background estimation, we will focus on hadronic modes, since that is where we found events. Using a background of zero for modes with zero events gives a conservative error estimate.

We then cut on the analogous joint confidence level $P(m_+ = m_-) > 0.001$. The resulting plots for data are shown in Figure 8.7. Our signal events form the peak at the D_s mass. We also find considerable background just below that. All combinations with a mass greater than 1.9 GeV are shown in Table 8.6, excluding the signal events listed in Table 8.2.

Figure 8.8 shows the background broken down into three-kaon and four-kaon channels. We find a large three-kaon background, with a peak just below the D_s mass. We also find two four-kaon background combinations. The backgrounds for these channels are discussed in the following sections.

8.2.1 Three-Kaon Background

We find several events with two non-resonant pions about five MeV away from the D_s mass, one of which contains a $\overline{K}^{*0}$. Tables 8.7 shows $m_{\pi\pi}$ for the two right-sign events with $P(D_s)$ just above 10^{-4}. We do not know their source, but we will treat them as a potential background. We make the conservative assumption that they are located inside the D_s mass region. We further assume that their mass is distributed according to phase space from $K\pi\pi$ decays of the D_s. We can then find the mass distribution

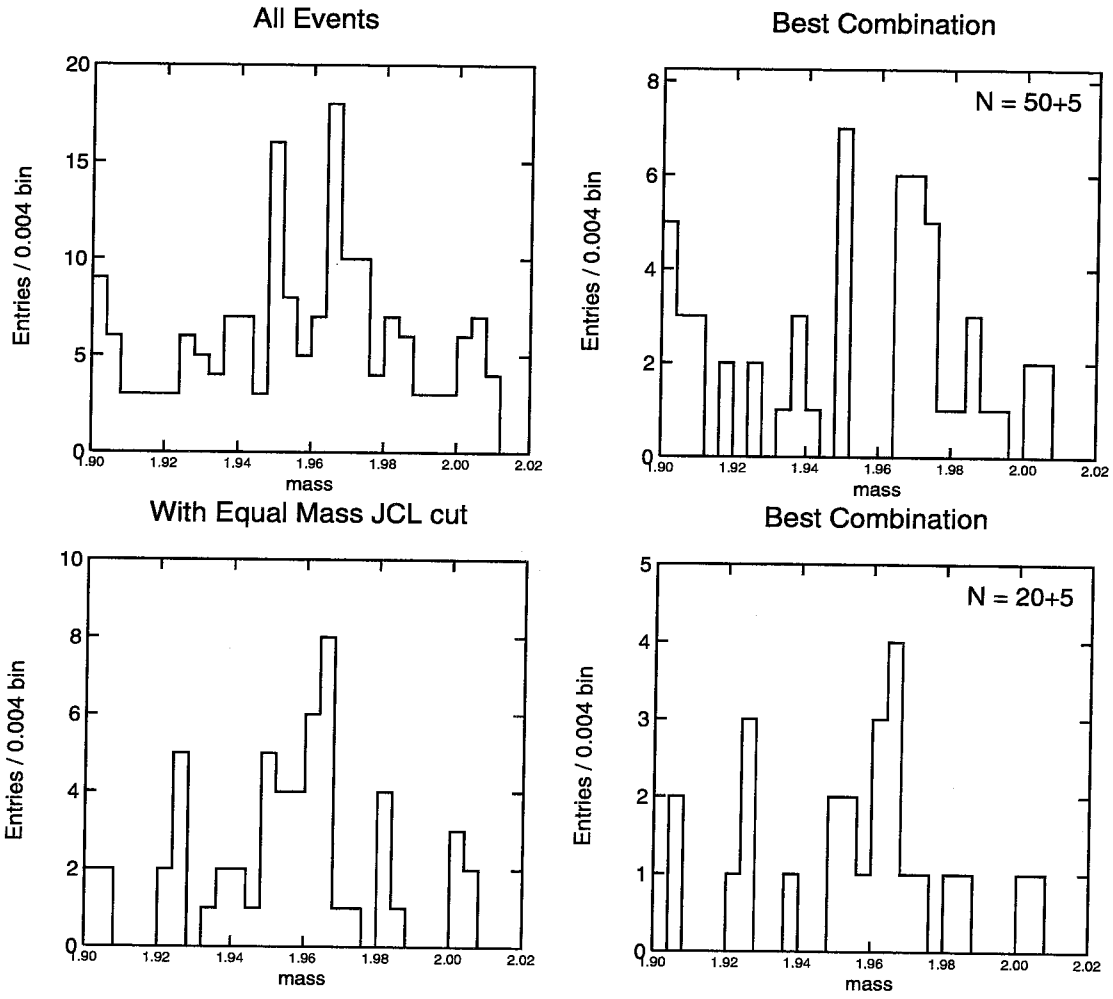

Figure 8.7: Mass Plot from equal-mass fit of real data. The first row is all events, the second requires $P(m_+ = m_-) > 0.001$. The first column contains all combinations, and hence double-counts. The second column shows only that combination with the highest two-body weight.

.

Run	Event	Mass	$P(D_s)$	Tag	m_{2body}	Recoil	m_{2body}	Weight	N_K
3211	7468	1.9251	0	$K^+(K^-\pi^+)$	1.109	$K^-(\pi^+\pi^-)$	0.562	5e-13	3
3232	3904	1.9232	0	$(K^-\pi^+)\pi^+$	0.983	$K^-(K^+\pi^-)$	0.982	0.03	-3
3273	31625	1.9263	0	$K^+(\pi^-\pi^+)$	0.671	$K^{*0}K^-$	0.935	4.21	3
3927	27132	1.9574	9.0e-05	$K^+(K^-\pi^+)$	1.235	$K^-(K^+\pi^-)$	1.048	6.3e-09	4
4523	37368	1.9053	0	$K^+(K^-\pi^+)$	0.982	$K^-(\pi^+\pi^-)$	0.923	0.02	3
5082	28884	2.0054	0	$K^+(K^-\pi^+)$	0.845	$K^-(\pi^+\pi^-)$	0.587	1.45	3
5627	17011	2.0008	0	$K^+(\pi^-\pi^+)$	0.823	$K^{*0}K^-$	0.885	15.28	3
5632	14293	1.9395	0	$K^+(K^-\pi^+)$	0.768	$(K^+\pi^-)\pi^-$	0.813	0.03	3
6091	18333	1.9246	0	$\overline{K}^{*0}\pi^+$	0.852	$\phi\pi^-$	1.017	90.43	-3
6294	27137	1.9535	4.3e-09	$(K^-\pi^+)\pi^+$	1.115	$K^-(K^+\pi^-)$	1.131	4.4e-19	-3
6294	27137	1.9546	4.2e-08	$K^+(\pi^-\pi^+)$	0.933	$K^-(K^+\pi^-)$	1.132	2e-22	-3
6294	27137	1.9069	0	$K^+(\pi^-\pi^+)$	0.861	$K^-(K^+\pi^-)$	1.097	5.2e-16	-3
6325	7677	1.9616	0.0003	$(K^-\pi^+)\pi^+$	1.002	$K^-(K^+\pi^-)$	0.742	0	-3
6679	4387	1.9739	0.0003	$K^+(K^-\pi^+)$	1.112	$(K^+\pi^-)\pi^-$	1.222	1.4e-18	3
6909	36267	1.9812	3.7e-11	$K^+(\pi^-\pi^+)$	0.643	$K^-(K^+\pi^-)$	0.972	0.07	3
6945	18950	1.9498	9.6e-14	$K^+(K^-\pi^+)$	1.380	$K^-(\pi^+\pi^-)$	0.914	0	3
6945	22767	1.9627	0.0004	$\overline{K}^{*0}K^+$	0.896	$K^-(\pi^+\pi^-)$	0.705	17.34	3
7142	9389	1.9509	9.2e-19	$\overline{K}^{*0}K^+$	0.910	$\phi\pi^-$	1.024	66.25	4
7355	23066	1.9868	0	$(K^-\pi^+)\pi^+$	1.491	$\phi\pi^-$	1.033	0.31	-3

Table 8.6: Background combinations of real data with $P(m^+ = m^-) > 0.001$ cut.

Run	Event	Mass	$m_{\pi\pi}$	Recoil
6679	4387	1.9739	1.269	$K^+K^-\pi^+$
6945	22767	1.9627	0.705	$\overline{K}^{*0}K^+$

Table 8.7: Non-resonant $K\pi\pi$ background events.

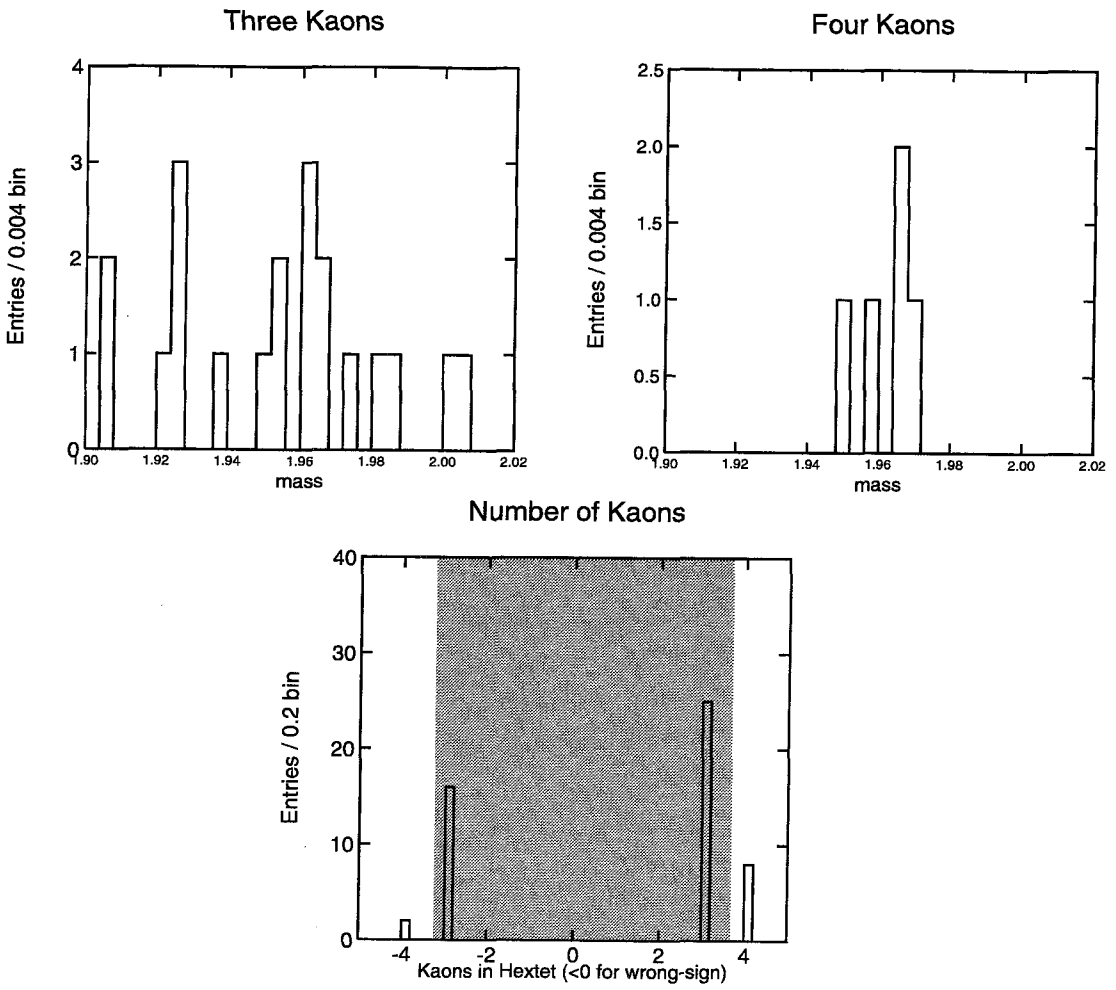

Figure 8.8: Background in three- and four-kaon channels, from real data.

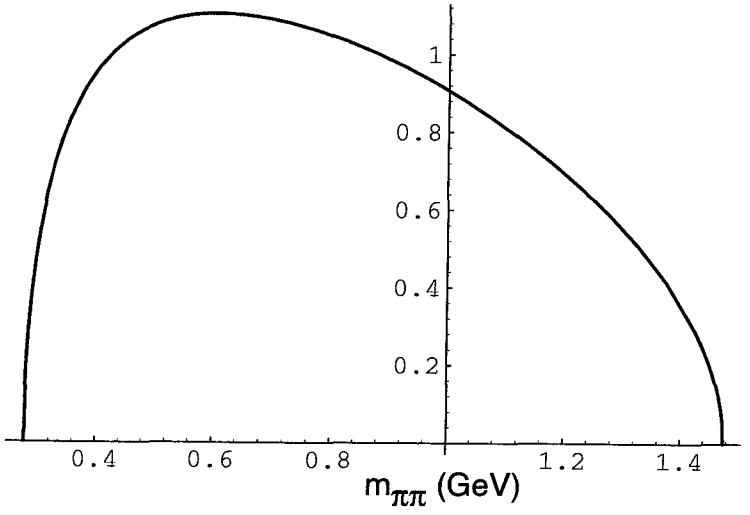

Figure 8.9: $m_{\pi\pi}$ phase space for nonresonant $D_s \to K\pi\pi$ decays.

Run	Event	Mass	Tag	Recoil
3927	27132	1.9574	$K^+K^-\pi^+$	$K^+K^-\pi^+$
7142	9389	1.9509	$\overline{K}^{*0}K^+$	$\phi\pi^-$

Table 8.8: Background events with four kaons.

by projecting the Dalitz plot[25], giving the distribution shown in Figure 8.9.

$$P(m_{\pi\pi}) \propto \frac{\sqrt{\left(m_{\pi\pi}^2 - (2m_\pi)^2\right)\left((m_{D_s} - m_K)^2 - m_{\pi\pi}^2\right)\left((m_{D_s} + m_K)^2 - m_{\pi\pi}^2\right)}}{m_{\pi\pi}} \quad (8.1)$$

Integrating this $\pm$40MeV around the K_S^0 mass gives a probability of 8.6%. Thus, each background non-resonant $\pi\pi$ event implies a background of 0.086 in the equivalent K_S^0 channel. Put another way, the presence of a background event implies an 8.6% probability that the same mechanism produced something resembling a K_S^0.

8.2.2 Four-Kaon Background

The background events with four kaons are shown in Table 8.8. The important parameter is not their two-body mass, but their fitted mass: how many of them would appear inside the D_s signal region? We answer this question by asserting that these background events are due to D^* decay, and hence would have the same distribution.

The distributions for D^* Monte Carlo are shown in Figure 8.10. As we saw in Table 7.1, we are only looking at 4% of the D^0 and 1% of the $D^\pm$ decay width. However, these are the modes which have the right particle multiplicities to contribute to our background. This would then represent a production of 80K neutral and 100K charged D^*D events, comparable to what we would expect from the coupled-channel model cross-sections in Table 4.2 (73K and 79K).

We see that the distribution is very similar to that for the data outside the signal region. In particular, it peaks at 1.95 GeV, where our four-kaon background is located. We also note that the $P(m_+ = m_-)$ cut removes any combinations inside the D_s signal region. If we fit to a flat background plus a Gaussian, we obtain an estimate of 1 ± 0.5

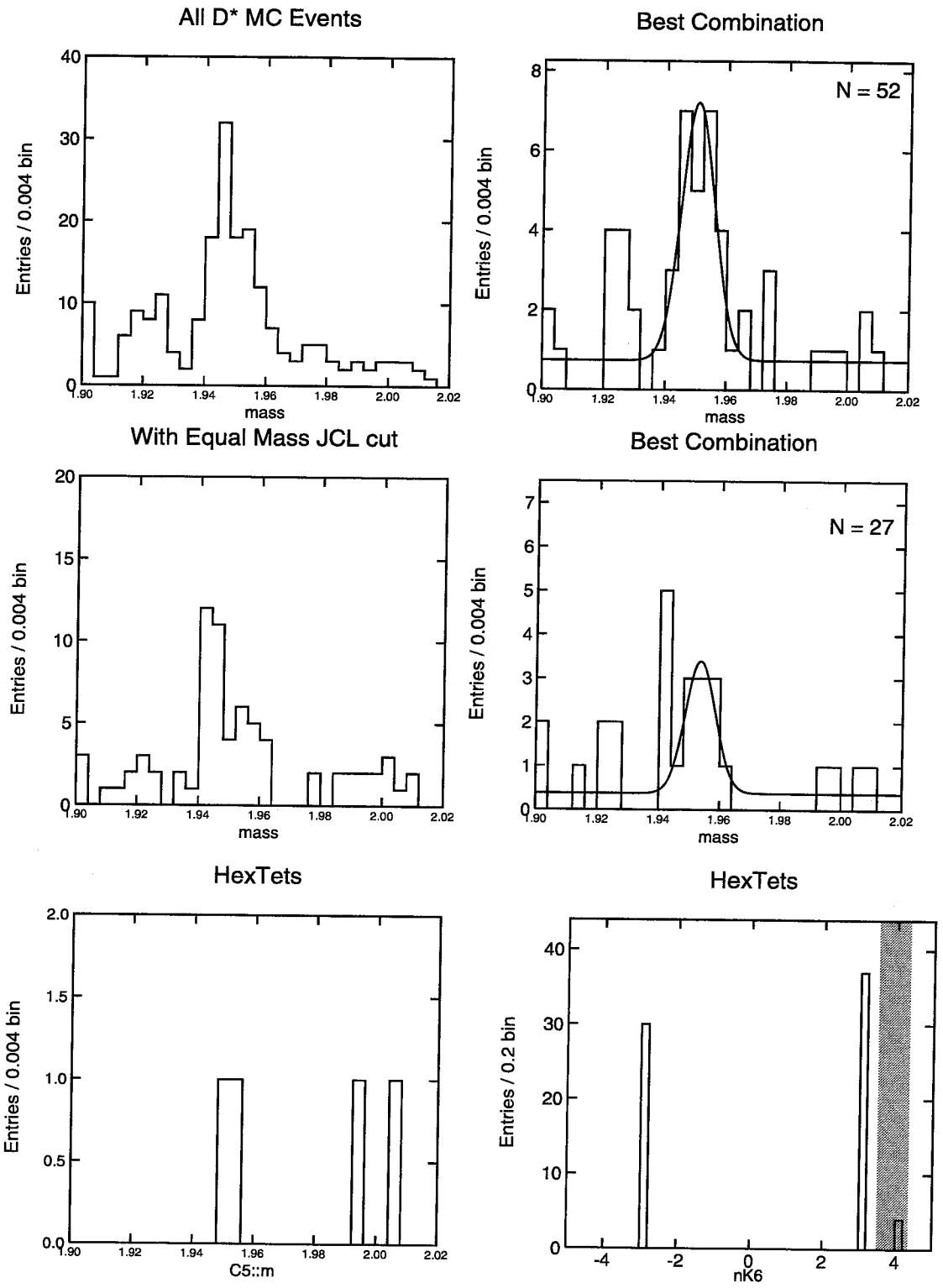

Figure 8.10: Mass Plot from equal-mass fit of D^* Monte Carlo. The first column contains all combinations, and hence double-counts. The second column showns only that combination with the highest two-body weight. The first row is all events, the second requires $P(m_+ = m_-) > 0.001$. The final row shows those events with four kaons that pass the $P(m_+ = m_-)$ cut.

Mode	Number	Background
$\phi\pi \times K^{0*}K$	1	0.075
$KK\pi \times K^0_S K$	2	0.075
$K^*K \times K^0_S K$	0	0.086
$KK\pi \times KK\pi$	0	0.086
$KK\pi \times K^{0*}K$	1	
$K^{0*}K \times K^{0*}K$	1	

Table 8.9: Measured signal and background events.

D^* events inside the 10 MeV signal region. Given that only four out of the 27 events had four kaons, this would imply a D^* background of 0.15 four-kaon events .

To first order, we can assume that the background in our data would be similar, since we have comparable numbers of total events and four-kaon events. Naively dividing this number of background events among the two channels we observed gives 0.075 background events per channel.

8.2.3 Summary

Based on the sidebands and Monte Carlo studies, we estimate 0.32 events of background, divided among two three-kaon and two four-kaon channels. This are summarized in Table 8.9, along with the signal modes measured. The background will form part of our systematic error. Given that our background is less than 10% of our signal, it should have a small effect.

8.3 Efficiencies

Having determined our backgrounds, we now need to estimate our efficiencies. We do this by examining the D_s Monte Carlo on a mode-by-mode basis. The number of events which survive our cuts are shown in Table 8.10 for hadronic decays and Table 8.11 for semileptonics. Note that we combine decays and their charge conjugates, giving a factor of two which will be accounted for later.

We use this information to obtain our efficiencies. To first order, we can simply count the number of events in each mode that is correctly identified, and divide

From \ To	K*K K^0_sK	KKπ K^0_sK	φπ K^0_sK	φπ K*K	φπ KKπ	φπ φπ	K*K K*K	K*K KKπ	KKπ KKπ	Total
K^0_sK K^0_sK		3								3
K*K K^0_sK	**75**	34								109
KKπ K^0_sK	16	**124**								140
φπ K^0_sK		3	**91**		1					95
φπ K*K				**67**	29				2	98
φπ KKπ				10	**77**	1			1	89
φπ φπ					3	**55**				58
K*K K*K							**55**	52	8	115
K*K KKπ				1			11	**79**	27	118
KKπ KKπ					6		2	31	**77**	116
Total	91	164	91	78	116	56	68	162	115	941

Table 8.10: Counts from hadronic Monte Carlo. Each row represents 1,000 events which were decayed to two three-prong final states, and detected as that column.

To / From	Tag / Recoil		φπ				K*K				KKπ				K^0_sK			
			φ1ν		K K1ν		φ1ν		K K1ν		φ1ν		K K1ν		φ1ν		K K1ν	
Tag	Recoil		μν	e ν	μν	e ν	μν	e ν	μν	e ν	μν	e ν	μν	e ν	μν	e ν	μν	e ν
φπ	φ1ν	μν	**4**	4								1	1					
		e ν	11	**23**	1	1						1						
	φρ		1	1	1													
	K*+K*0				1	2												
	Hadronic		1	1	1	2			0.5	1			0.5					
K*K	φ1ν	μν					**7**	4			2	2						
		e ν					11	**17**		1	8	9	2	1				
	φρ						2	1		1	3	1		1				
	K*+K*0									2			5	1				
	Hadronic								1.5	0.5			0.5	0.5				
KKπ	φ1ν	μν					1	1			**7**	6						
		e ν		1				1			9	**28**	1	1				
	φρ						1				5	1						
	K*+K*0												4	2				
	Hadronic					0.5				0.5			2.5	2				1
K^0_sK	φ1ν	μν													**3**	4	2	
		e ν										1			22	**29**	1	1
	φρ														4	2		
	K*+K*0																3	5
	Hadronic																1.5	2.5

Table 8.11: Counts from semileptonic Monte Carlo. Each row represents 1,000 events which were decayed to two three-prong final states, and detected as that column. Hadronic Monte Carlo tagged as semileptonic is given one-half count per triplet in the appropriate row.

To / Tag		$\phi\pi$	K*K	KKπ	K^0_SK	R
From / Recoil		$\phi l\nu$	$\phi l\nu$	$\phi l\nu$	$\phi l\nu$	$\phi l\nu$
Tag	Recoil	Sum	Sum	Sum	Sum	Sum
$\phi\pi$	$\phi l\nu$ Sum	**42**	0	2	0	0.53
	$\phi\rho$	2	0	0	0	0.88
	K*+K*0	0	0	0	0	0.35
	Hadronic	2	0	0	0	0.5
K*K	$\phi l\nu$ Sum	0	**39**	21	0	0.53
	$\phi\rho$	0	3	4	0	0.88
	K*+K*0	0	0	0	0	0.35
	Hadronic	0	0	0	0	0.5
KKπ	$\phi l\nu$ Sum	1	3	**50**	0	0.53
	$\phi\rho$	0	1	6	0	0.88
	K*+K*0	0	0	0	0	0.35
	Hadronic	0	0	0	0	0.5
K^0_SK	$\phi l\nu$ Sum	0	0	1	**58**	0.53
	$\phi\rho$	0	0	0	6	0.88
	K*+K*0	0	0	0	0	0.35
	Hadronic	0	0	0	0	0.5

Table 8.12: Efficiencies from semileptonic Monte Carlo. Column R indicates the relative branching fraction of the various modes to three-prong decays. The only hadronic contribution is from two $\phi\pi \times \phi\pi$ events.

by the number produced. However, this ignores cross-talk between modes, which is particularly important for the $K^*/K\pi$ and e/μ distinctions. Fortunately, we know the relative production rates for these modes to high accuracy. Therefore, we can calculate the contribution to each mode from the different components.

For the semileptonic events, we start out by combining the events for muons and electrons. This is easy, since they have essentially the same branching ratio. Next, we disregard all the non-resonant $KKl\nu$ events, which contain most of the background. This gives us the matrix in Table 8.12. We see that the contribution from background processes is much smaller than from signal modes, and therefore can be neglected.

However, there is still difficulty with $K^*/K\pi$ discrimination, as in the hadronic

From \ To		K*K K^0_SK	KKπ K^0_SK	$\phi\pi$ K*K	$\phi\pi$ KKπ	K*K K*K	K*K KKπ	KKπ KKπ	K*K ϕlν	KKπ ϕlν	Total	N K*	D
K*K K^0_SK	E	7.5%	3.4%	0.0%	0.0%	0.0%	0.0%	0.0%	0.0%	0.0%	**10.9%**	1	2
	P	0.92	0.41	0.00	0.00	0.00	0.00	0.00	0.00	0.00	**1.33**	1	2
KKπ K^0_SK	E	1.6%	12.4%	0.0%	0.0%	0.0%	0.0%	0.0%	0.0%	0.0%	**14.0%**	0	2
	P	0.08	0.59	0.00	0.00	0.00	0.00	0.00	0.00	0.00	**0.67**	0	2
$\phi\pi$ K*K	E	0.0%	0.0%	6.7%	2.9%	0.0%	0.0%	0.0%	0.0%	0.0%	**9.6%**	1	2
	P	0.00	0.00	0.94	0.49	0.00	0.00	0.00	0.00	0.00	**1.43**	1	2
$\phi\pi$ KKπ	E	0.0%	0.0%	1.0%	7.7%	0.0%	0.0%	0.0%	0.0%	0.0%	**8.7%**	0	2
	P	0.00	0.00	0.06	0.51	0.00	0.00	0.00	0.00	0.00	**0.57**	0	2
K*K K*K	E	0.0%	0.0%	0.0%	0.0%	5.5%	5.2%	0.8%	0.0%	0.0%	**11.5%**	2	1
	P	0.00	0.00	0.00	0.00	0.86	0.44	0.19	0.00	0.00	**1.49**	2	1
K*K KKπ	E	0.0%	0.0%	0.0%	0.0%	1.1%	7.9%	2.7%	0.0%	0.0%	**11.7%**	1	2
	P	0.00	0.00	0.00	0.00	0.14	0.52	0.52	0.00	0.00	**1.17**	1	2
KKπ KKπ	E	0.0%	0.0%	0.0%	0.0%	0.2%	3.1%	7.7%	0.0%	0.0%	**11.0%**	0	1
	P	0.00	0.00	0.00	0.00	0.00	0.04	0.29	0.00	0.00	**0.33**	0	1
K*K ϕlν	E	0.0%	0.0%	0.0%	0.0%	0.0%	0.0%	0.0%	2.0%	1.1%	**3.0%**	1	2
	P	0.00	0.00	0.00	0.00	0.00	0.00	0.00	0.97	0.52	**1.49**	1	2
KKπ ϕlν	E	0.0%	0.0%	0.0%	0.0%	0.0%	0.0%	0.0%	0.2%	2.5%	**2.7%**	0	2
	P	0.00	0.00	0.00	0.00	0.00	0.00	0.00	0.03	0.48	**0.51**	0	2
Total	E	**9.1%**	**15.8%**	**7.7%**	**10.6%**	**6.8%**	**16.2%**	**11.2%**	**2.1%**	**3.6%**	**83.1%**		
	P	**1.00**	**1.00**	**1.00**	**1.00**	**1.00**	**1.00**	**1.00**	**1.00**	**1.00**	**9.00**		

Table 8.13: $\overline{K}^{*0}K^+$versus$K^+K^-\pi^+$ efficiencies. Efficiencies are normalized to 1000 events for hadronic modes and 2000 events for semileptonic.

modes. These modes are summarized in Table 8.13. We resolve this ambiguity not by eliminating it, but quantifying it. We calculating the probability for a measured state to have been produced by a given channel. Since we have low statistics, this will generally result in fractional events per channel. These will be used in a likelihood analysis in the next chapter.

To calculate these probabilities, we make use of Bayes Theorem. The probability that a measured state M_j came from a generated state G_i is:

$$P(G_i|M_j) = \frac{P(M_j|G_i)P(G_i)}{P(M_j)} = \frac{P(M_j|G_i)P(G_i)}{\sum_n P(M_j|G_n)P(G_n)} \tag{8.2}$$

$P(M_j|G_i)$ is just the efficiency for measuring mode i as j. The important factor in $P(G_i)$ is the relative production rates. From Table 5.1, we get the relative probability for generation:

$$\begin{aligned}
\kappa &\equiv \frac{P(D_s^+ \to K^+\overline{K}^{*0} \to K^+(K^-\pi^+))}{P(D_s^+ \to K^+K^-\pi^+)} && (8.3)\\
&= \frac{B(D_s^+ \to \overline{K}^{*0}K^+)B(\overline{K}^{*0} \to K^-\pi^+)}{B(D_s^+ \to K^+K^-\pi^+)} && (8.4)\\
&= \frac{0.95B(D_s^+ \to \phi\pi^+)0.67}{0.25B(D_s^+ \to \phi\pi^+)} && (8.5)\\
&= 2.55 \pm 0.96. && (8.6)\\
& && (8.7)
\end{aligned}$$

Each mode picks up a factor of κ for each $\overline{K}^{*0}K^+$ in the event. There is also a multiplicity of two corresponding to the sum over charge-conjugates, for modes where both triplets do not come from the same decay. The efficiency for a real mode is then the sum of the efficiencies for all the modes in which it appears.

To illustrate, consider event 7108/19638, identified as $\overline{K}^{*0}K^+ \times K^+K^-\pi^+$. Reading down the appropriate column of Table 8.13 gives a normalization of $5.2\%\kappa^2 + (2)(7.9\%\kappa)+3.1\%$. This event is then treated as 44% $\overline{K}^{*0}K^+ \times \overline{K}^{*0}K^+$, 52% $\overline{K}^{*0}K^+ \times K^+K^-\pi^+$, and 4% $K^+K^-\pi^+ \times K^+K^-\pi^+$. Those generated modes have efficiencies of 11.5%, 11.7%, and 11.0%, respectively, for being detected in any mode.

Mode	Number	Background	Efficiency for 6 Prongs	Relative BF to 6 Prongs
$\phi\pi^{\pm} \times \phi\pi^{\pm}$	0.00		5.5%	0.24
$\phi\pi^{\pm} \times K^{*0}K^{\pm}$	0.94 ± 0.03^{a}	0.070	9.6%	2×0.31
$\phi\pi^{\pm} \times K^{\pm}K^{\mp}\pi^{\pm}$	0.06 ± 0.03^{a}	0.005	8.7%	2×0.12
$K^{*0}K^{\pm} \times K^{*0}K^{\pm}$	1.30 ± 0.15^{b}	0.014	11.5%	0.40
$K^{*0}K^{\pm} \times K^{\pm}K^{\mp}\pi^{\pm}$	0.66 ± 0.12^{b}	0.039	11.7%	2×0.16
$K^{\pm}K^{\mp}\pi^{\pm} \times K^{\pm}K^{\mp}\pi^{\pm}$	0.04 ± 0.03^{b}	0.022	11.0%	0.06
$\phi\pi^{\pm} \times K^{0}_{S}K^{\pm}$	0.00		9.1%	2×0.17
$K^{*0}K^{\pm} \times K^{0}_{S}K^{\pm}$	0.8 ± 0.2^{c}	0.114	10.9%	2×0.22
$K^{\pm}K^{\mp}\pi^{\pm} \times K^{0}_{S}K^{\pm}$	1.2 ± 0.2^{c}	0.058	14.0%	2×0.09
$\phi\pi^{\pm} \times \phi l^{\pm}\nu$	0.00		2.1%	2×0.26
$K^{*0}K^{\pm} \times \phi l^{\pm}\nu$	0.00		3.0%	2×0.34
$K^{\pm}K^{\mp}\pi^{\pm} \times \phi l^{\pm}\nu$	0.00		2.7%	2×0.13
$K^{0}_{S}K^{\pm} \times \phi l^{\pm}\nu$	0.00		2.9%	2×0.18

Table 8.14: Effective number of signal and background events. The uncertainty in the number of events comes from uncertainty in the value of $B(D_s \rightarrow K^+K^-\pi^+)$ used in the unfold matrix; superscripts indicate correlated errors. Background is only assigned to modes with a non-zero number of events. The factor of two in the relative branching fraction comes from summing over the charge-conjugate decays.

This procedure could be expanded to cover all modes with cross-talk. However, we do not wish to make use of additional relative branching fractions, since we intend to measure them. The effect of other channels can be considered part of the uncertainty in our efficiencies. That uncertainty goes like $\sqrt{N}$ in the number of observed events, and therefore will be on the order of 10% per channel. These will be factored into our systematic error.

Table 8.9 shows the modes measured from the data. Table 8.14 shows the effective number of generated modes this corresponds to, along with their efficiency and relative branching fractions. We also show the expected contribution from the 0.32 background events.

Chapter 9 Results

Table 8.14 contains all the information we need to measure relative branching fractions. Using $B(D_s^+ \to \phi\pi^+) = 0.035 \pm 0.04$ and $\mathcal{L} = 22.8 \pm 0.6$ pb^{-1}, we can also calculate the cross-section. We accomplish this by means of a likelihood analysis.

For a likelihood analysis, we first calculate a probability density function $p(x;\mu)$, where x is a measurement and μ is derived from the physical quantities of interest. We then define our likelihood as $L(\mu;x) \equiv p(x;\mu)$. We choose the value μ_0 which maximizes $\log L(\mu)$ as our estimator for μ, and define our error bars $\sigma_\pm$ from $\log L(\mu_0 \pm \sigma_\pm) = \log L(\mu_0) - 0.5$.

9.1 Summed Mode Analysis

We start by summing over all the modes in Table 8.14. Our likelihood is then derived from the Poisson distribution for the total number of events detected:

$$L(n;\mu) \equiv P(\mu;n) = \frac{\mu^n e^{-\mu}}{n!}, \tag{9.1}$$

for $n = 5$. The expected number of events is:

$$\mu = xN_{\phi\pi\phi\pi} + \beta \tag{9.2}$$

where $N_{\phi\pi\phi\pi}$ is defined by Equation 5.5, β is the background events, and our total relative efficiency is

$$x = \sum_{ij} b_i b_j \epsilon_{ij} = 0.336, \tag{9.3}$$

where ϵ_{ij} is the efficiency for mode $\{i,j\}$ and b_i is the relative branching fraction, from Equation 5.2.

We then examine the likelihood function, shown in Figure 9.1, to obtain our best

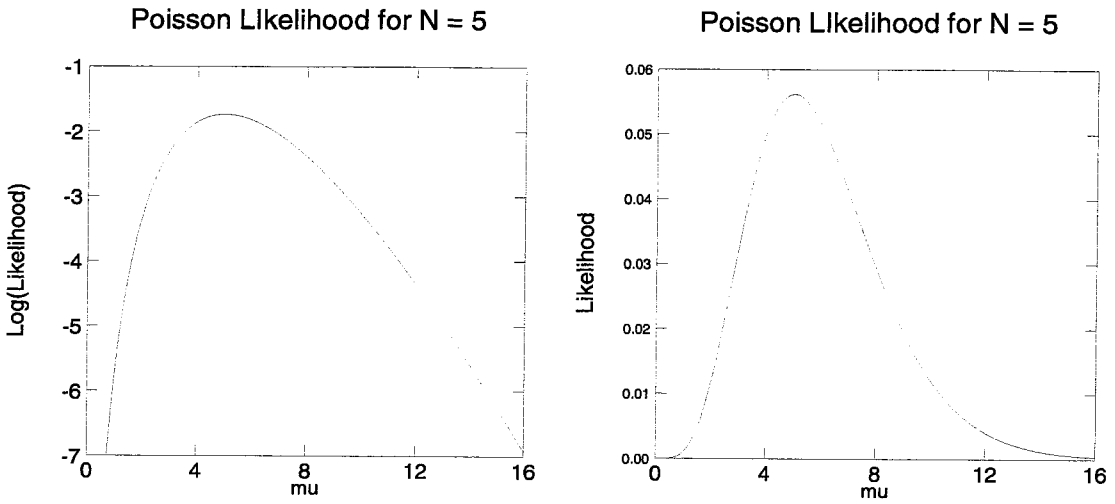

Figure 9.1: Poisson likelihood for n = 5.

estimate for μ, $\mu_0 = 5.0^{+2.6}_{-1.9}$. The statistical errors are sufficiently large we can neglect the background term and invert Equation 9.2 to obtain $N_{\phi\pi\phi\pi} = 14.9^{+7.7}_{-5.7}$. With the $\phi\pi$ branching fraction, that gives $N_{D_s^+D_s^-} = 12.1^{+6.3}_{-4.7} \times 10^3$, for a cross-section of $\sigma(e^+e^- \to D_s^+D_s^-) = 0.53^{+0.28}_{-0.20}$ nb. This is smaller than, but still within 1σ of, the prediction of 0.8 nb from the coupled-channel model. We see that our statistical uncertainty is completely dominated by the errors on the Poisson likelihood for five events.

9.2 Multiple Mode Analysis

There is additional information we can extract from this sample, based on the fact that we not only know the number of observed events, but also their distribution among the various decay modes. We therefore construct a probability distribution, and hence a likelihood, that is a product over the decay channels:

$$L(\vec{\mu};\vec{n}) \equiv P(\vec{n};\vec{\mu}) = \prod_{ij} P(n_{ij};\mu_{ij}), \tag{9.4}$$

where n_{ij} is the number of events in mode $\{i,j\}$, and the expected number of events in each mode is

$$\mu_{ij} = N_{\phi\pi\phi\pi}\ b_i b_j \epsilon_{ij} + \beta_{ij}. \tag{9.5}$$

These are the same as the components of Equation 9.3, with β_{ij} being the background in each channel. $P(n;\mu)$ is still the Poisson distribution for n events; however we generalize $n!$ to $\Gamma(n+1)$, allowing for fractional event counts.

Using the relative branching fractions, we can fit directly to $N_{\phi\pi\phi\pi}$, as above. Alternatively, we can fix $N_{\phi\pi\phi\pi}$ to one of our measured modes, and then fit for the relative branching fraction. We use the MINUIT[26] fitting package to obtain the value and uncertainty of our fit.

9.2.1 Cross-Section

We start by using this method to reproduce the calculation above. Again, we neglect background. Using all the information in Table 8.14 gives us the likelihood shown in Figure 9.2. As expected, it is identical to Figure 9.1. The fit returns $N_{\phi\pi\phi\pi} = 14.9^{+7.7}_{-5.7}$, the same as before.

9.2.2 $\overline{K}^{*0}K^+$ Branching Fraction

The main advantage of the multiple mode analysis is that it allows us to compare between modes. We will use the same events to measure the relative branching fraction $k = B(D_s^+ \to \overline{K}^{*0}K^+)/B(D_s^+ \to \phi\pi^+)$. We define $B(\phi\pi^+) \equiv B(D_s^+ \to \phi\pi^+)$, and similarly for $B(\overline{K}^{*0}K^+)$. We then derive

$$N_{\phi\pi\phi\pi} = NB(\phi\pi^+)B(\phi\pi^-) = NB(\overline{K}^{*0}K^+)B(\phi\pi^-)\frac{B(\phi\pi^+)}{B(\overline{K}^{*0}K^+)} = \frac{N_{\overline{K}^{*0}K^+\phi\pi^-}}{k}. \tag{9.6}$$

The number of $\overline{K}^{*0}K^+ \times \phi\pi^-$ events is

$$N_{\overline{K}^{*0}K^+\phi\pi^-} = NB(\overline{K}^{*0}K^+)B(\phi\pi^-) = \frac{N_{\phi\pi K^{*0}K}}{2} = \frac{n_{K^{*0}K\phi\pi}}{2\epsilon_{K^{*0}K\phi\pi}}, \tag{9.7}$$

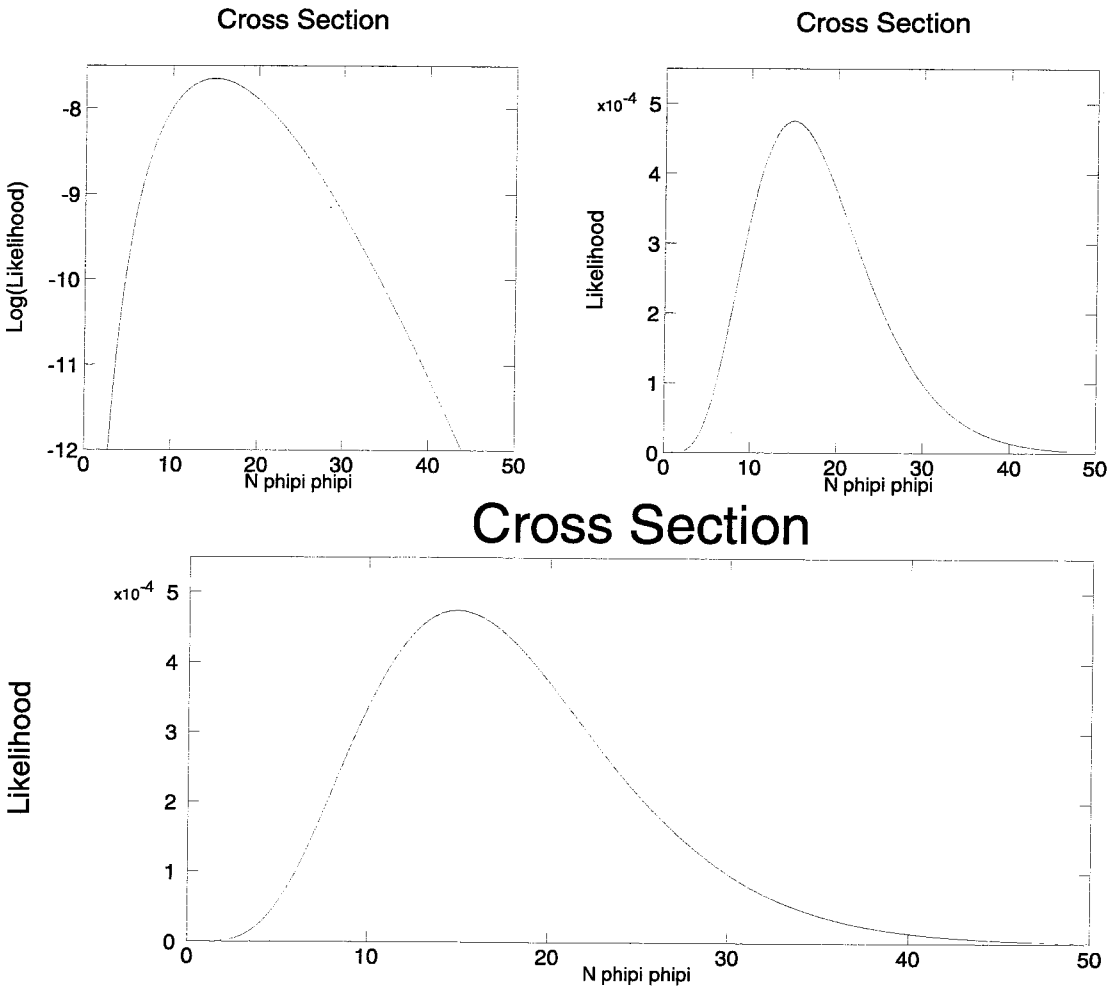

Figure 9.2: Multiple mode likelihood function for $N_{\phi\pi\phi\pi}$. The Poisson likelihood for five events is shown as a dotted line on the lower plot.

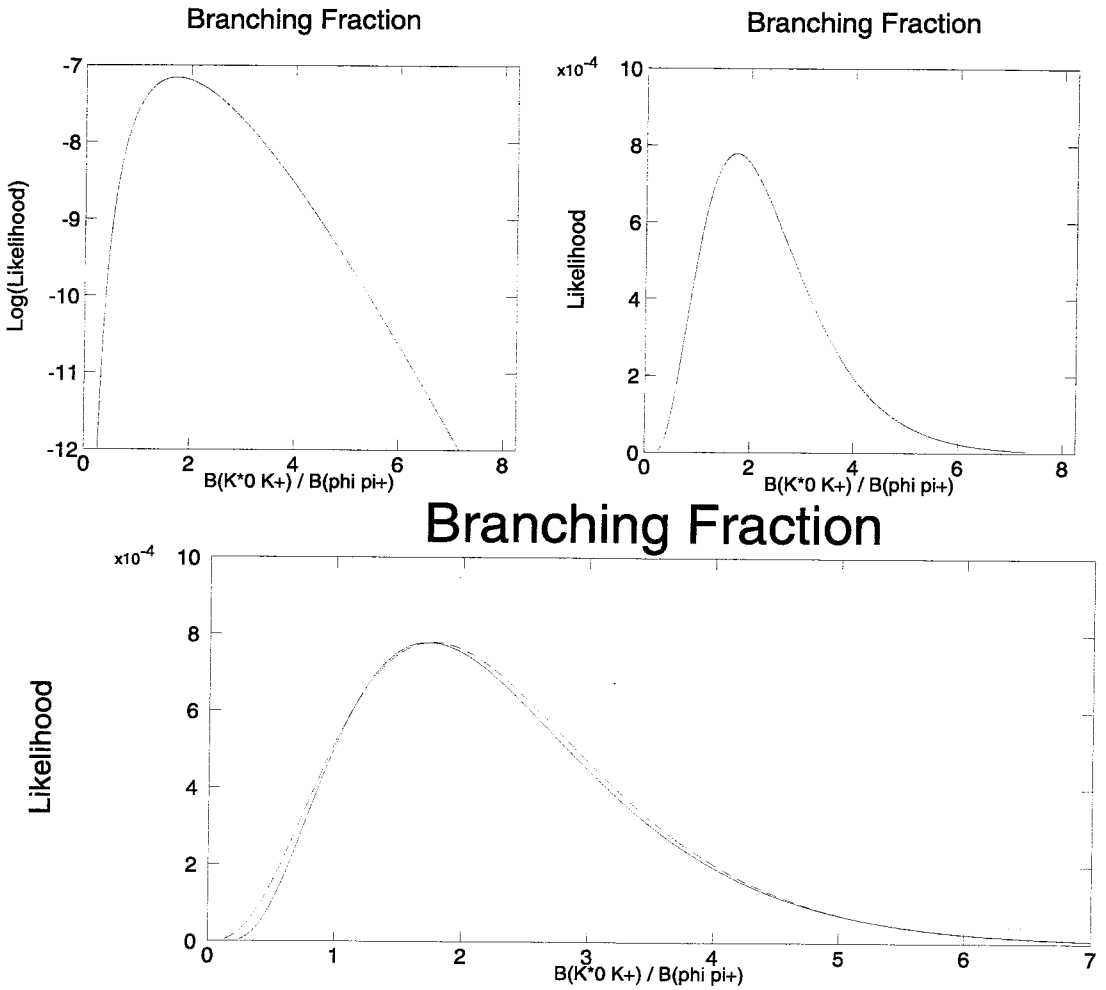

Figure 9.3: Likelihood function for $\frac{B(D_s^+ \to \overline{K}^{*0} K^+)}{B(D_s^+ \to \phi\pi^+)}$. The Poisson likelihood for three events is shown as a dotted line on the lower plot.

where $n_{\phi\pi \times \overline{K}^{*0} K+}$ and $\epsilon_{\phi\pi\ \overline{K}^{*0} K+}$ are the number of observed events and the efficiency for that mode plus its charge conjugate, hence the factor of two.

The main difference between the branching fraction and cross-section fits is that the former is non-linear in the fitted parameter, since we get one factor of k for each K^* in the final state. Since we have calculated our efficiencies as a convolution of the $\overline{K}^{*0} K^+$ and $K^+ K^- \pi^+$ modes, we keep the ratio κ fixed. The fractions for those two channels are then fit relative to all the other channels, which remain fixed.

This gives us the likelihood function shown in Figure 9.3, with $k = 1.72^{+1.20}_{-0.83}$. The fit resembles the Poisson likelihood for three events, except for being strongly suppressed near zero. This is almost one sigma larger than the PDG value of $0.95 \pm$

Source	Amount	$\Delta N_{\phi\pi\phi\pi}$ [14.9]	$\Delta\sigma(e^+e^- \to D_s^+D_s^-)$ [0.53 nb]	$\Delta\frac{B(D_s^+\to\overline{K}^{*0}K^+)}{B(D_s^+\to\phi\pi^+)}$ [1.72]
Background	0.32 events	-1.4	-0.05	-0.1
Branching Fractions	$\pm\sigma_b/\sqrt{4}$	+2.1 -1.7	+0.07 -0.06	+0.25 -0.19
Efficiencies	$\pm\sigma_\epsilon/\sqrt{13}$	+0.5 -0.5	+0.02 -0.02	+0.02 -0.02
Total Systematic		+1.9 -2.5	+0.07 -0.09	+0.22 -0.24
Statistical	$\log L - 0.5$	+7.7 -5.7	+0.28 -0.20	1.20 -0.76

Table 9.1: Sources of uncertainty in fitted and derived quantities.

0.05.

More significantly, our result is also larger than the BSW prediction of $k = 0.56 \pm 0.07$, differing by 1.16 ± 0.8, or 1.4σ. While not as compelling as the CLEO measurements, this does provide a largely independent confirmation of the weakness of the BSW model in describing the $D_s^+ \to \overline{K}^{*0}K^+$ decays.

9.3 Systematics

There are three main sources of systematic error. The first is from our background. Due to the large uncertainty, we do not include it directly in our fit. Rather, we fit both with and without background, and treat the difference as a systematic error. This should give us a conservative estimate.

The other two sources of systematic error are from the measurement uncertainty for the relative branching fractions, and the $\sqrt{N}$ uncertainty for the efficiencies. We vary each of these up and down in unison to obtain a conservative error estimate. Since there are four different branching fractions, shown in Table 5.2, we vary all of them by $\pm\sigma_b/\sqrt{4}$. The thirteen different efficiencies in Table 8.14 give a variation of $\pm\sigma_\epsilon/\sqrt{13}$.

Table 9.1 summarizes the various sources of uncertainty. The total systematic error is the sum in quadrature of the three. Other sources of error, such as uncertainty in κ, and bias in the Monte Carlo, would be smaller than this.

9.4 Conclusions

Combining all this information gives the following values for the cross-section and relative branching fraction:

$$\sigma(e^+e^- \to D_s^+ D_s^-) \text{ at } 4.03 \text{ GeV} \;=\; 0.53\,^{+0.28\,+0.07}_{-0.20\,-0.09}\,\text{nb}$$

$$\frac{B(D_s^+ \to \overline{K}^{*0} K^+)}{B(D_s^+ \to \phi\pi^+)} \;=\; 1.78\,^{+1.23\;+.22}_{-0.80\,-0.24}$$

We have seen that the use of kinematic fitting and confidence levels to prepare a doubly-tagged sample, combined with a likelihood analysis to interpret it, forms a very powerful tool for working with small datasets. The joint confidence level is a useful discriminator against background, while pulling in events that would not have passed cuts on kinematic fitting or particle identification alone. This, combined with an unfold matrix, allows us to use non-resonant $K^+K^-\pi^+$ events as part of our tag sample, to good effect.

The results are in reasonable agreement with predictions, given the low statistics. Our measurement provides confirmation for the coupled-channel model, and corroboration of inconsistencies between experimental measurements and BSW. Higher precision results for threshold-pair production of D_s mesons will have to await future experiments with higher statistics.

Part V

The Appendix

Appendix A One Event Displays

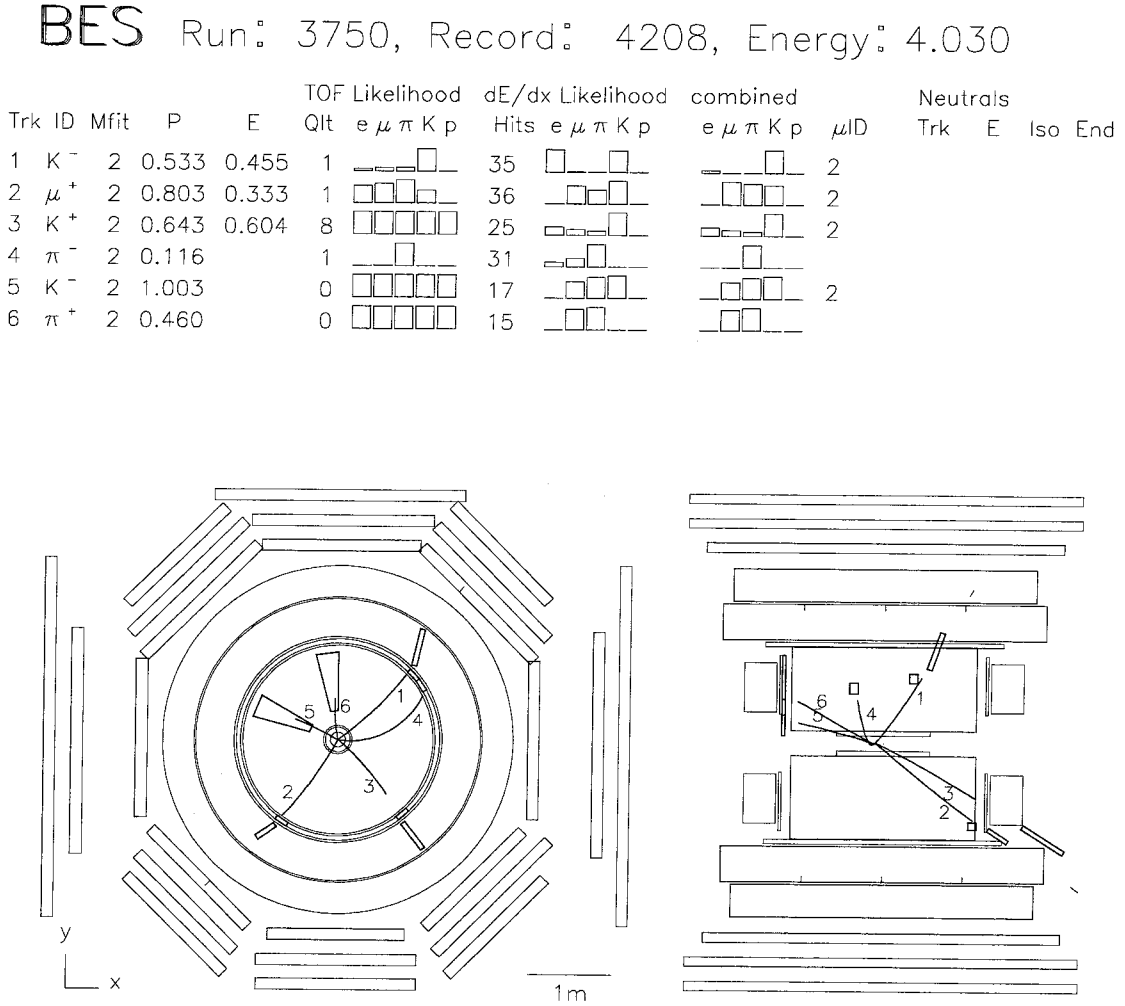

Figure A.1: One-event display for Run 3750, Event 4208.

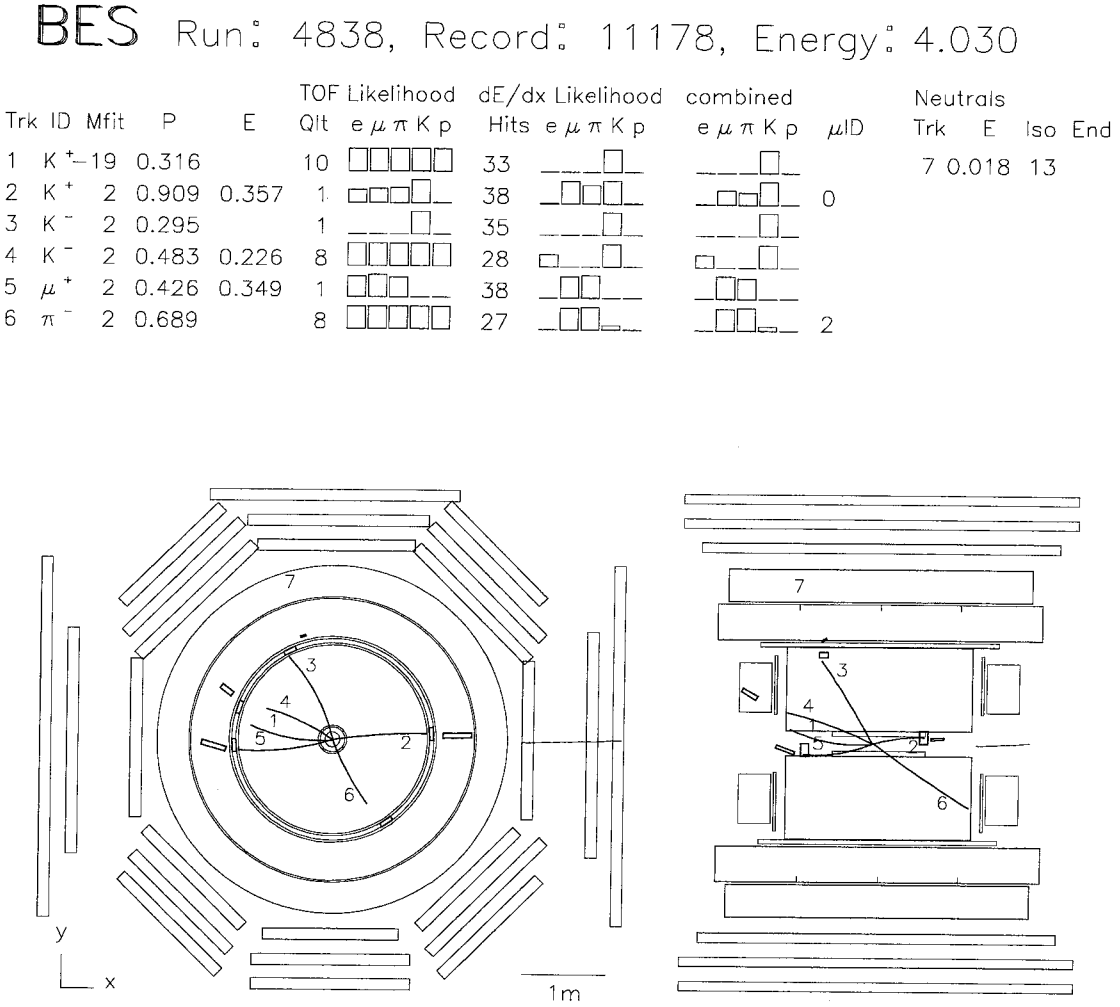

Figure A.2: One-event display for Run 4838, Event 11178.

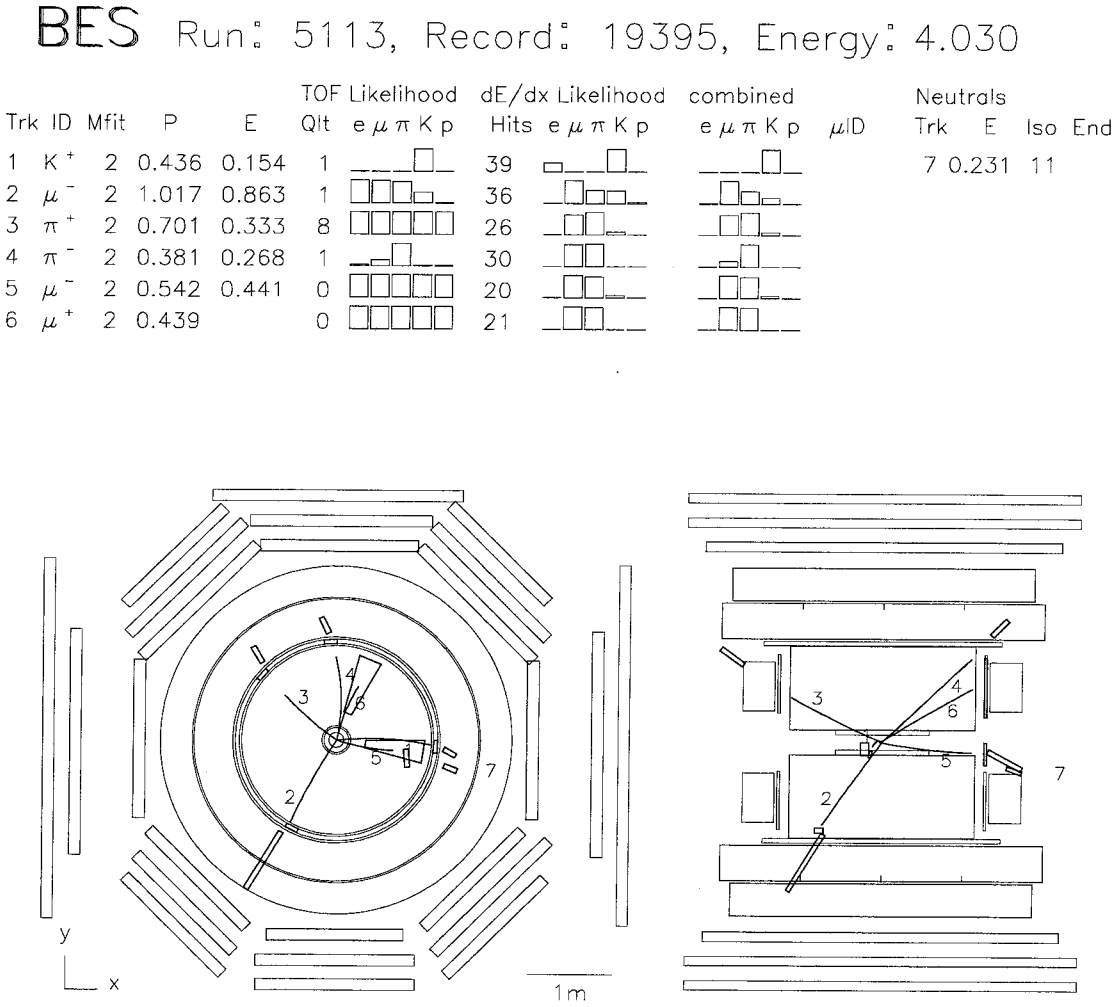

Figure A.3: One-event display for Run 5113, Event 19395.

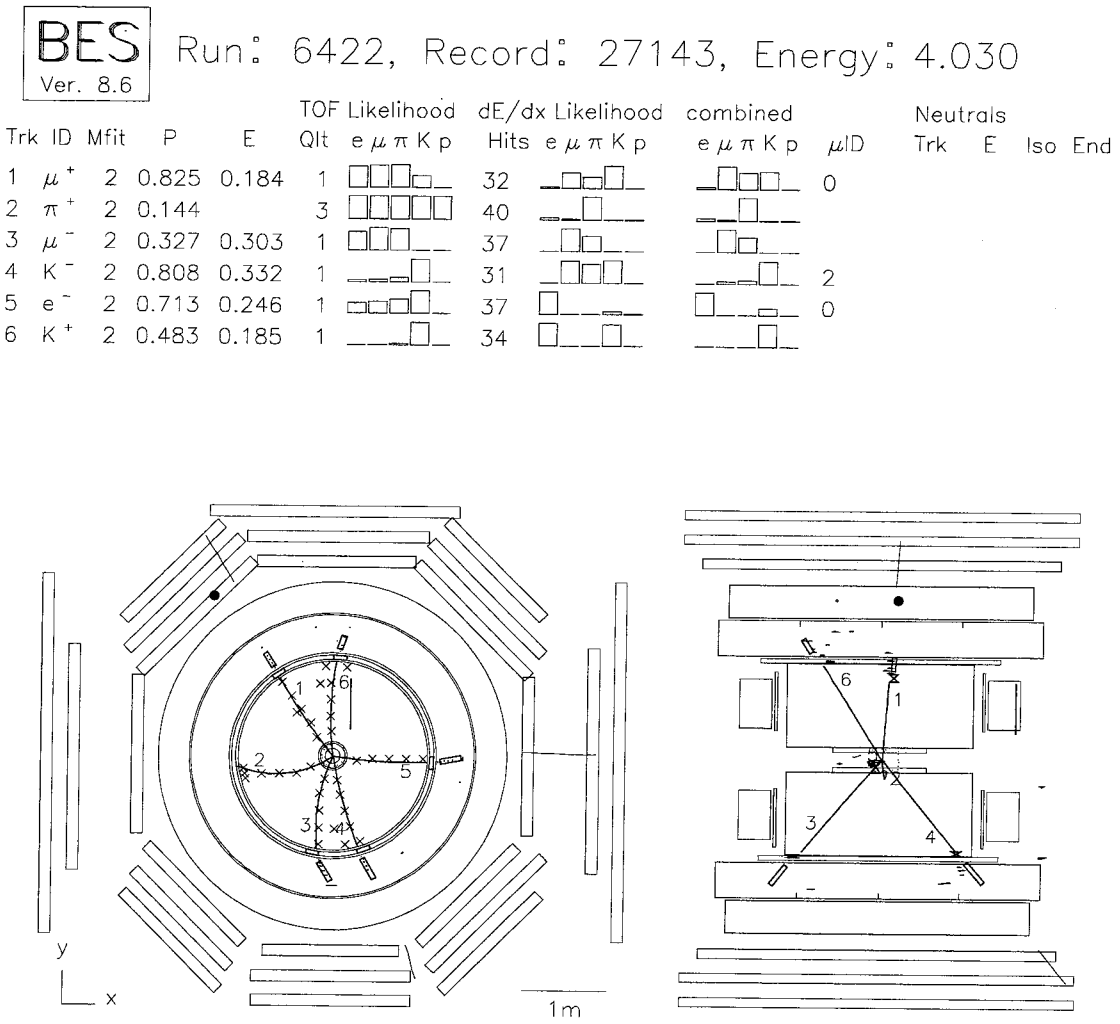

Figure A.4: One-event display for Run 6422, Event 27143.

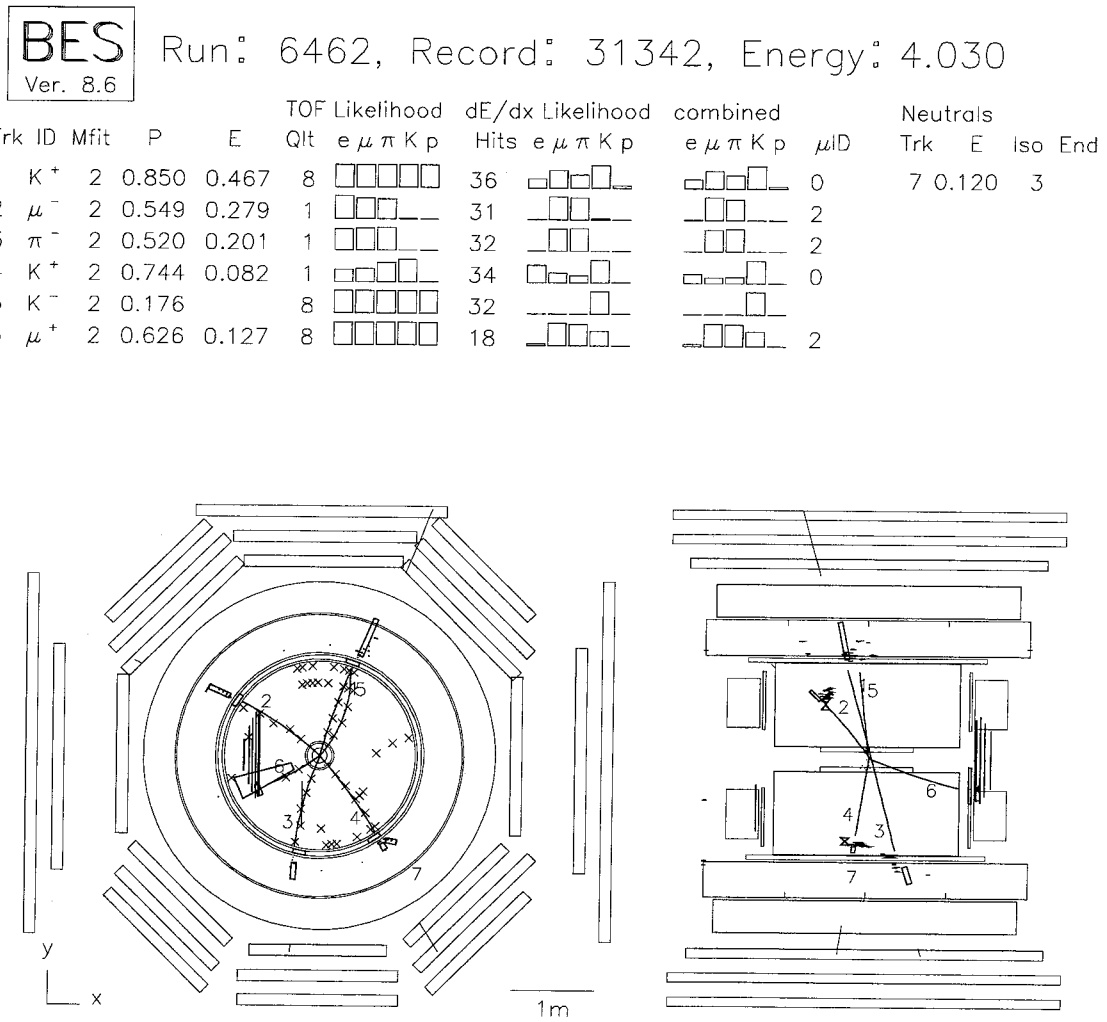

Figure A.5: One-event display for Run 6462, Event 31342.

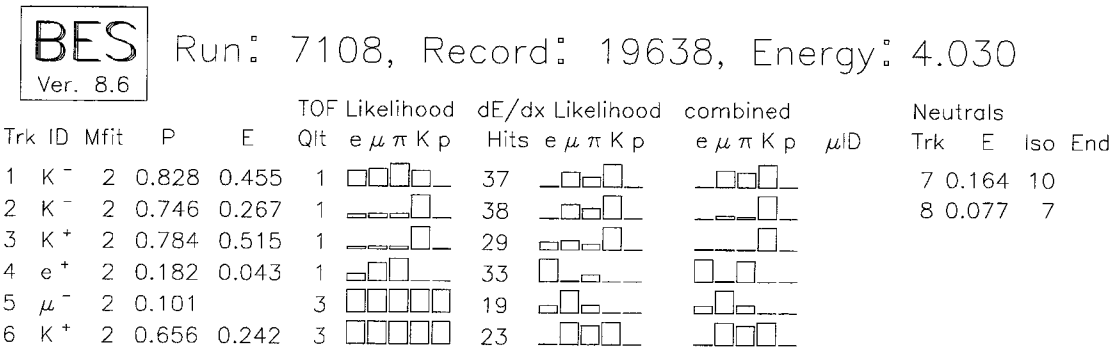

Figure A.6: One-event display for Run 7108, Event 19638.

Bibliography

[1] Particle Data Group (L. Montanet *et al.*), Phys. Rev. D **50**, 1173 (1994).

[2] C. W. Bernard, A. X. El-Khadra, A. Soni, Phys. Rev. D **45**, 869-874 (1992).

[3] M. H. Ye and Z. P. Zheng, in *Proceedings of the 1989 International Symposium on Lepton and Photon Interactions at High Energies,* Stanford U., Stanford, California, 122 (1989).

[4] L. Jones, *A Measurement of the Mass of the Tau Lepton*, Ph.D. Thesis, California Institute of Technology (1995). Preprint CALT-68-1920.

[5] *Beijing e^+e^- Collider and BES Research Report,* (tr. J. Chen) Institute of High Energy Physics, Beijing, P.R.C.

[6] H. F. Guo *et al.*, Nucl. Instrum. Meth. A **336**, 542-551 (1993).

[7] C. C. Zhang, private communication (1995).

[8] J. Lu, X. F. Zhou, C. C. Zhang, L. Ye, *Large angle BB events and luminosities for D_s runs (1992-1994)* BES internal documentation, 5 May, 1994.

[9] W. S. Lockman, *D and D_s Production in the Range* $3.8 < \sqrt{s} < 4.5 GeV$, Mark III Memorandum, March 20, 1987.

[10] CLEO Collaboration (M. Daoudi *et al.*), Phys. Rev. D **45**, 3965-3975 (1992).

[11] Mark III Collaboration (J. Adler *et al.*), Phys. Rev. Lett. **64**, 169-171 (1990).

[12] S. R. Wasserbaech, *Hadronic Decays of the D_s Meson,* Ph.D. Thesis, Stanford University, 1989. Preprint SLAC-345.

[13] B. Lowery, Presented at the 1994 Meeting of the American Physical Society, Division of Particles and Fields, Albuquerque, NM, August 2-6, 1994.

[14] CLEO Collaboration (J. Alexander *et al.*), Phys. Rev. Lett. **65**, 1531-1534 (1990).

[15] C. Matthews, *Inclusive Weak Decays of Charmed Mesons*, Ph.D. Thesis, California Institute of Technology (1995). Preprint CALT-68-1855.

[16] D. G. Hitlin, Banff 1988, in *Proceedings, Particles and Fields,* **3**, 607-712 (1988).

[17] M. Bauer, B. Stech, M. Wirbel, Z. Phys. C **34**, 103-115 (1987).

[18] M. Bauer, B. Stech, M. Wirbel, Z. Phys. C **29**, 637-642 (1985).

[19] M. Bauer, Ph.D. thesis, Ruprecht-Karls-Universität (1987).

[20] M. Bauer, M. Wirbel, Z. Phys. C **42**, 671-678 (1989).

[21] N. Isgur, D. Scora, B. Grinstein, M. B. Wise, Phys. Rev. D **39**, 799-816 (1989).

[22] M. Sadzikowski, *Semileptonic decays of heavy to light mesons from an MIT bag model* Jagellonian U. (1994). Preprint TPJU-13-94.

[23] M. Kelsey, BES Note 94-005, April 6, 1994.

[24] The BES Collaboration (adapted from Mark III), 1993.

[25] R. H. Dalitz, *Phil. Mag.* **44**, 1068 (1953), cited in D. H. Perkins, *Introduction to High Energy Physics*, Addison-Wesley Publishing Co. 119-124 (1987).

[26] CERN, 1992.